UNIVERSITY OF OKLAHOMA

GRADUATE COLLEGE

INVESTIGATING AEROSOL OPTICAL PROPERTIES FROM LONG-RANGE TRANSPORT SMOKE TO THE SOUTHERN GREAT PLAINS U.S.

A THESIS

SUBMITTED TO THE GRADUATE FACULTY

in partial fulfillment of the requirements for the

Degree of

MASTER OF SCIENCE

By

HAYDEN WEBB

Norman, Oklahoma

2025

INVESTIGATING AEROSOL OPTICAL PROPERTIES FROM LONG-RANGE TRANSPORT SMOKE TO THE SOUTHERN GREAT PLAINS U.S.

A THESIS APPROVED FOR THE

SCHOOL OF METEOROLOGY

BY THE COMMITTEE CONSISTING OF

Dr. Marcela Loría-Salazar, Chair

Dr. Jens Redemann

Dr. Connor Flynn

Acknowledgements

First, I would like to thank my advisor, Dr. Marcela Loría-Salazar, for giving me this opportunity and taking a risk on me as a non-meteorological background student. I would not have been able to reach this point in my career without your guidance.

I would also like to thank Dr. Connor Flynn and Kyle Eskew for assisting with this work's lidar and HYSPLIT portions. Dr. Flynn has been a fantastic help with career advice as well as an amazing resource for data. Kyle completed the back trajectory analysis portion of this work as part of his undergraduate research.

Finally, I would like to thank my two best friends in the world for being with me throughout this program. While one is a dog and the other is my partner, I could not have completed this work without their support.

Table of Contents

List of Tables

List of Figures

Abstract

With an increasing number and intensity of wildfires each year, exposure to smoke is a growing health concern. These fires produce large loadings of aerosols, which have intense local effects and also travel thousands of miles downwind. While many field campaigns have been developed to study smoke's physical and chemical properties near the smoke plumes within the U.S., the effects on aerosol physical properties due to long-range transport aging have been less examined. This is especially important as travel times' effects on aerosol properties are not represented in many atmospheric models. This investigation aims to improve the understanding of aerosol physical properties such as aerosol optical depth (AOD), extinction Ångström exponent (EAE), single scattering albedo (SSA), and absorption Ångström exponent (AAE) in the Southern Great Plains (SGP), specifically Oklahoma. A total of twenty-seven cloud-free smoke events between 2015 and 2022 were identified using a combination of MODIS Deep Blue (DB) AOD maps, AERONET ground station data, and HYSPLIT back-trajectories parameterized by MicroPulse Lidar (MPL) determined plume height. Results indicate that an elevated AOD (~0.2 to ~0.3) path between the western U.S. and the SGP with peaks of AOD > 0.4 in August and September. Comparisons of AERONET observations across various sites revealed evidence of long-range transport, with AOD, EAE, and SSA decreasing and AAE increasing as the smoke traveled to Billings, OK. Mean AOD decreased by ~0.21, ~0.38, ~1.69, ~1.42, and ~0.1, while mean EAE decreased by ~0.13, ~0.2, ~0.25, ~0.18, and ~0.2 for zero through four-day travel time, respectively. Mean SSA decreased by ~0.02, ~0.02, <0.01, ~0.02, and ~0.01, while mean AAE increased by ~1.26, ~0.16, ~0.04, ~0.34, and ~0.32, respective to travel time. While lower arrival height may be associated with shorter travel times, the underlying meteorology (troughs and ridges) driving wind direction and intensity seem to be the primary determinant of the plume

path. The study's findings highlight the need for further research to explore the impact of meteorological conditions and variations in fuel type on smoke aerosol optical properties, with an emphasis on using remote sensing methods for broader analysis.

1. Introduction

1.a. Motivation

Aerosols are solid or liquid particles suspended in the atmosphere (e.g., sea salt, dust, and smoke). Aerosols are a key contributor to the atmospheric radiation budget. However, even today, aerosols are climate models' largest source of uncertainty (Lee et al. 2023). The uncertainties are linked with aerosols' nature and their interaction with their underlying surface as aerosols have the potential to both cool through scattering and warm by absorbing light in the atmosphere, altering the surface energy budget (Chylek and Wong 1995). These fluctuations in the Earth's radiative forcing prevent us from understanding aerosols' extent and role in climate change (Szopa et al. 2023).

There are many sources of aerosols, both natural and anthropogenic. For instance, wind can pick up sea salt from the ocean, volcanos can inject ash into the atmosphere, and factories can generate a wide range of emissions [sulfates, black carbon (BC), etc.]. Aerosols emitted into the atmosphere from their direct source are considered primary aerosols. Secondary aerosols form in the atmosphere through chemical and photochemical reactions with already emitted aerosols or gases (Turpin et al. 1991). An example of primary aerosols is smoke (BC and other gases) produced by wildfires. As these aerosols age through photochemical reactions, their optical properties can change, transforming into brown carbon (BrC). This process is known as secondary aerosol formation. In the context of aerosols, extensive properties like aerosol optical depth (AOD), extinction, scattering, and absorption coefficients depend on the quantity of aerosol particles present. In contrast, intensive aerosol properties are independent of aerosol amount and depend on the nature of the aerosol itself, including single-scattering albedo (SSA), hemispheric backscatter fraction, and Ångström exponent, reflecting size, shape, and composition.

Aerosols also impose a considerable risk to human health. As an example, smoke exposure is a growing public health concern affecting tens of millions of residents of the United States (U.S.) (Cascio 2017). Prolonged exposure (one year or greater) to low concentrations (mean concentration of 8.7 $\mu g/m^3$) of $PM_{2.5}$ (particles with an aerodynamic diameter smaller than 2.5 µm), such as smoke, can increase cardiovascular risk (Gan et al. 2017; Crouse et al. 2012). Research has also shown a correlation between wildfire smoke exposure and an increased risk of cancer of many types, with wildfire smoke exposure accounting for nearly one-third of the national average total cancer risk from hazardous air pollutants (Grant and Runkle 2022).

Wildfires are a natural phenomenon that plays an essential role in the ecological cycle of the western U.S. (Cascio 2017). Furthermore, prescribed fires are performed in this region to mitigate wildfire hazards (Fernandes and Botelho 2003). Even still, in the past decades, the number of large wildfires (>405 hectares) has been on the rise (Dennison et al. 2014; Westerling et al. 2006). This increase is partly due to multiple severe droughts across the western U.S. from 2006 to 2015 (Crockett and Westerling 2018; Kogan and Guo 2015). Woodhouse et al. 2010, suggest that the medieval period (~AD 900–1300) prolonged droughts could serve as a conservative estimate of what to expect in the early 21st century for Southwest North America. Ensemble models of projected wildfire area burned, emissions, and fire season length show that this trend will continue as more land burns each year (Ford et al. 2018; Spracklen et al. 2009). The median model results show an increase in land burned by 24-169% in the western U.S., regardless of the projection method (Yue et al. 2013). The resulting smoke can then be injected upwind (via convection) or downwind (via entrainment) into the free troposphere and travel long distances to other parts of the country or world (Wilkins et al. 2020).

With a projected increase in annual large wildfires (> 405 ha) of seven fires per year and an increase of 355 km^2 area burned per year, wildfires primarily contribute to $PM_{2.5}$ (Dennison et al. 2014). With policymaking primarily aimed at reducing anthropogenic sources of $PM_{2.5}$, wildfire smoke aerosols are also an increasing percentage of total $PM_{2.5}$ emissions (Chowdhury et al. 2024). In the western U.S., wildfires produce more than 50% of summer $PM_{2.5}$ emissions (O'Dell et al. 2019). Wildfires generate strong convective updrafts, which enable smoke aerosols to be injected above the atmospheric boundary layer (ABL) (Colarco et al. 2004). Thermal turbulent mixing then entrains aerosols back into the ABL downwind of the source fire (Colarco et al. 2004). During this transport process, smoke's physical and chemical properties vary significantly based on age, the interaction of sunlight, and the aerosol transported (Hung et al. 2020). Aerosol properties can be further altered as they are enriched by secondary species such as sulfate, ammonium, and nitrite from anthropogenic sources (Reid et al. 2005). Thus, accessing and characterizing smoke aerosols' physical properties can be difficult as they deposit far from their origin.

1.b. Aerosol Optical Properties

To better understand the physical properties of smoke, we use specific measurements to quantify aerosols' physical and optical characteristics. Aerosol optical Depth (AOD) measures the amount of light at a particular wavelength that is attenuated by aerosols within a column of air in the atmosphere (Petty 2006). AOD is an extensive property that indicates the amount of radiation directly prevented from reaching the ground due to aerosol optical loading in the atmosphere (Li et al. 2022). It is mathematically defined as:

$$AOD(s_1, s_2) = \int_{s_1}^{s_2} \beta_{ext}(s) ds \quad \text{(Eq. 1)}$$

Where s1 and s2 typically represent the surface to the top of the atmosphere (TOA), respectively. β_{ext} is known as the extinction coefficient, which gives a measure of how much light is depleted as it travels a measured distance. β_{ext} is simply defined as:

$$\beta_{ext} = \beta_{abs} + \beta_{sca} \quad \text{(Eq. 2)}$$

Here, β_{ext} is the sum of the absorption coefficient β_{abs} and the scattering coefficient β_{sca}, or parameters that measure the relative contributions of absorption and scattering of light to the total extinction of light by a substance (Petty 2006).

The absorption and scattering coefficients are useful for determining other metrics related to aerosol properties, such as the aerosol SSA. SSA is the ratio comparison of the amount of light that is scattered by an aerosol particle, represented by β_{sca}, compared to total light extinction, or β_{ext} (Russell et al. 2002). SSA is an intensive property that ranges from 0 to 1, indicating particle brightness. A value of 1 means that 100% of the incident light is scattered, while a value of 0 means that 100% of the light is absorbed by the particle. SSA is frequently utilized to determine the signs of aerosol radiative effects in the atmosphere (Bergstrom et al. 2007). While SSA for smoke will vary based on fuel type, Ponderosa and other pine trees, such as those along the western U.S., result in values between ~0.8 and ~0.9 for 405 nm (Lewis et al. 2008). Mathematically, it is defined as:

$$\omega = \frac{\beta_{sca}}{\beta_{ext}} = \frac{\beta_{sca}}{\beta_{sca}+\beta_{abs}} \quad \text{(Eq. 3)}$$

The Extinction Ångström exponent (EAE) is a variable that describes how AOD depends on the wavelength of the light (Li et al. 2022; Ångström 1929). It is used to qualitatively indicate the aerosol particle size distribution, where small values (<1) indicate coarse particles such as sea salt and large values (>1.7) indicate fine particles typically from combustion sources (Schuster et al. 2006). While the value of smoke EAE is observed across a range (~0.85 – ~4), Bian et al. (2020) observed ambient smoke in the Pacific West and Southwest regions of the U.S. at ~2.24 and ~2.19, respectively. EAE is defined as (Eck et al. 1999):

$$EAE = \frac{ln\left(\frac{\tau_{\lambda_1}}{\tau_{\lambda_2}}\right)}{ln\left(\frac{\lambda_2}{\lambda_1}\right)} \quad \text{(Eq. 4)}$$

Here, τ_λ is the AOD at wavelength λ.

Related to EAE is the Absorption Ångström Exponent (AAE), which is a component of the Ångström exponent that considers only absorption. AAE describes the spectral dependence of light absorption by aerosols (Helin et al. 2021). AAE is typically used to differentiate between various types of aerosols, such as BC and BrC. While BC is widely accepted at an AAE of 1.0, fresh BC is approximately 1.05 and can vary between 0.8 and 1.4 with coatings of other materials (Liu et al. 2018). Lack and Cappa (2010) showed that while AAE <1.6 does not preclude BrC, BrC cannot be confidently assigned unless AAE >1.6. AAE is defined as:

$$AAE = \frac{ln\left(\frac{\tau_{abs\lambda_1}}{\tau_{abs\lambda_2}}\right)}{ln\left(\frac{\lambda_2}{\lambda_1}\right)} \quad \text{(Eq. 4)}$$

Here, τ_{abs} is the absorption aerosol optical depth (AAOD), which is the absorption component of AOD. AAOD can be derived as a function of SSA and AOD:

$$AAOD = (1 - \omega) \times AOD \quad \text{(Eq. 5)}$$

In aerosol-related health studies, aerosols are referred to as particulate matter (PM) and are categorized based on their aerodynamic diameter. For example, PM_{10} denotes particulate matter with an aerodynamic diameter of less than 10 microns. Thus, smoke aerosols with an aerodynamic diameter of less than 2.5 microns are classified as $PM_{2.5}$.

1.c. Background Research

Understanding the transport of wildfire smoke is crucial, as it can alter the physical properties of smoke aerosols and impact their radiative forcing. Smoke from both local and long-range fires has varying impacts on respiratory and cardiovascular health in affected communities. This variation can partly be attributed to fewer warnings associated with long-range smoke and misclassification. Additionally, chemical changes during transport may play an important role in differentiating local and long-range smoke (Magzamen et al. 2021). Smoke aerosols can be transported long distances and act as pollutants in distant environments. During this transport process, smoke interacts with other atmospheric trace gases, reacting and evolving over time (Sokolik et al. 2019). Understanding smoke transport and its effects on aerosol properties can help improve air quality forecasting and exposure models, comprehend the health effects of acute or chronic smoke exposure, and accurately parameterize climate models (Sokolik et al. 2019). Many attempts have been made to examine the effects of long-range transport on wildfire aerosol properties. However, most studies have been limited in scope to single fire events. Studies range from temporal scales of days such as Sicard et al. (2019) or on the order of weeks (Sillanpää et al. 2005) to months (Wu et al. 2018).

While the studies mentioned above examined smoke undergoing long-range transport, they did not attempt to quantify the changes in aerosol physical properties. Sicard et al. (2019) examined 2017's record-breaking burning season in Canada and the U.S. During the first week of

September, fires were observed across British Columbia, Alberta, Washington, Oregon, Idaho, Montana, and northern California. Satellite imagery was used to track two large smoke plumes that were observed to reach the Iberian Peninsula after days of travel on the 7th and 8th of September. AERONET sites in northern and southern Spain observed 440 nm AOD up to 0.62, AE of 1.6–1.7, fine mode fraction > 0.88, 440 nm AAOD < 0.008, and SSA at 440 nm > 0.98. However, the younger and faster-moving plume comprised over 90% of the column density. Their research used a combination of Lidar networks, including the Cloud-Aerosol Lidar with Orthogonal Polarization (CALIOP), the European Aerosol Research Lidar Network (Aerosol, Clouds, and Trace gases Research Infrastructure) (EARLINET/ACTRIS), and MPLNET, along with HYSPLIT, to determine the altitudes of the plumes during transport. HYSPLIT and MPLNET showed that plume 1 arrived at 3 km over Madrid, and plume 2 arrived at 6 and 11 km. They found that particle depolarization properties increased by 0.05 during the vertical transport from the mid to the upper troposphere.

Between August 23, 2002, and September 23, 2002, Sillanpää et al. 2005 observed episodes of long-range transport particulate in an urban background site in Helsinki, Finland. This work primarily focused on identifying long-range transport episodes and analyzing their chemical composition. A combination of aerosol sampling via two β-attenuation monitors, a virtual impactor, and a Berner low-pressure impactor was used to identify cases associated with high concentrations of $PM_{2.5}$. While two cases were identified during this study, only one was associated with biomass burning. This case was associated with increased biomass signatures, crustal elements (Fe, Al, CA, and Si), and organic material. While HYSPLIT trajectories at fixed heights of 10, 500, and 1000 meters were used, this research focused on examining the path and composition of the parcels rather than examining travel time.

Finally, Wu et al. (2018) examined smoke plumes from the Fort McMurray wildfires in Alberta, Canada, in May 2016. Elevated levels of $PM_{2.5}$ in New York City (NYC) between May 9th–13th and May 25th–29th were observed using a 3-wavelength Elastic-Raman lidar, a ceilometer, CALIOP aboard the CALIPSO satellite, and an AERONET Cimel sun/sky radiometer. These instruments and HYSPLIT back trajectories linked the resulting change in NYC's air quality to the Fort McMurray fires. The May 9 - 13 plume showed deep mixing-layer height (MLH) at ~2.5 km on the 9^{th}, with MLH generally lower than 1.5 km on May 11- 12. Conversely, the May 25 - 29 plume showed two aloft aerosol layers, one below 1 km and the other at 2 – 3 km. Plumes reaching NYC were observed to have decreased SSA and AAE near 1, indicating a strong absorbing component. These plumes were also noted to have undergone vertical mixing and affected surface air quality, with a coincident increase of ground PM2.5 from 5 to 25-30 μg/m^3.

The properties of fresh or recently emitted wildfire aerosols often differ from those of aged aerosols, influencing the overall atmospheric radiative budget in complex ways. Wildfires produce large quantities of BC into the atmosphere. As these particles travel and age, they build up coatings that can initially increase the SSA and later decrease it as the coatings wear down (Sedlacek et al., 2022). For instance, the aging of laboratory BC aerosols emitted from Siberian peat combustion demonstrated a 6 to 11 times increase in total particle count and a decrease in SSA at 405 nm of ~2.4% (Iaukea-Lum et al. 2022). However, observations are more complicated and often show a weaker increase in the absorbing components of particles (Lee et al., 2022). Therefore, the exact effect of BC and biomass-burning (BB) aerosols on the atmosphere is an ongoing field of research.

This study will examine multiple long-range smoke events over the U.S. Southern Great Plains (SGP) to better understand the effects of long-range smoke transport on intensive and extensive aerosol optical properties. By combining several datasets, we aim to answer the following questions:

1. How do wildfire smoke aerosol optical properties evolve during transport from their source fire to the Southern Great Plains during the fire season?
2. How is the change in smoke aerosol optical properties dependent on travel time between the source and the Southern Great Plains?

Understanding the optical properties of smoke and how they change with time and long-range transport will help inform public health decisions, improve environmental equality, expand understanding of aerosols' influence on the Earth's energy budget, and help parameterize climate models. This research aims to examine AOD, SSA, AAOD, EAE, and AAE.

2. Instruments and Datasets

2.a. Ground-based Aerosol Optical Properties from AErosol RObotic NETwork (AERONET)

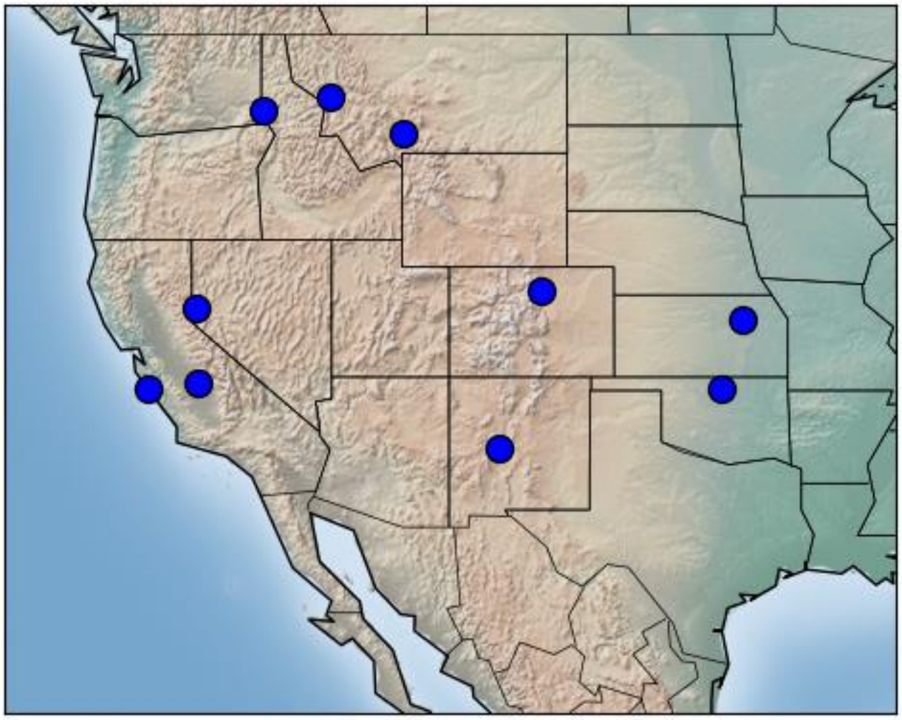

Figure 1 Map of the ten AERONET stations (blue dots) used during this research.

NASA's AERONET was established in 1998 to evaluate satellite retrievals of aerosol loading and properties (Holben et al. 1998) using the standard instrument CE-318 sun-sky radiometer. The CIMEL CE-318 photometer was first made available in 1992 and measures spectral direct Sun, direct moon irradiance, and spectral sky radiances. The CE-318 performs measurements at an approximate field of view of 1.29◦ at ten spectral bands, 1020, 937, 870, 675, 500, 440, 380, and 340 nm. This is accomplished using a silicon photodiode detector and additional measurements at 1020 and 1640 nm using an InGaAs detector (Barreto et al., 2016). AERONET was established by 'NASA's Earth Observing System (EOS) and has been expanded by many non-NASA institutions. This network of instruments then retrieves direct Sun and sky radiances. The former is used to measure AOD, EAE, and Fine Mode Fraction, while the latter is used to infer aerosol characteristics with the Dubovik and King (2000) inversion algorithm such as SSA, size distribution, AAE, etc. (Dubovik et al. 2000). The Version 3 algorithm enhances its predecessor by being fully automated. This automation is achieved by comparing AOD calculations with both pre-field and post-field calibrations. (Giles et al. 2019). AERONET data quality is separated into Level 1.0, Level 1.5, and Level 2.0. NASA AERONET defines Level 1 as prescreened data, Level 1.5 as near-real-time automatic cloud screening and automatic instrument anomaly quality controls, and Level 2.0 also applies pre-field and post-field calibrations (Giles et al. 2019). Sites used in this study are listed in Table 1 and are categorized in Level 2. This investigation uses AOD (500 nm), EAE (440-870 nm), fine mode fraction, SSA (440 nm), and AAE (440-870 nm). The primary source of computed AOD uncertainty comes from calibration, which is approximately 0.010-0.021 for field instruments, with higher errors in the ultraviolet (Eck et al. 1999). The calibration of sky radiances achieves an absolute accuracy of approximately 5% against frequently characterized integrating spheres at the NASA Goddard Space Flight Center (Holben et al. 1998).

State	City	AERONET Site	Longitude/Latitude	Elevation (m)
California	Fresno	Fresno_2	199.77° W - 36.78° N	100
California	Monterey	Monterey	121.85° W - 36.59° N	50
Nevada	Reno	Univ_of_Nevada-Reno	119.81° W - 39.54° N	1410
Montana	Missoula	Missoula	114.08° W - 46.92° N	976
Montana	Bozeman	Bozeman	111.04° W - 45.66° N	1507
Idaho	Rimrock	Rimrock	116.99° W - 46.49° N	824

New Mexico	Sevilleta	Sevilleta	106.88° W - 34.35° N	1477
Colorado	Longmont	NEON_CVALLA	105.17° W - 40.16° N	1539
Kansas	Ashland	NEON_KONZ	96.56° W - 39.10° N	415
Oklahoma	Billings	ARM_SGP	97.49° W - 36.60° N	319

Table 1 State, city, name, coordinates, and elevation (m) of AERONET sites used in this study.

2.b. In-situ Aerosol Optical Properties from the Department of Energy (DOE) Atmospheric Radiation Measurement (ARM) User Facility

Nephelometers and Particle Soot Absorption Photometers (PSAP) are part of the standard Atmospheric Radiation Measurement (ARM) aerosol observing system (AOS) equipment. An integrating nephelometer measures total light scattering (β_{sca}) and hemispheric backscattering. The scattering properties of aerosols are determined by subtracting the scattering from the environment from the scattering of the particle. The scattered light is split into three color bands: red (700 nm), green (550 nm), and blue (450 nm), which are then captured by photomultiplier tubes (Uin 2024). Nephelometers deployed at ARM sites typically do so in pairs. One instrument measures the ambient conditions, while the other measures scattering as a function of slowly increasing or decreasing relative humidity (RH) (Feng et al. 2023). Systematic uncertainty becomes the dominant source of uncertainty for particle scattering coefficients above about 10^{-6} m^{-1} and averaging times longer than about 60 seconds. According to Anderson and Ogren 1998, modeling and experimental results show systematic uncertainty within ±10%.

Radiance Research PSAPs determine the optical extinction coefficient by measuring transmittance through glass/cellulose filters. As particles collect on the filter, the change in transmittance is compared to that of a reference filter. The accuracy of the PSAP is not generally agreed on in the community. Several corrections to PSAP data are discussed by Bond et al., 1999, however, for aerosols with high single-scattering albedo, the scattering correction can be up to 50% of the original measurement. Sensitivity for the PSAP with no dilution is taken as 3 X σ or 0.3 Mm-1 for 60-s averaging of intensities (Springston 2018).

2.c. Ground-based Backscattering from Micro Pulse Lidar (MPL)

The MPL is an automated ground-based lidar that transmits short pulses of laser light to detect the portion backscattered by atmospheric particles. The ARM SGP site operated a non-polarized MPL until August 2006. After this, dual-polarization lidars were adopted to detect backscattering light co-polarized (parallel) and cross-polarized (perpendicular) channels. The beam emitted by the lidar operates at 532 nm, is 3 m long, and switches polarization states every 3 – 10 seconds (Muradyan and Coulter 2020). Welton et al. 2002 showed that near the surface, overlap uncertainty dominates, which is signal loss in the near range due to the poor receiver efficiency of the telescope and associated optics. However, above the overlap region, the dominant uncertainty is from uncertainty in energy.

2.d. Satellite Retrievals of AOD

We used AOD from the Deep Blue (DB) algorithm (Hsu et al. 2004a) to observe the seasonal variation of AOD across the U.S. and identify transport paths to the SGP. The DB algorithm was created with the goal of improving AOD retrievals over arid, semi-arid, and urban environments, and the principal concept behind the DB algorithm was to view land surfaces that are bright in the red spectrum of visible light in their comparably darker blue spectrum. After cloud screening, AOD and aerosol type are determined simultaneously using look-up tables to match the satellite-observed spectral radiances (Carboni et al. 2012). For this investigation, we used the DB algorithm from the Moderate Resolution Imaging Spectroradiometer (MODIS) sensors onboard the Terra and Aqua satellites (Barnes and Salomonson 1992). The instrument was launched aboard ' 'NASA's Earth Observing System (EOS) Terra spacecraft on December 18, 1999, and their Aqua spacecraft on May 4, 2002 (Barnes et al. 2003). For our investigation, we used DB retrievals with quality assurance (QA) flag 3 (Sayer et al. 2013). The DB retrievals show root mean square error (RMSE) compared to AERONET of ~0.04 over bright and~0.01–0.02 over darker (e.g., vegetated) land surfaces (Sayer et al. 2015).

2.e. Back Trajectory Analysis

The National Oceanic and Atmospheric Administration (NOAA) Air Resources Laboratory (ARL) created the first version of the HYbrid Single-Particle Lagrangian Integrated Trajectory HSYPLIT model in the early 1980s (Draxler and Taylor 1982). Version 4 of HYSPLIT serves as the basis of the current model and was released in 1998. The model is a system for computing simple trajectories to complex dispersion and deposition simulations using puff or particle approaches over Polar, Lambert, or Mercator map projections (Draxler and Hess 1997). While the puff approach simulates an expanding puff that will split into smaller groups of particles after reaching the size of a grid cell, a particle approach simulates a fixed number of particles. HSYPLIT Version 4 calculates the dispersion rate from the vertical diffusivity profile, wind shear, and horizontal deformation of the wind field and three-dimensional particles, puffs, or hybrid Lagrangian representations (Stein et al. 2015). Draxler & Hess, 1998 offer a more detailed overview of the HYSPLIT Version 4 model. This research used the North American Model (NAM) at 12 km resolution as the meteorological data for our HYSPLIT back trajectory models.

2.f. ERA5 Reanalysis

Atmospheric data used in this work was collected from ERA5 reanalysis. ERA5 is based on the Integrated Forecasting System (IFS) Cy41r2, which was operational in 2016 and is the fifth generation of ECMWF reanalysis. ERA5 has a horizontal resolution of 31 km, hourly output, and 137 levels between the Earth's surface and 0.01 hPa (Hersbach et al. 2020). Compared to the previous ERA-Interim, ERA5 provides an uncertainty estimate for each product and has a much shorter latency of 5 days rather than 2 – 3 months. Reanalysis data for this work was collected over the continental United States between 10 am and 2 pm (corresponding to MODIS pass over times) for specific smoke event days between 2015 and 2022.

Table of Datasets

	Name	Agency	Variables	Spatial Temporal Resolution	
Instrument and Satellite	MODIS (Barnes and Salomonson 1992) Terra and Aqua	NASA	DB AOD_{500nm}(Sayer et al. 2014; Hsu et al. 2004b, 2013)	10x10 km^2	daily
Model or Reanalysis	NAM (Information (NCEI) n.d.)	NOAA	P_{surf}, P_{msl}, T_{surf}, T_{2m}, DWT_{2m}, orography, RH_{2m}, U_{10m}, V_{10m}, land mask, vegetation, PBLH	12x12 km^2	6 hours
	HYSPLIT (Stein et al. 2015)	NOAA	Back and forward trajectories and smoke dispersion	12x12 km^2	hourly
	ERA5 (Hersbach et al. 2020)	ECMWF	$U_{500\ hPa}$, $V_{500\ hPa}$, geopotential height	31x31 km^2	hourly

Instrument and Network	AERONET (Giles et al. 2019)	NASA	AOD$_{500nm}$, EAE$_{440\text{-}870nm}$, AAE$_{440\text{-}870nm}$, SSA$_{440nm}$	Point location	<1 hour
	MPL (Campbell et al. 2002)	NASA	Back_sca$_{559\ nm}$	Point location	<1 hour
	Nephelometers (Feng et al. 2023)	DoE	Back_sca$_{500\ nm}$, Back_abs$_{500\ nm}$	Point location	<1 hour

Table 2 List of instruments and datasets used in this research with owning agency, variables, spatial, and temporal resolution.

3. Methods

3.a. Identification of Smoke Events

This research's spatial domain was established from the western U.S. to the Southern Great Plains (SGP) region, specifically Oklahoma. To account for AERONET site relocation and overlap, retrievals from sites within 25 km of each other were combined. The 10 sites listed in Table 1 were selected because they had continuous data sets (at least one data point for each year) from 2015-2022. This research examined Level 2 AOD at 500 nm, EAE at 440-870 nm, SSA at 440 nm, and AAE at 440-870 nm at each AERONET site. To identify the months with the highest long-range smoke transport signal, we calculated the monthly averages of AOD using daily Deep Blue AOD at 550 nm data retrieved from Aqua and Terra satellites for each month. These AOD maps were created with a grid of 10x10 km^2 in both longitude and latitude, spanning from 128° W, 50° N to 66° W, 24° N. The maps were also overlaid with points indicating each of the ten AERONET sites and their monthly AOD averages (Figure 1). Specifically, we observed AOD over the western U.S. during the peak of the fire season (August and September), noting a steady increase beginning in June. We then compared the daily AOD averages at 500 nm at each observed AERONET site over the subsequent months. Using real-color images from Aqua and Terra, this data was utilized to create a list of smoke events originating in Canada, Mexico, or the western U.S. transported over the Southern Great Plains (Billings, OK, ARM_SGP) site.

3.b. Estimating Travel Time with Back Trajectory Analysis

To properly evaluate the evolution of aerosol properties, we conducted back trajectory analysis to investigate the path and travel time of specific smoke events. We utilized the North American Model (NAM) at 12 km resolution as the meteorological data for our HYSPLIT back trajectory models. The starting height of our parcel back trajectories over the ARM_SGP site (Billings, OK) was determined using the mean average plume height for each smoke event, found using Billings, OK's MPL. Each MPL attenuated backscatter profile was divided by the attenuated Rayleigh backscatter profile to remove the ambient pressure dependence of the lidar profile, making it easier to discern weak aerosol signals. The height of the maximum backscattering ratio was identified for each smoke event and used as its HYSPLIT parcel height. Although this method increased the accuracy of the HYSPLIT trajectories, the availability of cloud-free MPL data at the ARM SGP Facility limited the temporal domain of our work to events starting in 2015. After setting our starting parameters, HYSPLIT simulations were able to approximate the path and travel time for each parcel.

3.c. Comparison of AERONET and Nephelometer Data

With an established path and travel time for each smoke event, we compared AERONET stations along the path. Travel time was recorded in the nearest number of days from the event's start. Regardless of location, each event's closest station to the source fire was also noted. Observations of AOD, SSA, EAE, and AAE were collected from the AERONET site near the fire source at the start of the event and the Billings, OK site a number of days later based on the travel time. These 24-hour periods were compared to observed changes and the evolution of the smoke's physical properties. Observations in Billings, OK, at the ARM_SGP site were further compared to nephelometer measurements on site. Specifically, $AOD_{500\ nm}$ was compared to $\beta_{s\ 550\ nm}$ to examine when smoke aerosols arrived near the surface and approximate quantity.

4. Results

4.a. DB satellite retrievals of AOD over CONTinetal United States (CONUS) from 2015 to 2022

Given long-range transport was the focus of this work, we needed to establish the temporal domain (monthly trends) when mean AOD peaks due to wildfire smoke. Specifically, we identified when there were elevated paths of AOD between the Western U.S., Canada, or Mexico and the AERONET site in Billing, OK. Figure 2 shows the monthly means of AOD from DB (550 nm) and AERONET (500 nm) sites from 2015 to 2022. Qualitatively, we observed that our AERONET sites generally agreed with the surrounding DB AOD retrievals.

We utilized satellite retrievals of DB AOD to identify smoke transported from various regions of the U.S. and its temporal dominance in the Southern Great Plains. Beginning in January (Fig. 2.a), the entire United States exhibited a relatively low AOD signal (AOD < 0.1). As the months progressed from February to May (Fig. 2.b-e), a stronger mean AOD signal developed across the eastern half of the U.S., extending from the Dakotas and the SGP to the eastern U.S. While pockets of elevated mean AOD (~0.25 – ~0.4) were observed in California, Utah, and Nevada within the western U.S., the majority of the western U.S. maintained a mean AOD within the range of 0.0 – 0.1. Conversely, the eastern U.S. exhibited AOD values ranging between approximately 0.1 and 0.2, approaching 0.4 around the Great Lakes and into Canada's Ontario and Quebec territories. In May (Fig. 2e), mean AOD values indicated an increasing trend of aerosol loading (between 0.1 – 0.2) developing between the SGP and the Alberta and Saskatchewan regions of Canada, as well as a continuous increase in the eastern U.S.

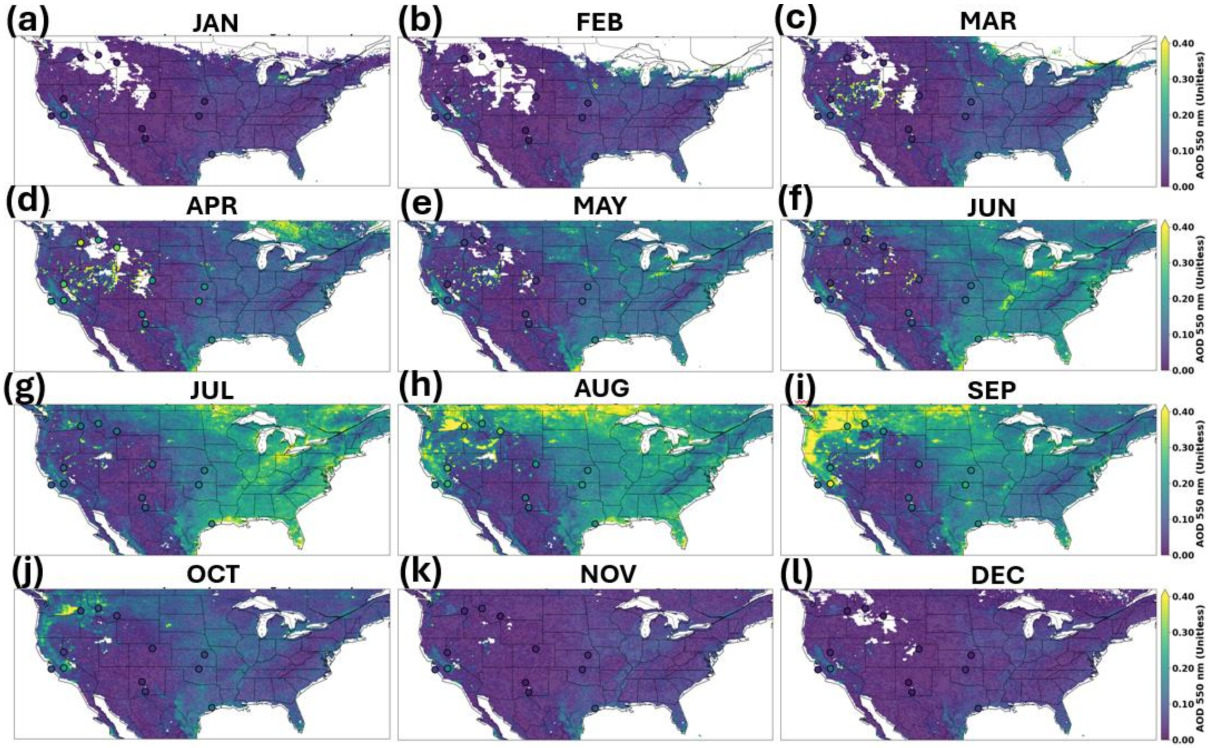

Figure 2 Monthly averages of DB AOD (550 nm) from MODIS Terra and Aqua from 2015 to 2022. Circles represent the monthly averages of AERONET AOD (500 nm).

The continued development of this AOD pathway between the SGP and Canada, along with the increasing occurrence of mean AOD peaks (~0.2) in Washington and Oregon, led us to define the beginning of our temporal domain in June (Fig. 2f). The elevated mean AOD in the eastern U.S. peaked in July (Fig. 2g), with mean values ranging between 0.2 and 0.3, and many regions reaching values ≥ 0.4. Notable regions included the Gulf Coast along Louisiana (~0.3 – ~0.4), the southern tip of Florida, the northern region of Minnesota (>0.3), and the Ohio coast of the Great Lakes (~0.35 – ~0.4). While some regions in the western U.S. (e.g., Arizona, Utah, New Mexico, and Colorado) did not exhibit strong signals for high mean AOD, with few values reaching 0.1 across any month, the western U.S., Northwest U.S., and lower Canada regions trended upwards between July and September (Fig. 2.g-i). The peak mean AOD for the Canadian and U.S. border was observed in August (>0.4) (Fig. 2h), while the areas around California, Oregon, Washington, and Idaho peaked in September with much of the region >0.4. Mean AOD across the entire U.S. began to decrease in October (Fig. 2j), with some regions in the Northwest, such as parts of Washington, still exhibiting average values ≥ 0.4. In November and December (Fig. 2.k-l), values across the entire observed region returned to 0 and 0.1, similar to January. While evidence of local and prescribed fires in the eastern U.S. was apparent between March and July, a visible AOD pathway between the West Coast and the SGP was dominant in August and September. Consequently, we established the temporal domain of our study to be between June and September of 2015 – 2022, when AOD was elevated between the western U.S. and SGP, likely indicating the wildfire season with higher average peaks at the SGP in August and September.

4.b. Identification of smoke using AERONET stations from the western U.S. to the SGP

In Figure 3, we aim to identify elevated AOD signals from the DB AOD maps (Figure 2) attributable to long-range transport by observing AOD loadings at distant AERONET sites and the one located at the SGP (Billings, OK). Further details about each AERONET site, including coordinates and elevation, can be found in Table 1. Figure 3 illustrates the distribution of 500 nm AOD measured at eight AERONET sites (Fresno, CA; Rimrock, ID; Reno, NV; Longmont, CO; Missoula, MT; Flint Hills, KS; Sevilleta, NM; and Billings, OK), categorized by month (August and September) from 2015 to 2022. Several spikes in Aerosol Optical Depth (AOD) were observed at various sites, suggesting long-range transport. For example, in September 2020, Fresno, CA recorded the highest AOD values for September across all AERONET sites, with a mean AOD of ~0.96, a median of ~0.65, and a standard deviation (SD) of ~0.96. In comparison, Reno, NV, and Billings, OK also exhibited high aerosol loading, with Reno, NV showing a mean

AOD of ~0.59, an SD of ~0.82, and a median of ~0.24, while Billings, OK had a mean AOD of ~0.57, an SD of ~0.48, and a median of ~0.29. Although the values at Reno, NV, and Billings, OK, were lower than those at Fresno, CA, they were outside the expected range when compared to other years. Reno's AOD mean was 0.51 higher than in years without major fire events, while Billings, OK AOD's was ~0.44 higher.

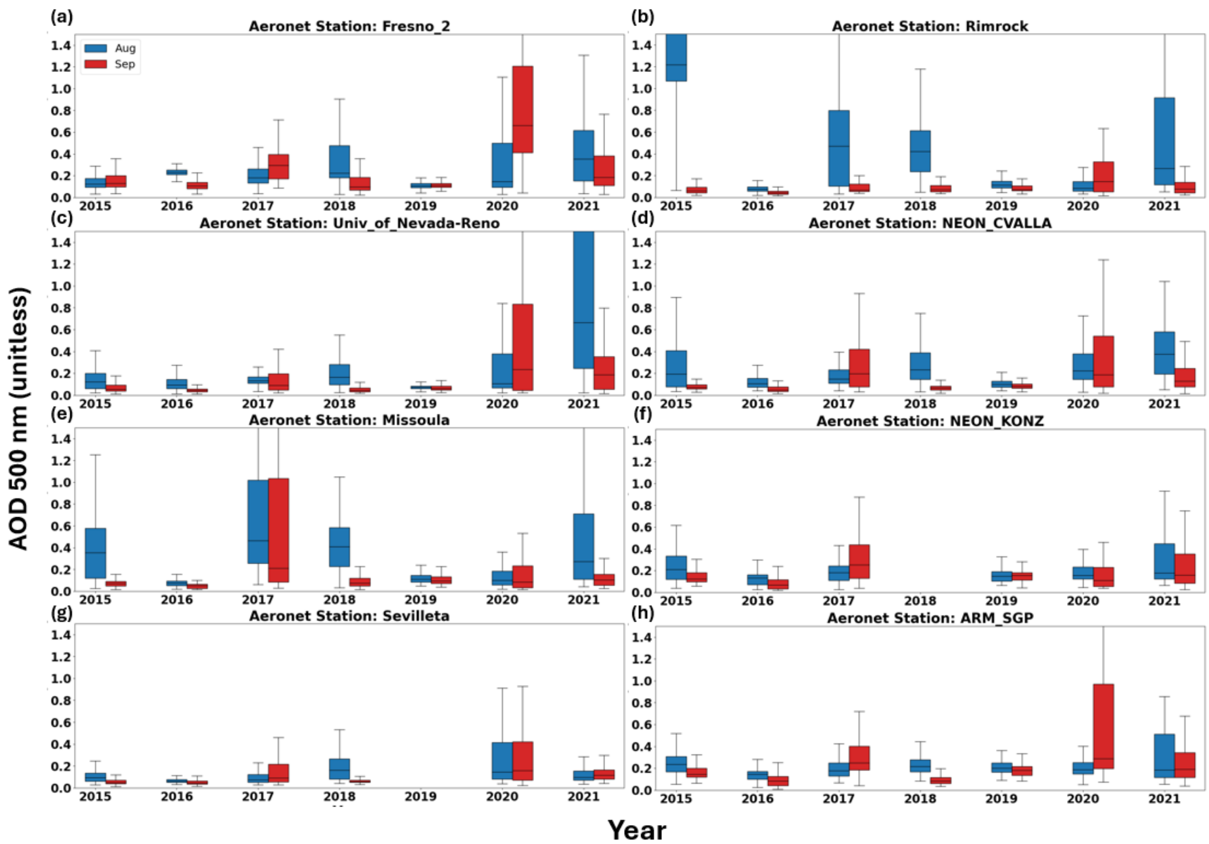

Figure 3 Box-and-whisker plots of AERONET AOD500 nm (unitless) recorded in August and September from 2015-2021 for the sites in Fresno, CA (a), Rimrock, ID (b), Reno, NV (c), Longmont, CO (d), Missoula, MT (e), Ashland, KS (f), Sevilleta, NM (g), and Billings, OK (h).

This strongly indicates that a fire event in September 2020 in Fresno, CA, produced smoke that underwent long-range transport to Billings, OK. Additionally, in August 2021, the Reno, NV site observed a spike in AOD, with a mean AOD of ~0.94, larger than that of the 2020 Fresno, CA event. This elevated AOD was detected at distant sites such as Missoula, MT, and Billings, OK.

Missoula showed a mean AOD of ~0.54, an SD of ~0.62, and a median of ~0.27, while Billings, OK, had a mean AOD of ~0.30, an SD of ~0.22, and a median of 0.19. Another notable spike in AOD occurred in September 2017, when Missoula registered high levels of AOD (mean ~0.69). Although smaller than 2020, Billings, OK, observed an elevated mean AOD of ~0.31, which was ~0.17 higher compared to non-event years (i.e., 2015, 2016, 2018, and 2019), indicating long-range transport likely from a Northwest region fire. Additional months and years outside of the domain of this work can be found for each station in Appendix A.

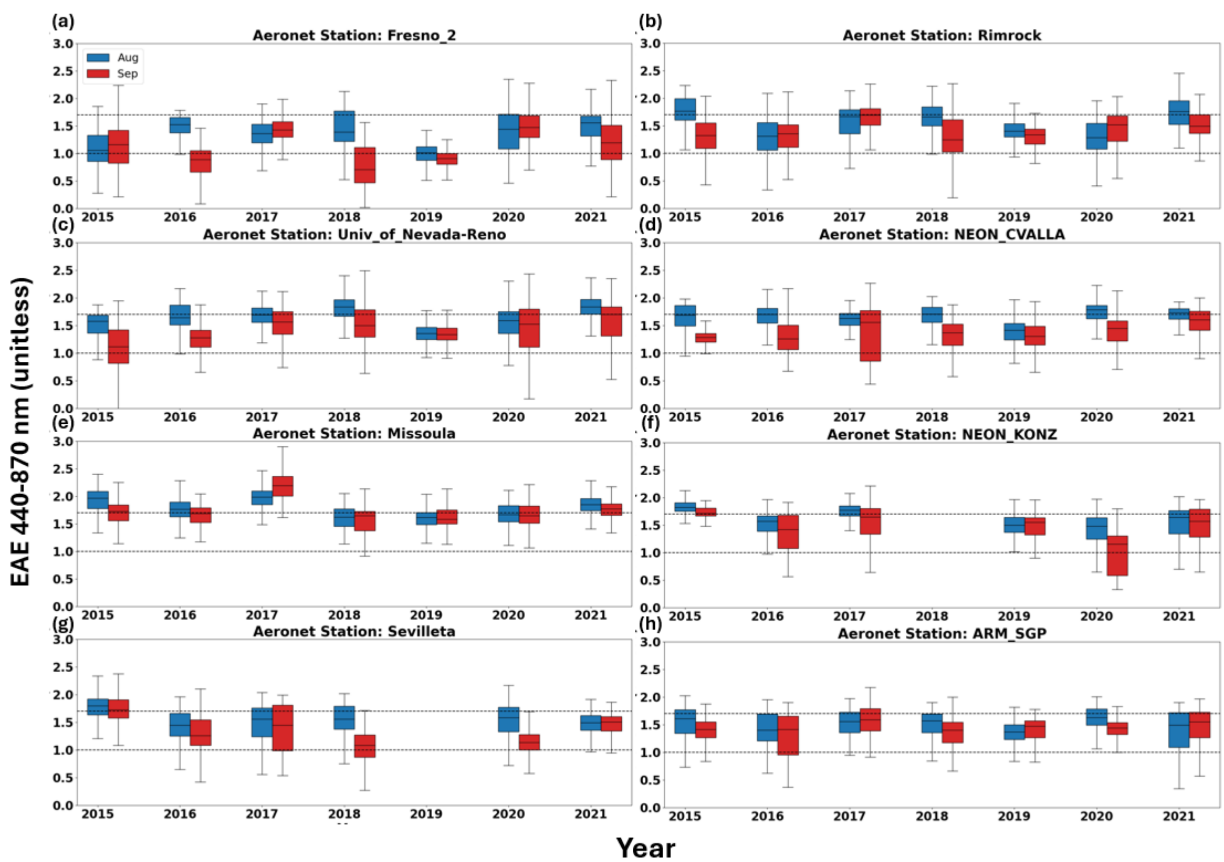

Figure 4 Box-and-whisker plots of AERONET EAE440 – 870 nm (unitless) recorded in August and September from 2015-2021 for the sites in Fresno, CA (a), Rimrock, ID (b), Reno, NV (c), Longmont, CO (d), Missoula, MT (e), Ashland, KS (f), Sevilleta, NM (g), and Billings, OK (h). The Dashed lines at 1.7 and 1.0 represent fine and coarse mode, respectively.

These observations are further substantiated by examining the EAE at each site (Figure 4). In September 2017, Missoula recorded a mean EAE of ~2.2 (SD ±0.27), well within the fine mode range (EAE > 1.7). Notably, 2017 exhibited the highest mean EAE observed in Missoula and the second highest at Billings, OK, with a mean EAE of 1.58 (SD ±0.26). Similarly, this elevated EAE at Billings, OK, was only surpassed in August 2020, when the site recorded a mean EAE of ~1.62 (SD ±0.21). The 2020 increase in EAE was also observed at Reno (mean EAE ~1.56, SD ±0.28), Longmont, CO (mean EAE ~1.71, SD ±0.27), and Bozeman (mean EAE ~1.64, SD ±0.26). These long-range transport examples were visually confirmed using Terra and Aqua true color imagery using NASA Worldview (Appendix B). A list of smoke events was then created by observing satellite retrievals and AERONET data for visible smoke and fire anomalies (Fire radiative power).

Date (yyyy/m/d)	Day 1 Source Station	Travel Time to SGP (days)
2017/9/2	Missoula	2
2017/9/8	Rimrock	2
2017/9/8	Missoula	2
2017/9/11	Missoula	3
2017/9/11	Rimrock	3
2020/8/15	NEON_CVALLA	1
2020/8/23	Rimrock	2
2020/9/6	Fresno_2	4
2020/9/7	Fresno_2	4

2020/9/7	Univ_of_Nevada-Reno	1
2020/9/12	Rimrock	3
2020/9/12	Monterey	0
2020/9/13	Monterey	4
2020/9/19	Univ_of_Nevada-Reno	3
2020/10/1	NEON_CVALLA	1
2021/7/13	NEON_KONZ	0
2021/8/3	Rimrock	2
2021/8/3	NEON_KONZ	1
2021/8/6	Missoula	3
2021/8/9	Univ_of_Nevada-Reno	4
2021/8/9	Bozeman	3
2021/9/1	Univ_of_Nevada-Reno	2
2021/9/10	Univ_of_Nevada-Reno	1
2021/9/10	Bozeman	1
2021/9/13	Univ_of_Nevada-Reno	3
2022/5/8	Sevilleta	0

2022/9/13	Missoula	2

Table 3 Arrival date, nearest source station, and travel time for smoke events that reached Billings, OK. Rows are color-coded based on the travel time from the source station to SGP: blue for zero days, orange for one day, green for two days, pink for three days, and brown for four days.

4.c. Comparison of aerosol optical properties between western U.S. and SGP by travel time

Here, we compared how travel time influences the optical properties retrieved from the source of smoke events in Table 3 and the Billings, OK site.

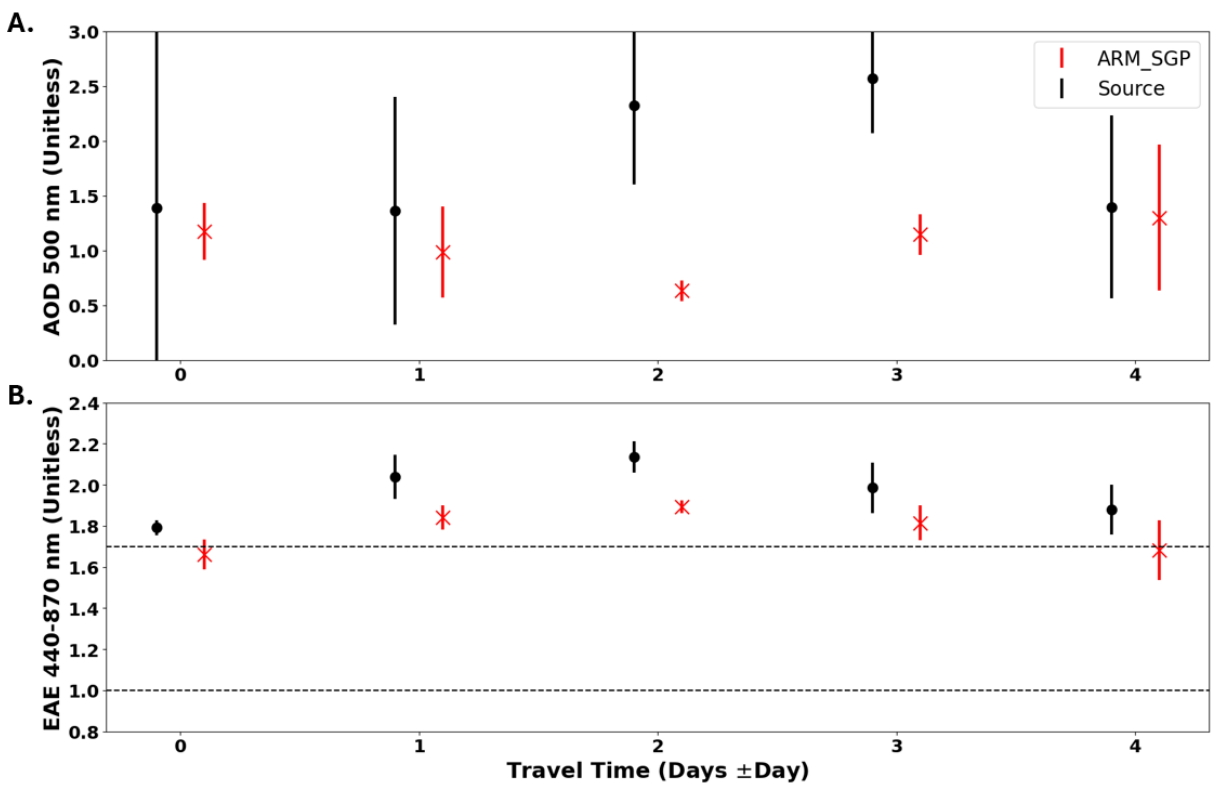

Figure 5 Plot comparing AOD500 nm (unitless) (a.) and EAE440 – 870 nm (unitless) (b.) retrievals at Billings, OK (red) and Source Station (black) grouped by travel time in days ± 1 day. Points show mean while lines are one standard deviation. The dashed lines at 1.7 and 1.0 in 5.b. represent fine mode and coarse mode, respectively.

After travel time in days to the SGP was determined for each smoke event in Table 3 using HYSPLIT back trajectories, events were grouped into bins by travel time. The AOD and

EAE of each travel time bin were then averaged at the Billings, OK (red), and source (black), respectively, and compared in Figures 5 and 6. The quantitative results from these figures are listed in Table 4. To focus on smoke plume coverage and minimize clear sky measurements, the values in these figures were restricted to the upper quartile of data points. This approach ensures that the analysis specifically examines smoke.

Travel Time (days)	0 (±1)		1 (±1)		2 (±1)		3 (±1)		4 (±1)	
	Source	ARM_SGP	Source	ARM_SGP	Source	ARM_SGP	Source	ARM_SGP	Source	ARM_SGP
$AOD_{500\ nm}$ N	155	152	273	337	302	306	317	402	298	222
$AOD_{500\ nm}$ ±SD	1.39 (±1.83)	1.18 (±0.26)	1.36 (±1.04)	0.98 (±0.41)	2.32(±0.72)	0.63(±0.09)	2.57(±0.5)	1.15(±0.18)	1.39(±0.84)	1.29(±0.67)
$EAE_{440\text{-}870\ nm}$ N	162	153	279	363	330	306	347	405	307	229
$EAE_{440\text{-}870\ nm}$ ±SD	1.79 (±0.4)	1.66 (±0.07)	2.04 (±0.11)	1.84 (±0.06)	2.14 (±0.08)	1.89 (±0.03)	1.99 (±0.12)	1.81 (±0.09)	1.88(±0.12)	1.68 (±0.15)
$SSA_{440\ nm}$ N	1	2	6	15	7	10	3	25	11	5
$SSA_{440\ nm}$ ±SD	0.96 (<0.01)	0.94 (±0.01)	0.98(<0.01)	0.96 (±0.01)	0.97(±0.01)	0.97 (±0.01)	0.97 (<0.01)	0.95 (±0.01)	0.96 (<0.01)	0.95 (±0.01)
$AAE_{440\text{-}870\ nm}$ N	1	2	6	15	7	10	3	25	11	5
$AAE_{440\text{-}870\ nm}$ ±SD	0.82 (<0.01)	2.08 (±0.01)	1.33 (±0.04)	1.49 (±0.04)	1.43 (±0.03)	1.47 (±0.06)	1.44 (±0.04)	1.78 (±0.21)	1.66 (±0.28)	1.98 (±0.08)

Table 4 List of number N of samples and mean ± SD for AOD500 nm, EAE440 – 870 nm, SSA440 nm, and AAE440-870 nm sorted by travel time in days ± 1 day retrieved at the smoke event source and after arrival at Billings, OK (ARM_SGP AERONET site).

Results from Figure 5a show that for all travel times, the mean AOD is always lower at Billings, OK, compared to the source station, regardless of travel time. This indicates that the loading of smoke aerosols emitted at the fire event source decreases approaching the Billings, OK, site due to dry and/or wet depositions. At zero and one-day travel times, less AOD is dispersed between the source site and Billings, OK, with a mean difference of ~0.21 at zero days and ~0.38 at one day, indicating that shorter travel time gives the aerosols less opportunity to undergo deposition. By comparison, a longer travel time of two or three days results in a larger variation in AOD between the source site and Billings, OK, with mean differences of ~1.69 and ~1.42, respectively. However, this trend does not apply to a travel time of four days, which shows only a mean difference of ~0.1. Further investigation reveals that this is due to smoke plumes from other sources overlapping with the travel of the plumes from the observed four-day events. Specifically, both the September 6th and 7th, 2020 events from Fresno, CA, overlap with each other and the September 7th event from Reno, NV (Appendix B7 and B8).

Additionally, the September 13th, 2020, event from Monterrey, CA, overlaps with the September 12th events from Monterrey, CA, and Rimrock, ID (Appendix B9 and B10), and the August 9th, 2021, event from Reno, NV overlaps with August 6th and 9th events from Missoula, MT and Boseman, MT respectively (Appendix B15 and B16). It is also important to note the difference in standard deviation between the source site and the Billings, OK, location. The standard SD at the source for each travel time varied, with the highest SD at zero days (~1.83) and the lowest at three days (~0.5). Meanwhile, the Billings, OK SD ranged from ~0.18 at three days to ~0.72 at two days. The large SD at the source is likely due to variations in local weather conditions, such as wind direction, boundary layer entailment microphysics, and variability in burn rate.

Similarly, Figure 5b shows that EAE at the source location is greater than at Billings, OK, for all travel times, indicating that particles are larger upon arrival. For example, the largest difference in EAE occurred at a travel time of two days, with a decrease of ~0.25. In contrast, the smallest difference, only ~0.13, occurred at zero days travel time. Travel times of one, three, and four days resulted in values within this range, specifically ~0.2, ~0.18, and ~0.2, respectively. This change in EAE occurs because, as the particle travels, it builds a coating primarily composed of organic matter. This observation aligns with Sedlacek et al. (2022), who examined the lifetime of tropospheric BC aerosol coatings and found that this coating develops within the first 1 to 2 hours of the particle's lifetime. The coating size remains constant for 1 to 2 days before beginning to decay. However, the decay rate is two orders of magnitude slower than the initial growth rate, making a decrease in coating size unlikely to be observed within the time scale of this study.

Additionally, there is a noticeable trend of increased EAE (particle size decrease) as travel time increases. The smallest observed mean EAE occurred at a zero travel time with ~1.79 (±0.04) at the source and ~1.66 (±0.07) at Billings, OK. The largest mean EAE occurred at two days of travel, ~2.14 (±0.08) at the source and ~1.89 (±0.03) at Billings, OK. This may be because more intense fires release smaller particles due to more complete combustion and generate greater injection height, allowing them to travel further. However, similarly to AOD, a four-day travel time increased mean EAE of ~1.88 (±0.12) at the source and ~1.68 (±0.15) at Billings, OK, likely due to the mixed plume injection described above.

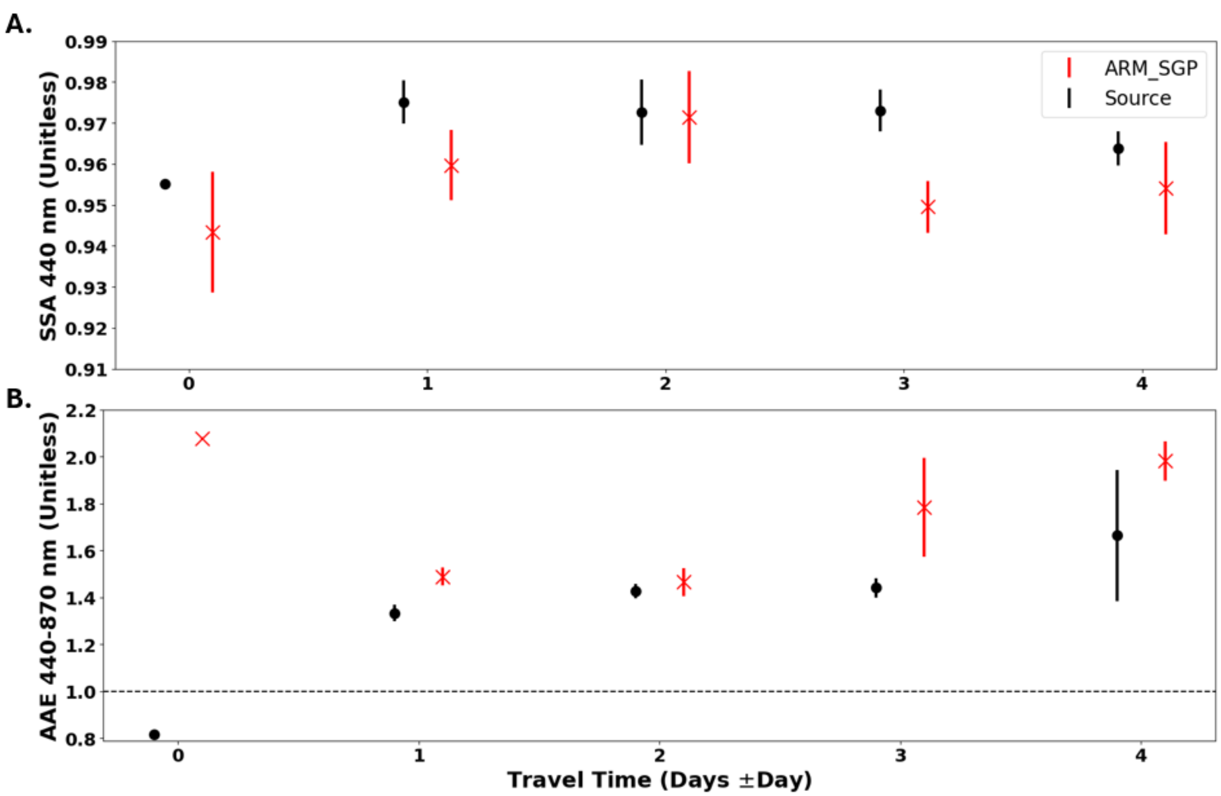

Figure 6 Plot comparing SSA440 nm (unitless) (a.) and AAE440 – 870 nm (unitless) (b.) retrievals at ARM_SGP (red) and Source Station (black) grouped by travel time in days ± 1 day.

Points show mean while lines are one standard deviation. The dashed line at 1.0 in 6.b. represents the theoretical value for BC.

Figure 6 further examines aerosol optical properties as they change with travel time with SSA and AAE. It is important to note the small sample size and lack of robustness of statistical significance (see Table 4), with the largest bin containing 25 points and the smallest only containing 1. This lack of data points is due to AAE and SSA being derived from AERONET inversion algorithms. AERONET requires an AOD of greater than 0.4 at a wavelength of 440 nm to derive these properties, and Level 2 data quality control further limits retrievals.

For SSA (Figure 6a), all values are higher at the source than in Billings, OK for all travel times, indicating that the particles are brighter at the source than at the ARM site. This observation aligns with Sedlacek et al. (2022), as the organic coating formed within the first hours of the aerosol's life increases its scattering component by decreasing the ratio of BC to organic material. Values close to ~0.9 should persist for the first four days until the coating breakdown increases the ratio of BC, thereby lowering SSA. Variations in SSA within the first four days may be due to photochemical reactions in the atmosphere that, while not decreasing the coating size, do alter its scattering properties. Our observations indicate values in the ~0.9s, with a ~0.02 decrease for zero, one, and three-day travel times, a less than ~0.01 decrease for two days, and a ~0.01 decrease for four-day travel events.

Inversely, all values for AAE (Figure 6b) are greater in Billings, OK, than at the source for all travel times, indicating the smoke is closer to BrC than BC upon arrival. Of the four travel times, zero-day events at their source exhibited the closest measurement to BC at a mean AAE of ~0.82 and the highest measurement of AAE in Billings, OK, with a mean AEE of ~2.08. One and two-day events showed less extreme differences between source and Billings, OK, with a difference of ~0.16 and ~0.04, respectively. While the source AAE of three days is similar to one and two days (~1.44), the difference to Billings, OK, was ~0.34, and the mean AAE of ~1.78 was within the range of BrC. Finally, with a difference of ~0.32, four days was the only event bin with a source (~1.66) and arrival value (~1.98) within the range of BrC.

4.d. Connecting Smoke Events AOD Retrievals with Ground Nephelometer Measurements

In Figure 7, we aim to evaluate where smoke arrives over the Billings, OK, site and how that relates to AOD. While AOD is a columnar measurement, ground-based nephelometers take measurements near the surface. This allows us to use $\beta_{sca\ 550\ nm}$ as an estimate for when smoke aerosols are detected near ground level. To further ensure that smoke is being examined and not dust or other particulate matter, the data points in this figure were limited to only those with EAE > 1.4. This threshold was selected to preserve data points that were lost closer to fine mode at EAE > 1.6, such as those of four day events discussed more below. Individual points for AOD and β_{sca} for each event can be viewed in Appendix C and D, respectively.

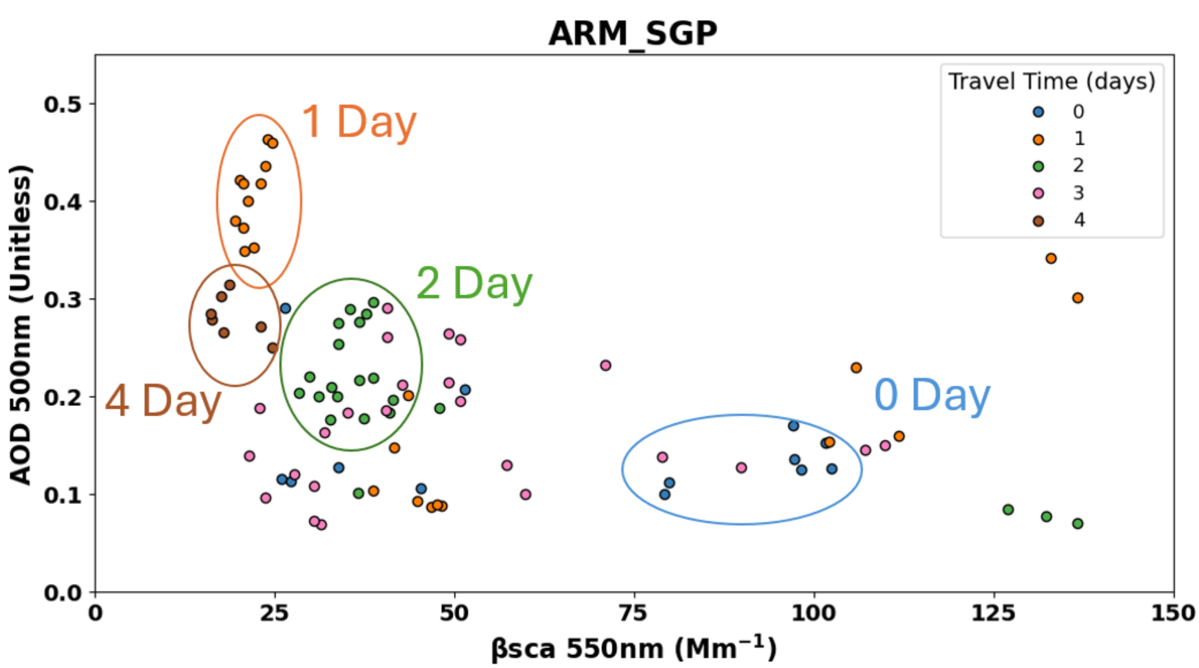

Figure 7 Scatter plot of columnar AOD500 nm versus ground β_{sca} 550 nm. Points are color-coded based on the travel time from the source station to SGP: blue for zero days, orange for one day, green for two days, pink for three days, and brown for four days.

While the data indicates a variety of optical loading and surface proximity across travel times, there are notable groupings of points for zero, one, and two days. The zero-day cluster contains data points from the May 8, 2022, event from Sevilleta, NM, and the September 19, 2020, event from Reno, NV. AOD values for this grouping range from ~0.09 to ~0.17, while β_{sca} $_{550\ nm}$ ranged from ~79.31 Mm^{-1} to ~102.4 Mm^{-1}. These results suggest that the plume from these events mixed down to the surface while loading was low. This is further reinforced by the MPL in Billings, OK, from these events (Appendix B20 and Figure 8c) that show strong backscattering between ~1 km and the surface.

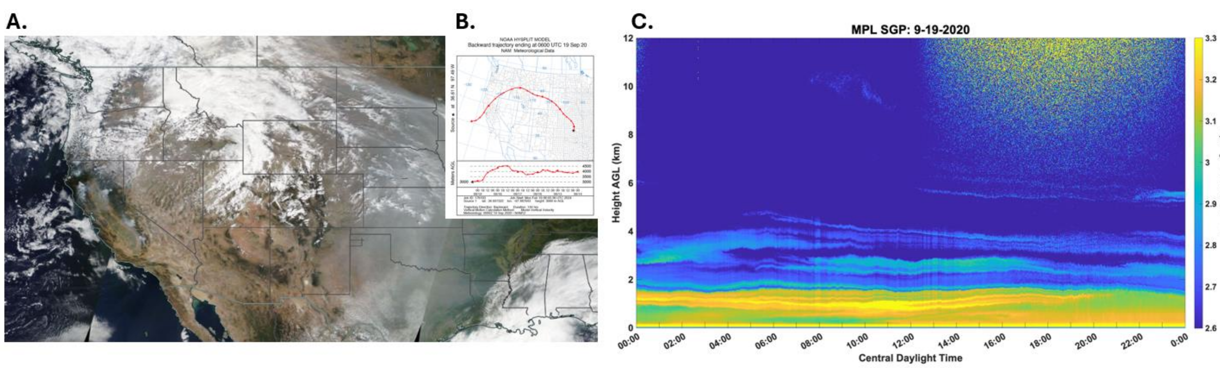

Figure 8 Smoke event data set for September 19, 2020 (a) HYSPLIT back trajectory over Billings, OK, with a starting height of 3000 meters at 600 UTC (b) Terra true color image of smoke over the western U.S. (c) MPL normal relative backscattering retrieval above Billings, OK.

Similarly, the two-day cluster contained points from the August 23, 2020, Rimrock, ID event and the mixed plumes from Missoula, MT, and Rimrock, ID on September 8, 2017. This cluster shows a comparably lower range of β_{sca} $_{550\ nm}$ between ~28.41 Mm^{-1} and ~47.9 Mm^{-1}. This indicates that while these events saw larger values of AOD (~0.17 to ~0.29), there is less evidence of mixing toward the surface. MPL indicates that the August 23, 2020 (Appendix B6) plume arrived at ~4 km, while the September 8, 2017, plumes arrived at ~2 km and ~4 km (Appendix B2). A more extreme example is observed for the cluster of 1-day points from Reno, NV, on September 7, 2020. MPL (Appendix B8) indicates that the plume arrived over Billings, OK, at ~6 km, which supports a lower $\beta_{sca\ 550\ nm}$ between ~19.54 Mm^{-1} and ~24.68 Mm^{-1}. While this plume was likely above the planetary boundary layer, it showed the greatest level of AOD (~0.35 to ~0.46) among the groups observed.

However, increasing the threshold to EAE > 1.6 to be closer to that of fine mode particles removes three groupings of note. First, the cluster of three two-day event points from Rimrock on August 3, 2021, with AOD < 0.1 and $\beta_{sca\ 550\ nm}$ > 125 Mm^{-1} is dropped. This event is notable as it is a mixed plume with a 1-day travel event from Flint Hills, KS, and the MPL and HYSPLIT indicate these points are misattributed. Figures 9b and 9c show the relatively slower-moving Rimrock, ID plume arriving in Billings, OK at ~6 km while the faster Flint Hills, KS plume arrives between ~2 km and the surface. Thus, the elevated $\beta_{sca\ 550\ nm}$ is likely a result of the 1-day travel event.

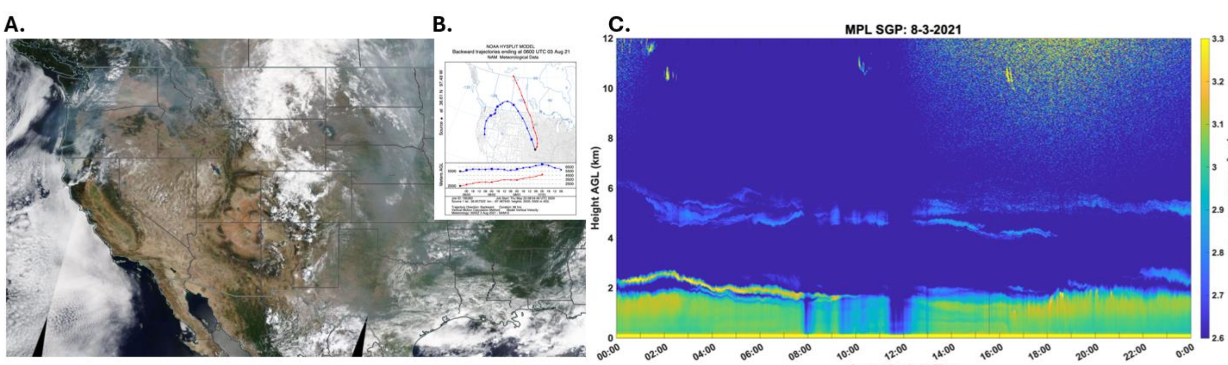

Figure 9 Smoke event data set for August 3, 2021 (a) HYSPLIT back trajectory over Billings, OK, with a starting height of 5500 meters (blue) and 2000 (red) at 600 UTC (b) Terra true color image of smoke over the western U.S. (c) MPL normal relative backscattering retrieval above Billings, OK.

The next lost points are the four-day cluster from Fresno, CA, on September 6, 2020, which showed an elevated AOD between ~0.26 and ~0.31 with a lower $\beta_{sca\ 550\ nm}$ between ~22.74 Mm^{-1} and ~16.35 Mm^{-1}. As discussed above, all four-day events are mixed plumes, resulting in lower overall EAE. This accounts for why this group of points depends on a lower EAE threshold. This plume's path resulted in it arriving above the boundary layer at ~5 km (Appendix B7). Finally, four three-day points from Rimrock, ID, on September 12, 2020, depend on the lower EAE threshold. This event is a unique comparison to the September 19, 2020, event from Reno, NV, because they both result from the same prolonged series of fires along the western U.S. where the Reno, NV plume traveled over the U.S. Canada border before reaching Billings, OK, near the surface, the Rimrock, ID plume was carried over the Pacific Ocean before traveling along the southern U.S. and Mexico (Figure 10a-b). Upon arrival in Billings, OK, the plume was observed with an AOD of 0.07 to 0.09. MPL (Figure 10c) and a $\beta_{sca\ 550\ nm}$ between ~11.1 Mm^{-1} and ~12.03 Mm^{-1} indicate the plume arrived above the boundary layer at ~7.5 km.

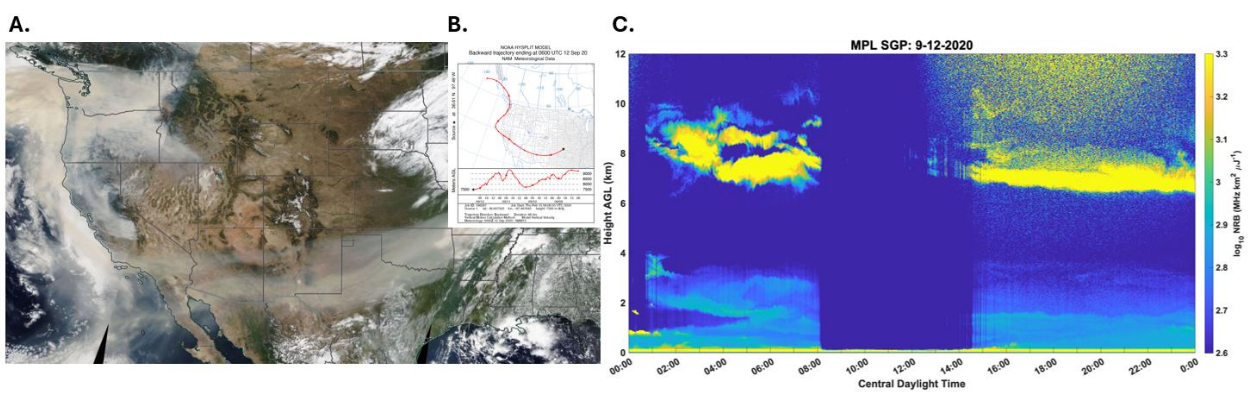

Figure 10 Smoke event data set for September 12, 2020 (a) HYSPLIT back trajectory over Billings, OK with a starting height of 7500 meters at 600 UTC (b) Terra true color image of smoke over the western U.S. (c) MPL normal relative backscattering retrieval above Billings, OK.

4.e. Meteorology Driving Long-Range Transport Pathways and Plume Arrival Height

Figures 11 – 13 aim to further examine the synoptic meteorology driving the long-range transport of individual smoke events to the SGP. Specifically, we looked at 500 hPa geopotential wind maps for the September 12, 2020, event from Rimrock, ID; the September 19, 2020, event from Reno, NV; and the mixed plume on August 3, 2021, from Rimrock, ID, and Flint Hills, KS.

The September 12, 2020, event is defined by a closed low centered over the Colorado and Utah border. The rotation of this low-pressure area resulted in northerly winds between ~10 to ~20 m/s on the first day of travel (September 9, 2020) over the western U.S. (Figure 11a). The fires along the West Coast also substantially modified vertical and horizontal winds due to the smoke-stabilized planetary boundary layer trapping pollution in a shallow boundary layer. The effect was a katabatic and offshore wind anomaly of 3 to 4 m/s easterly near-surface winds created by land cooling (Huang et al. 2023). This further extended the travel time of the plume by carrying it out over the Pacific Ocean. As the closed low progressed to the east, over South Dakota on September 12, 2020, winds over the southern U.S. of ~10 to ~15 m/s would become more westerly, directing the plume over the SGP.

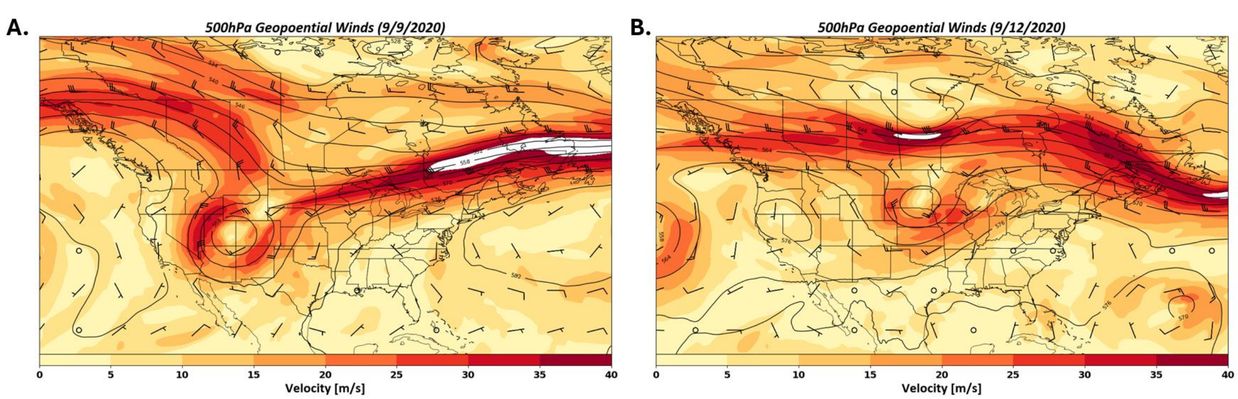

Figure 11 500 hPA height contours over the U.S. with shaded geopotential wind velocity (m/s) and wind barbs indicating wind direction for September 9, 2020 (a) and September 12, 2020 (b).

While these fires resulted in the September 19, 2020, event, the plume underwent an inverse trajectory. On the first day of travel (September 16, 2020), a ridge axis centered over Oklahoma and Texas, extending into the western U.S., resulted in southerly winds of approximately 10 to 15 m/s (Figure 12a). As the trough over the Pacific Ocean pushed the ridge eastward, wind speeds decreased to around 5 to 10 m/s and initially rotated to be more westerly. By September 19, 2020, the winds had inverted to northerly and northwesterly (Figure 12b). This resulted in the arcing path shown in Figure 8b, depositing the plume within the boundary layer over Billings, OK.

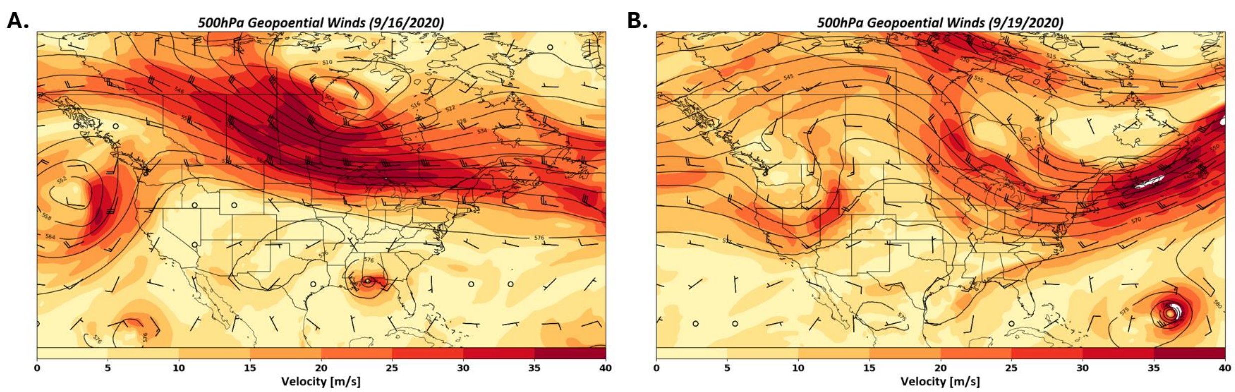

Figure 12 500 hPA height contours over the U.S. with shaded geopotential wind velocity (m/s) and wind barbs indicating wind direction for September 16, 2020 (a) and September 19, 2020 (b).

Similarly to the previous event, the primary driving factor for the August 3, 2021, mixed plumes was a ridge axis with its back edge along Washington, Oregon, and California on the first plume's starting day of August 1, 2021 (Figure 13a). However, unlike the previous event, this ridge remained mostly stationary and partly weakened over the three days. The first plume, starting in Rimrock, ID, was advected over Canada by southerly winds of approximately 5 m/s. On August 2, 2021, the first plume followed the clockwise flow around the ridge with westerly to northwesterly winds of approximately 5 to 10 m/s, while the second plume began its travel from

Flint Hills, KS (Figure 13b). Although the same northerly winds of approximately 5 to 10 m/s deposited the plumes over Billings, OK, they arrived at different heights (Figure 13c). While the Flint Hills, KS plume starting closer is likely a significant factor for the arrival location, a marginally stronger gradient in the geopotential heights over Kansas resulted in greater wind speeds on August 2, 2021.

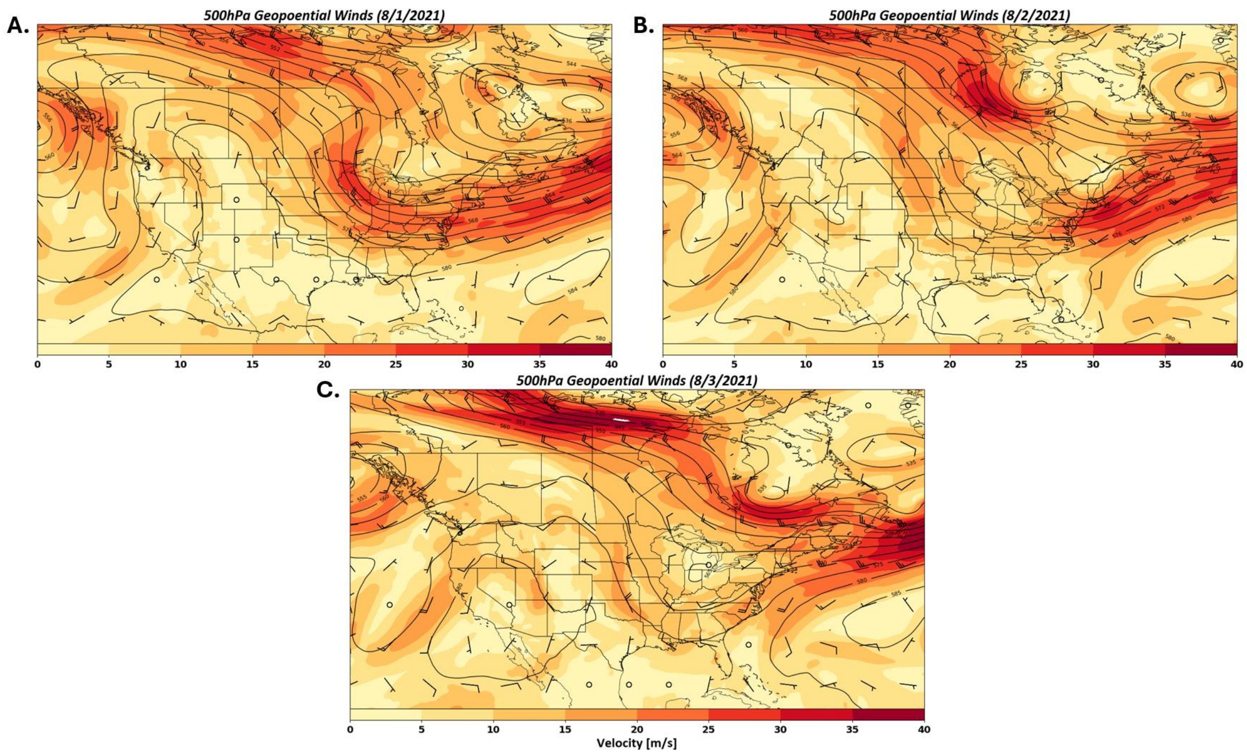

Figure 13 500 hPA height contours over the U.S. with shaded geopotential wind velocity (m/s) and wind barbs indicating wind direction for August 1, 2021 (a), August 2, 2021 (b), and August 3, 2021 (c).

5. Future Work

The future of this work is multi-faceted. A major limiting factor of the current methodology is the lack of high-quality data, particularly for AAE and SSA, as other variables further limit their derivation. While this research examined over a decade's worth of AERONET data, we only identified 27 cases of long-range transport to SGP. Although this is a substantial number of cases, many more were removed for quality assurance and to ensure observations were limited to smoke. This limitation could be addressed by expanding to other aerosol monitoring networks such as the Interagency Monitoring of Protected Visual Environments (IMPROVE) network or the Surface Particulate Matter Network (SPARTAN). However, ground-based networks will only ever allow for the comparison of optical properties at separate points.

A possible direction for this work would be to incorporate more satellite observations to not only fill in gaps of data at ground stations but also examine smoke properties along its entire path. While NASA MODIS is a likely candidate for this idea, the forthcoming aerosol products for NASA Plankton Aerosol Cloud, ocean Ecosystem (PACE) are especially promising for future work. The results of this work also suggest that while travel time plays a role in the evolution of optical properties, future expansions of this work should incorporate a focus on variations due to fuel type and influence by meteorological conditions. An especially interesting continuation would be to examine specific aerosol paths and the underlying meteorology to identify any connection with the evolution of aerosol properties. This would also allow for determining which conditions influence whether plumes will enter the boundary layer to more directly influence human health. In addition, this work can be expanded by following the smoke plumes further in the SGP using ground stations from AERONET, EPA, and NASA MPLNET.

6. Summary

This research examined the effects of long-range transport from the western U.S. to the Southern Great Plains (SGP) on smoke aerosol optical properties. We sought to answer how wildfire smoke aerosol optical depth (AOD), single scattering albedo (SSA), Absorption Ångström exponent (AAE), and extinction Ångström exponent (EAE) evolve during transport to the SGP and what are the dependencies on travel time.

Twenty-seven cloud-free smoke events were identified to have undergone long-range transport and arrived at Billings, OK, between 2015 and 2022. These cases were identified through a combination of seasonally averaged MODIS Deep Blue (DB) AOD maps, comparison of AERONET ground stations retrievals, and HYSPLIT back trajectories parameterized by micropulse lidar (MPL) determined plume height over Billings, OK. After determining the closest AERONET station to each smoke event's source, we compared source station aerosol optical properties to Billings, OK observations lagged by the travel time of the smoke plume. ERA5 reanalysis and ground-based nephelometer observations at Billings, OK, examined meteorological influences and reinforced plume arrival height. With the above in mind, we found:

- Seasonal maps of DB AOD established the temporal domain for identifying smoke events between June and September from 2015 to 2022. AOD was elevated to approximately 0.2 to 0.3 between the western U.S. and SGP, likely indicating the wildfire season. August and September also saw peak AOD (>0.4) across Washington, Oregon, and California.
- A comparison of AERONET AOD retrievals across ten sites during August and September from 2015 to 2022 indicated evidence of long-range transport across sites during September 2017, September 2020, and August 2021. Here, mean AOD at Missoula, MT (~0.69), Fresno, CA (~0.96), and Reno, NV (~0.94) corresponded with elevated mean AOD in Billings, OK (~0.31, ~0.57, and ~0.3).
- The twenty-seven smoke events were validated to have arrived over Billings, OK, with MPL and AERONET measurements of AOD and EAE. Back trajectory analysis was conducted for each event, with starting height determined by MPL estimating plume height to determine source and travel time.

- When comparing AERONET observations of AOD and EAE, there was a decrease in both properties between their plume source and Billings, OK. Particle size and optical loading seem to decrease with travel time until nearly four-day events, as these were all observed to mix with other plumes during travel. Mean AOD decreased by ~0.21, ~0.38, ~1.69, ~1.42, and ~0.1 while mean EAE decreased by ~0.13, ~0.2, ~0.25, ~0.18, and ~0.2 for zero through four-day travel time, respectively. With a longest travel time of four days, this work is unlikely to observe large changes in the organic coating that accumulates on black carbon aerosol.
- While SSA decreases between source and Billings, OK, AAE increases with travel. This indicates that after long-range transport, smoke aerosols become more light-absorbing and closer to brown carbon. Mean SSA decreased by ~0.02, ~0.02, <0.01, ~0.02, and ~0.01, while mean AAE increased by ~1.26, ~0.16, ~0.04, ~0.34, and ~0.32, respective to travel time. However, it is important to note that the relatively small number of points for these variables limits the statistical significance of these values.
- Several of the smoke events observed arrived in Billings, OK, within the boundary layer ($\lesssim$2 km from the surface). While lower arrival height may be associated with shorter travel times, the underlying meteorology (troughs and ridges) driving wind direction and intensity seem to be the primary determinant of plume path and arrival.
- Some limiting factors of this work were limited data points, especially for the derived values of AAE and SSA. Also, while this work primarily focused on sources from a similar region (western U.S.), more should likely be done to account for variations due to fuel type.

- A significant focus for future work should be on the evolution of optical properties influenced by specific meteorological events and travel paths. The scope of this work would likely need to expand beyond relying on ground stations and approach more remote sensing options such as the NASA Plankton Aerosol Clouds Ecosystem (PACE) mission.

Appendix

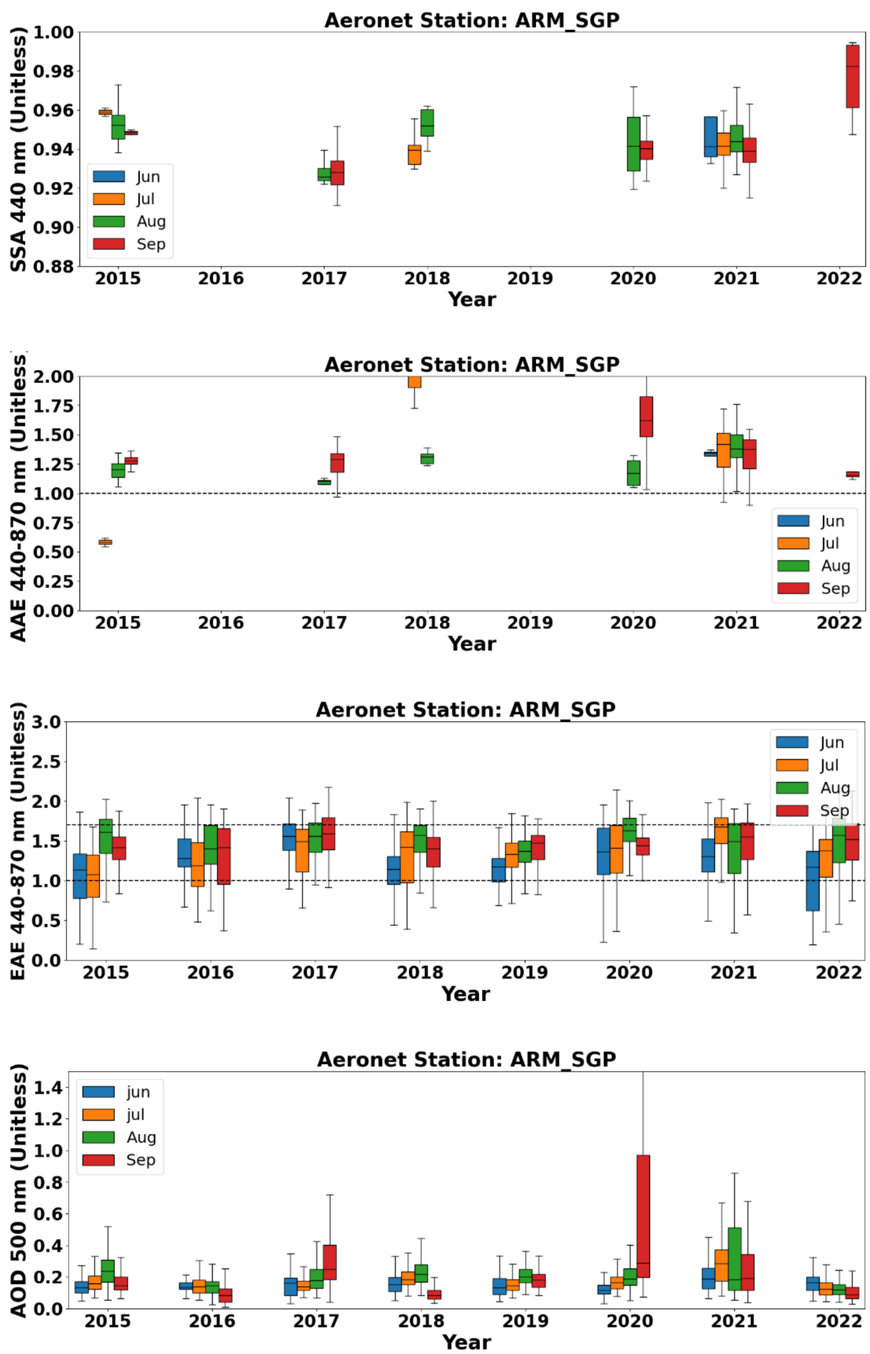

Appendix A 1 Monthly box and whisker plots for June, July, August, and September from 2015 to 2022 of $SSA_{440\,nm}$, $AAE_{440-870\,nm}$, $EAE_{440-870\,nm}$, *and* $AOD_{500\,nm}$ *for Billings, OK.*

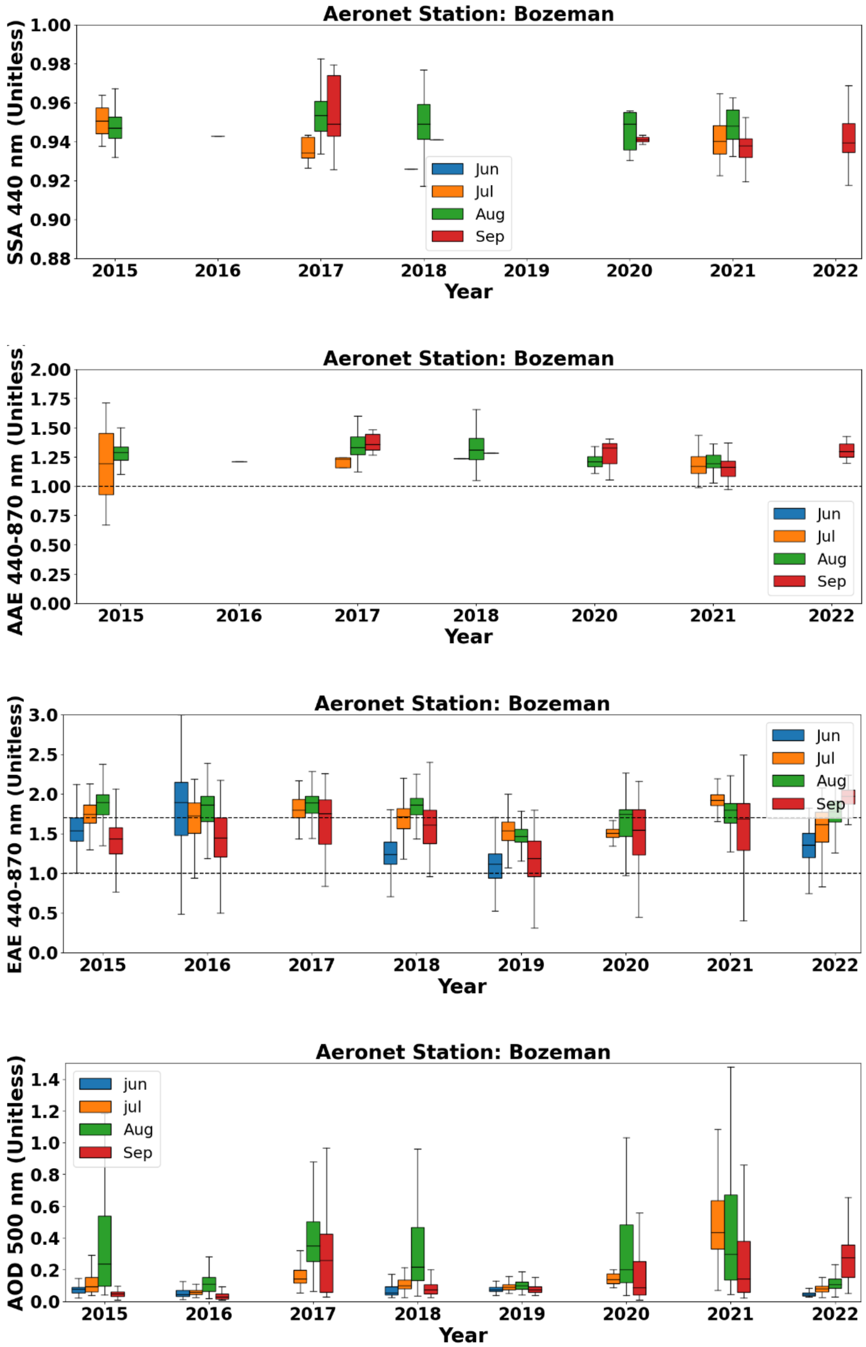

Appendix A 2 Same as A.1 for Bozeman, MT.

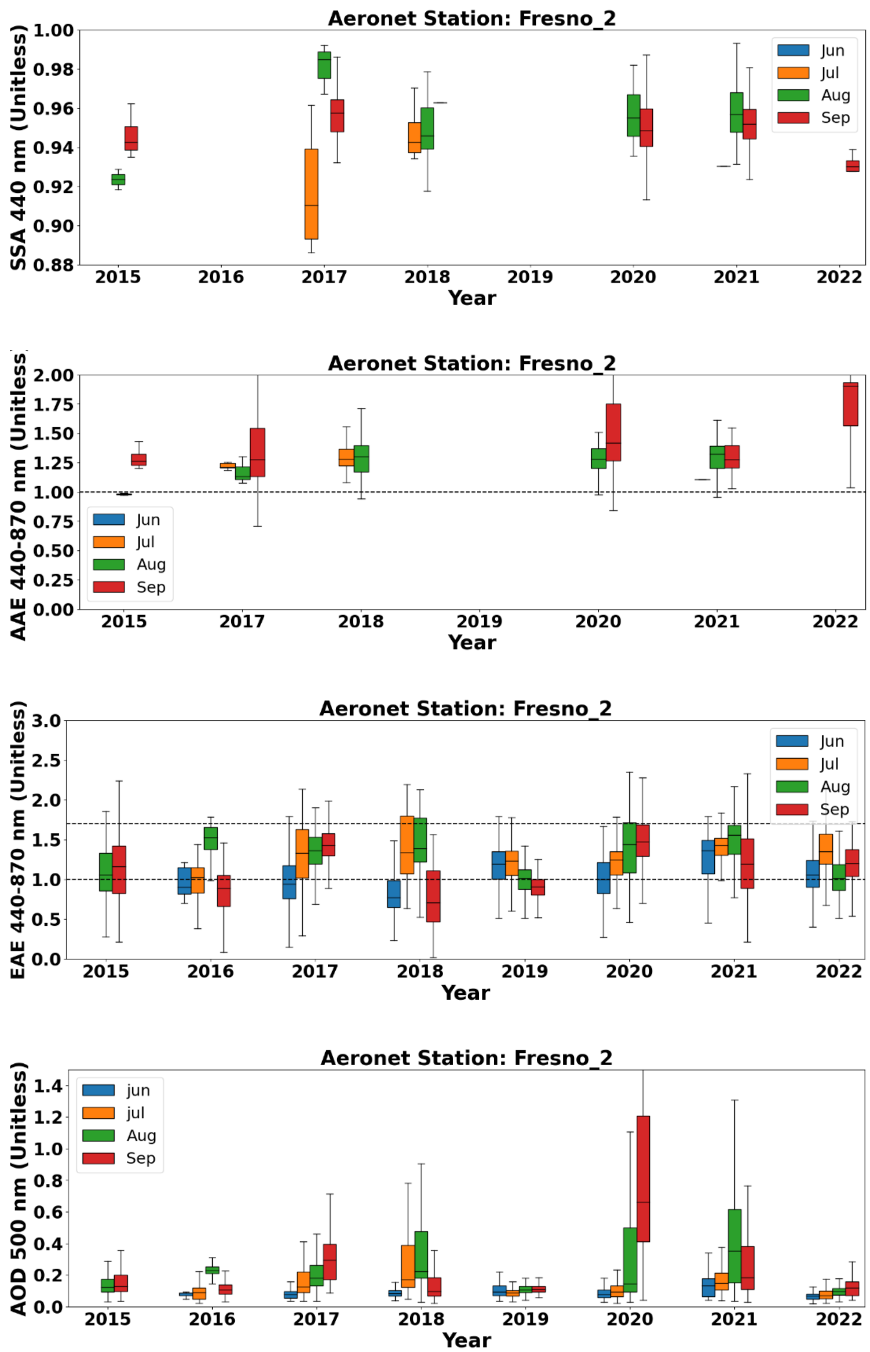

Appendix A 3 Same as A.1 for Fresno, CA.

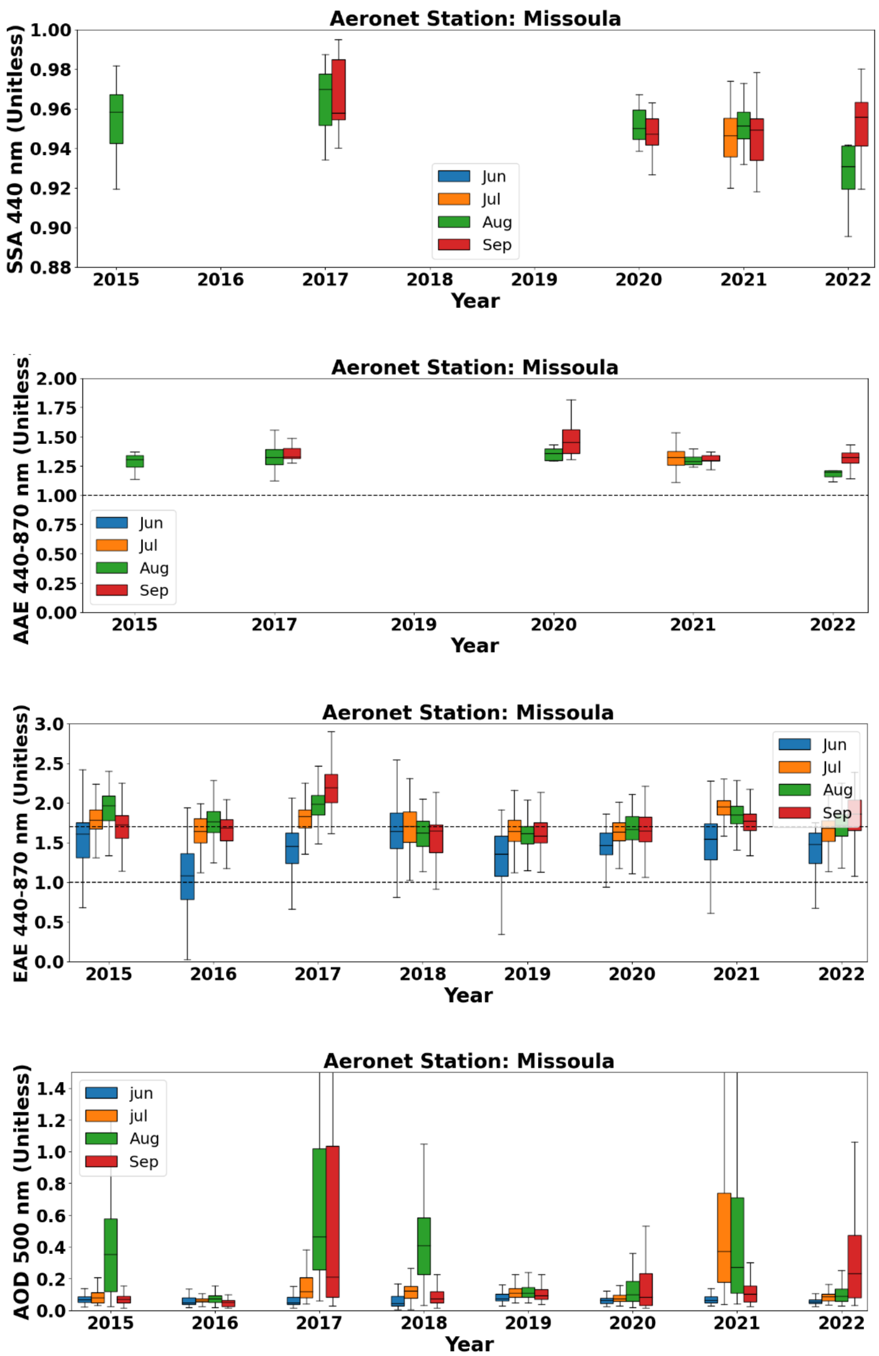

Appendix A 4 Same as A.1 for Missoula, MT.

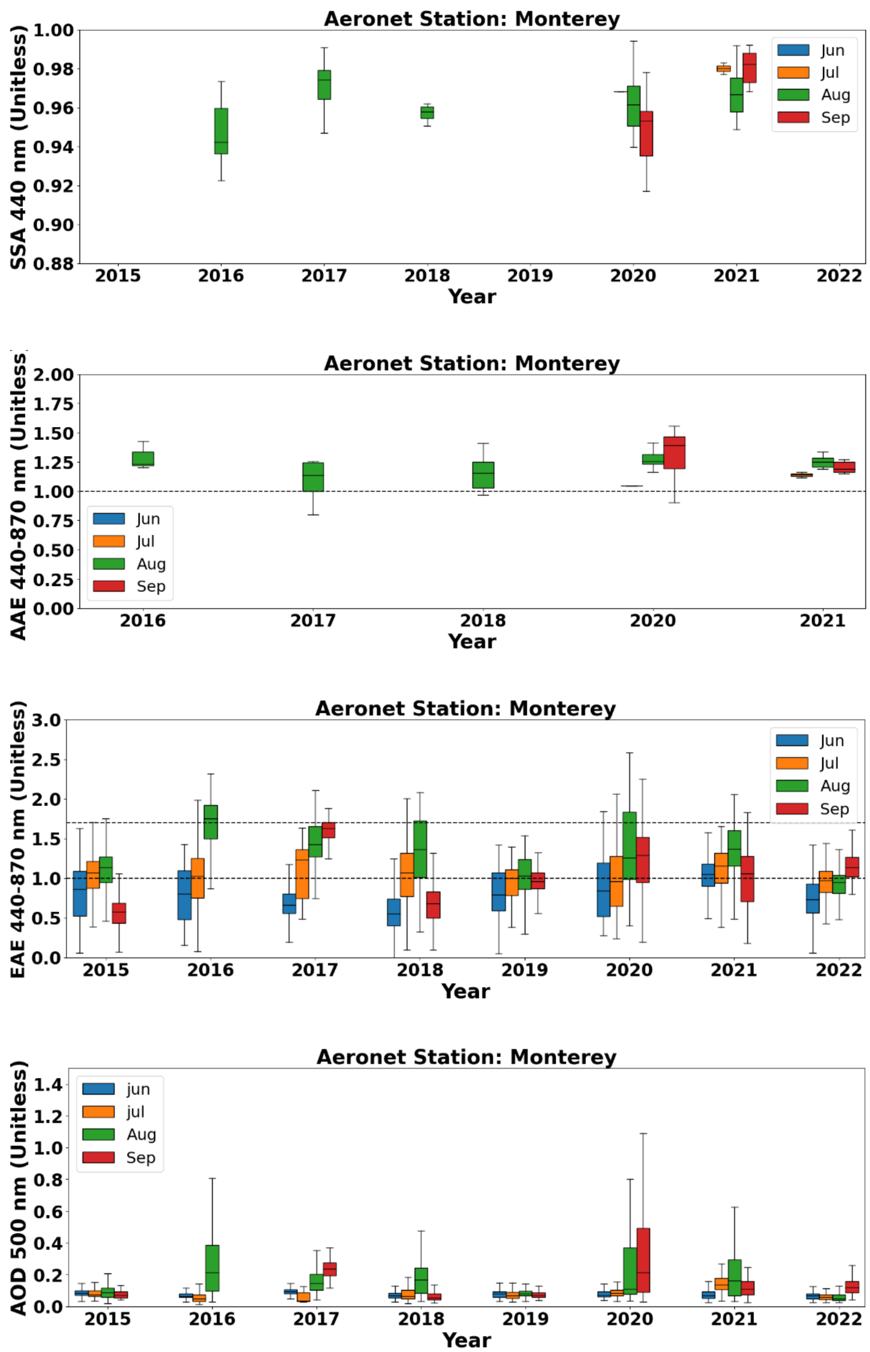

Appendix A 5 Same as A.1 for Monterey, CA.

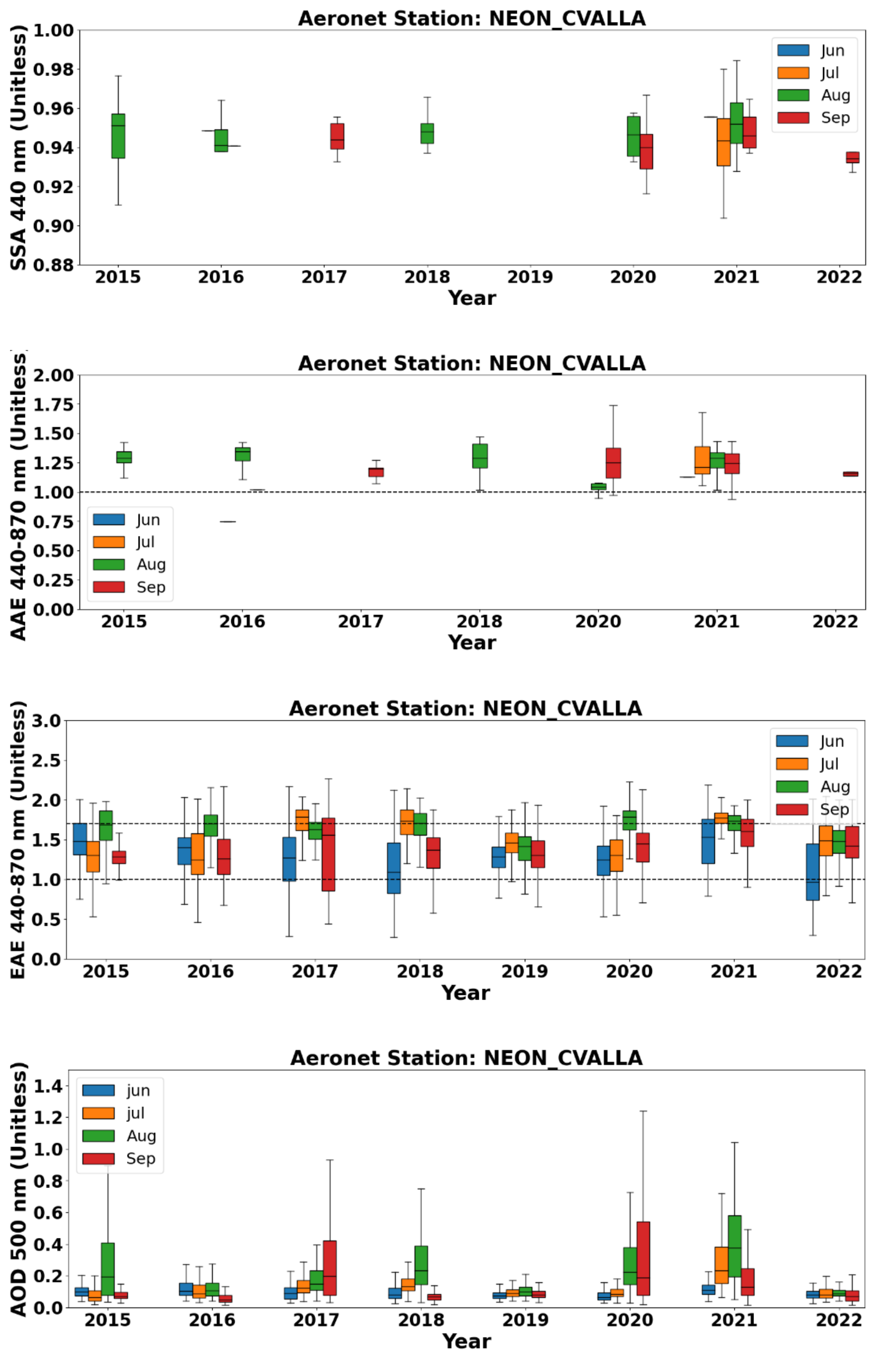

Appendix A 6 Same as A.1 for Longmont, CO.

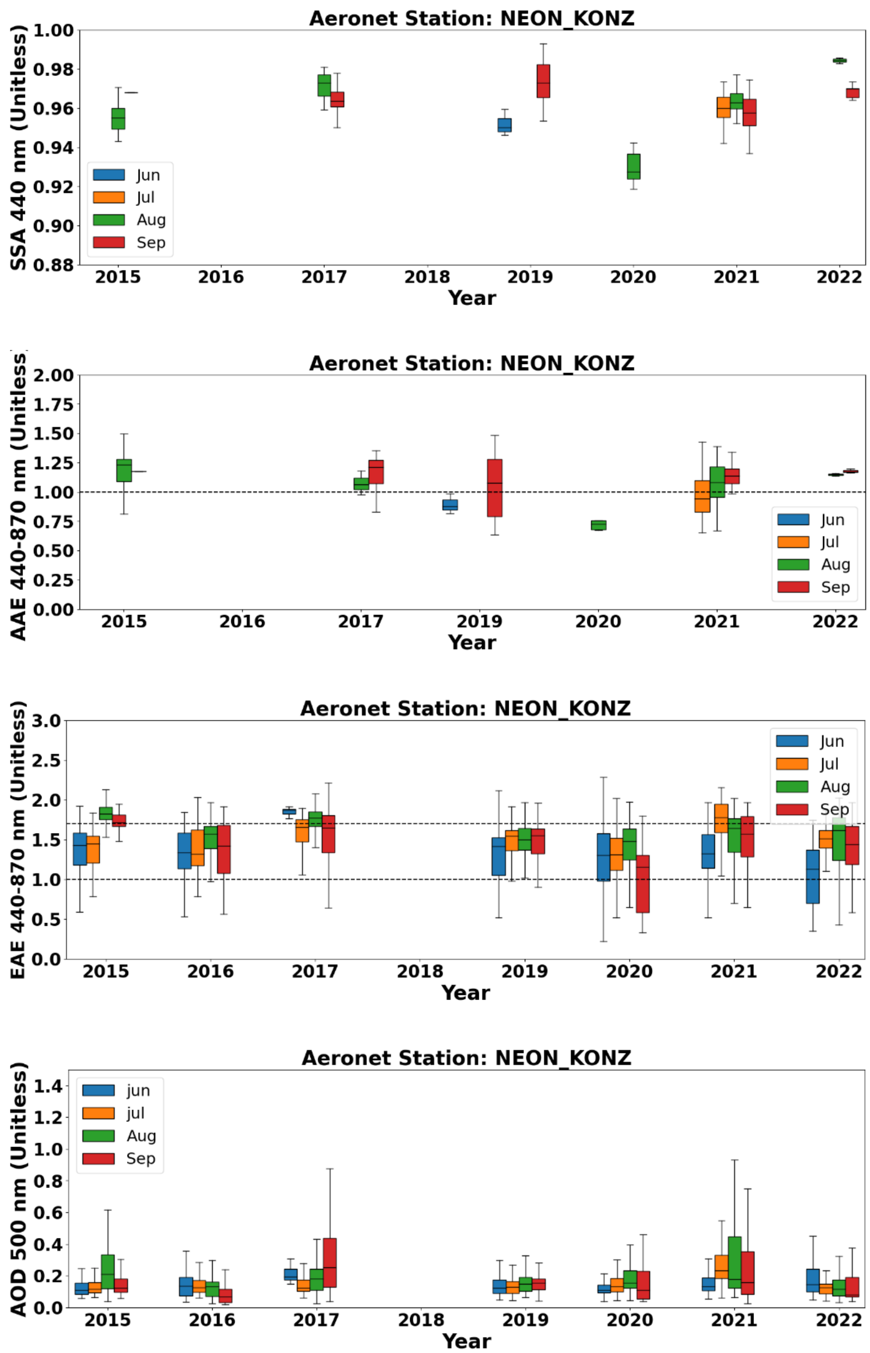

Appendix A 7 Same as A.1 for Flint Hills, KS.

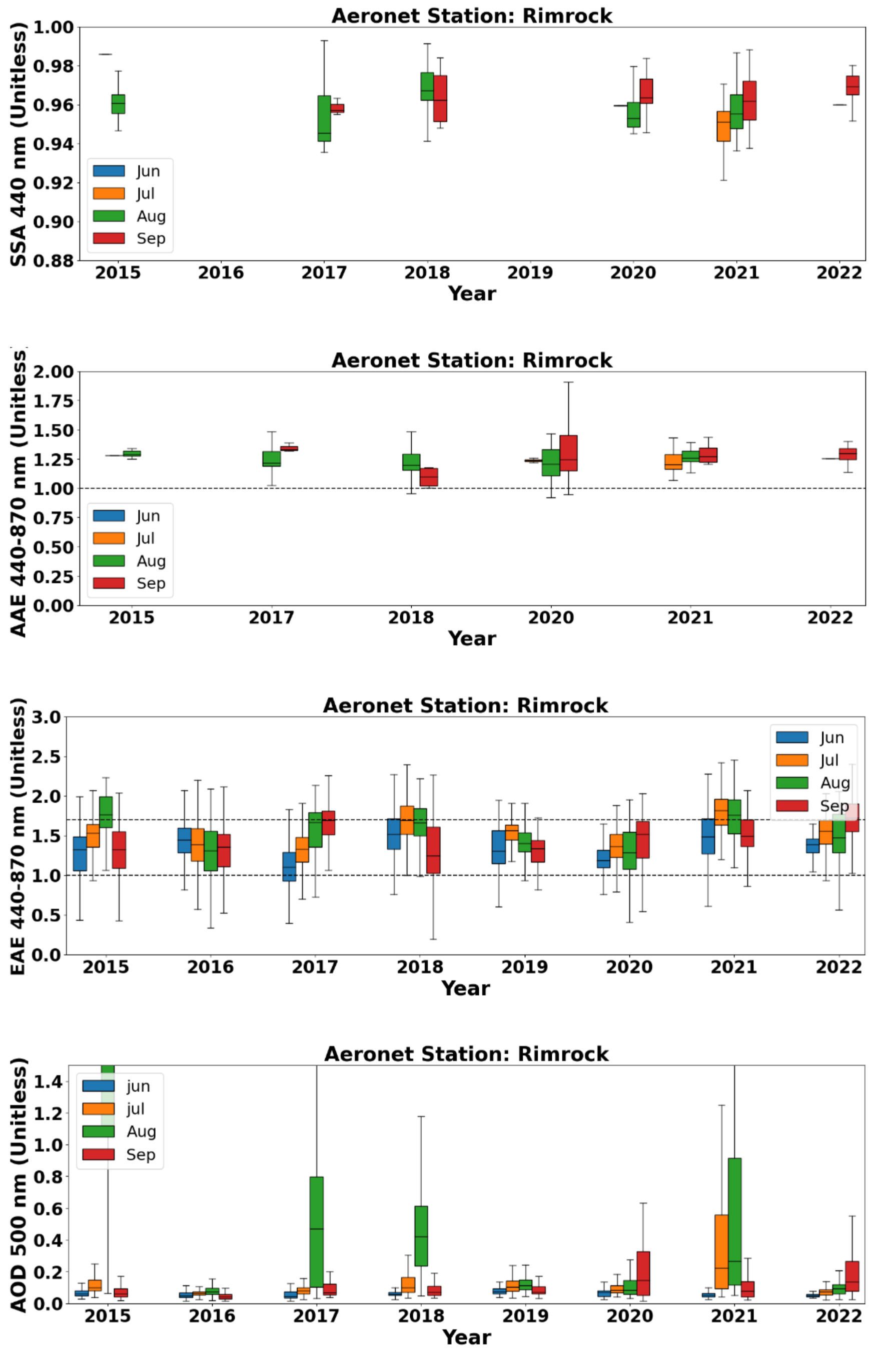

Appendix A 8 Same as A.1 for Rimrock, ID.

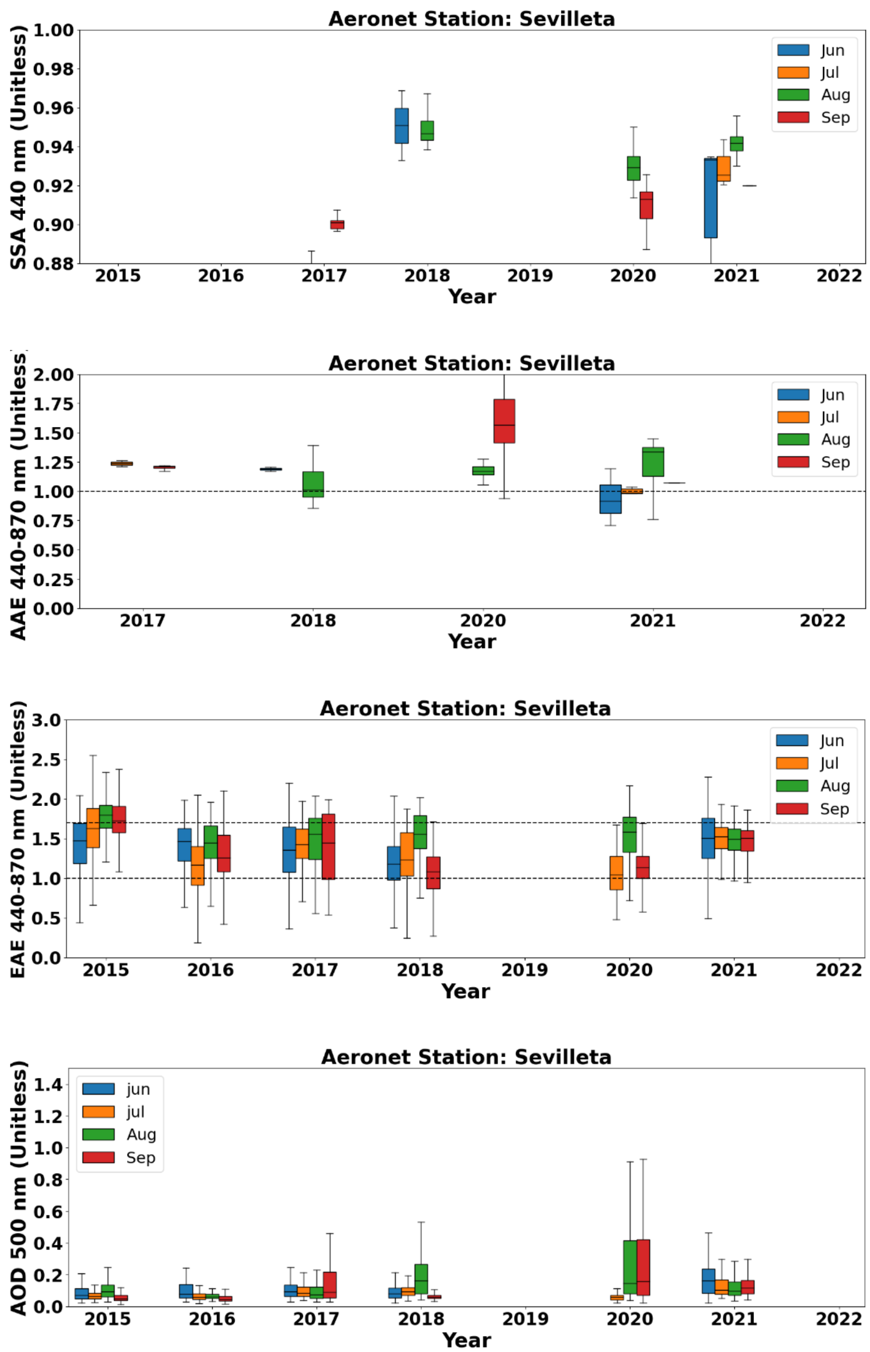

Appendix A 9 Same as A.1 for Sevilleta, NM.

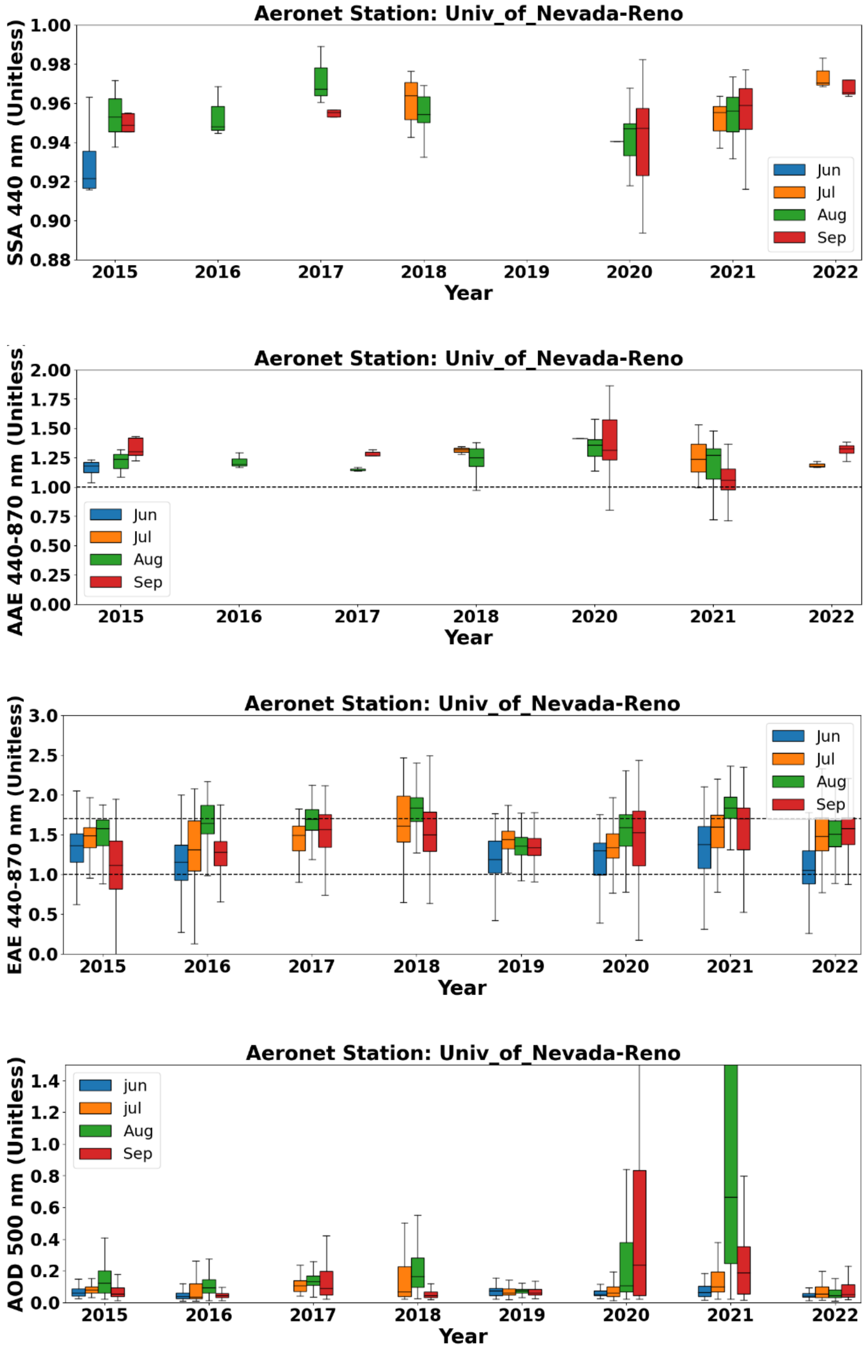

Appendix A 10 Same as A.1 for Reno, NV.

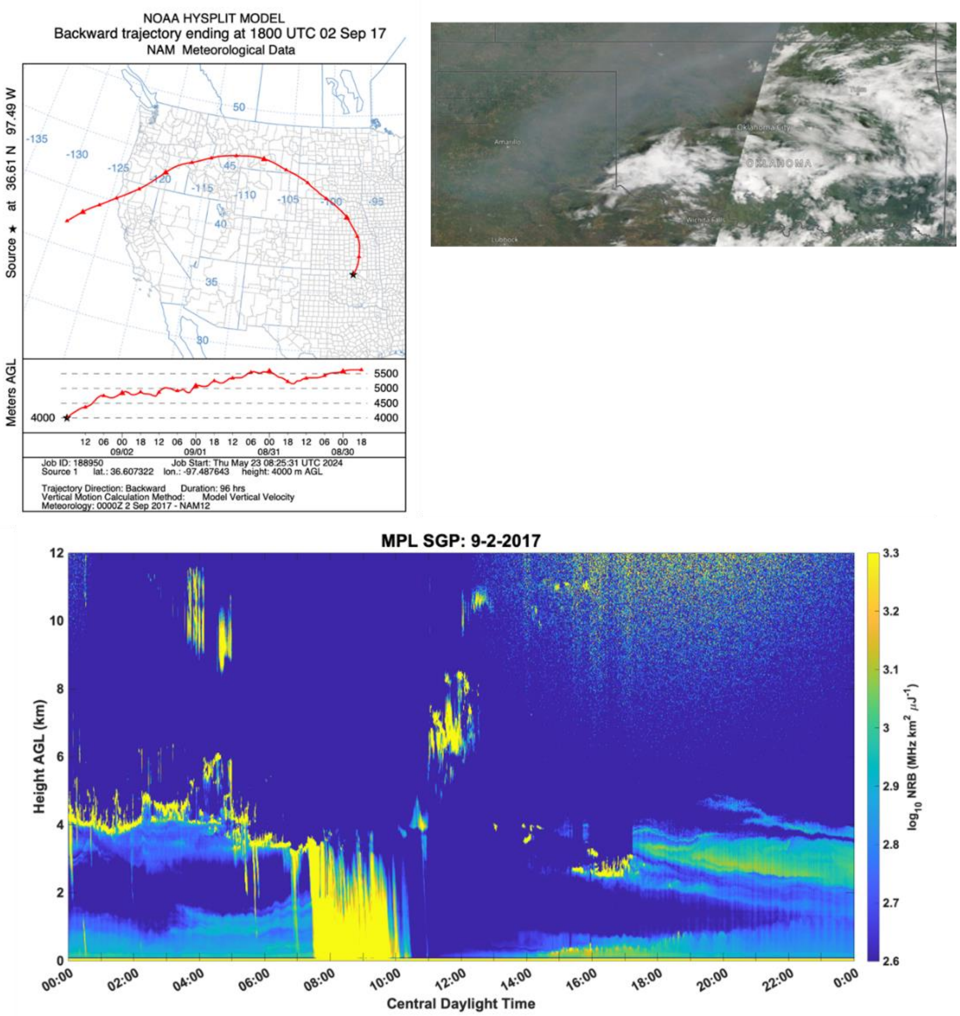

Appendix B 1 Smoke event data set for September 2, 2017, including HYSPLIT back trajectory over Billings, OK, Terra true color image of smoke, and MPL normal relative backscattering retrieval.

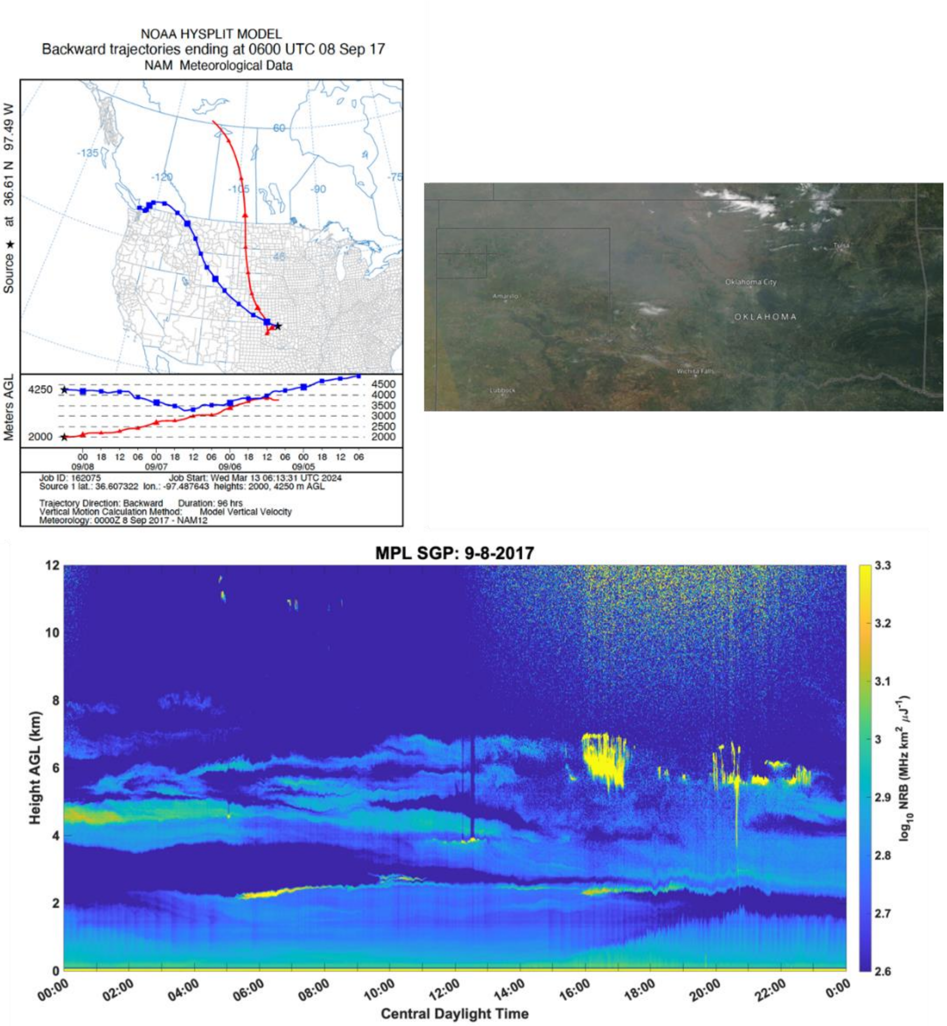

Appendix B 2 Same as B.1 for September 8, 2017.

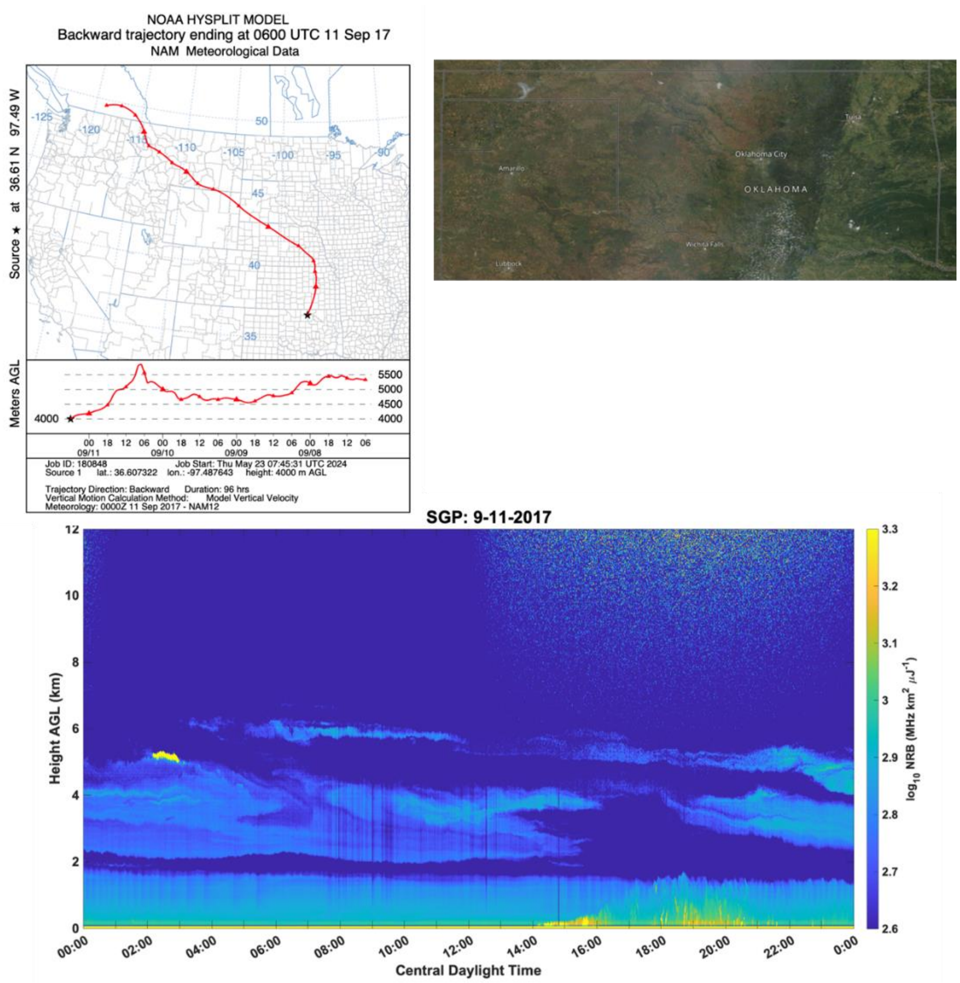

Appendix B 3 Same as B.1 for September 11, 2017.

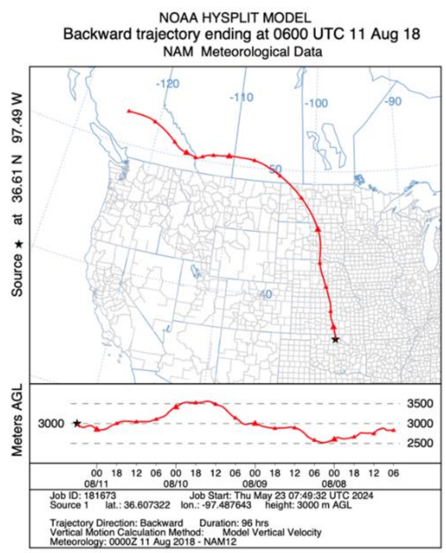

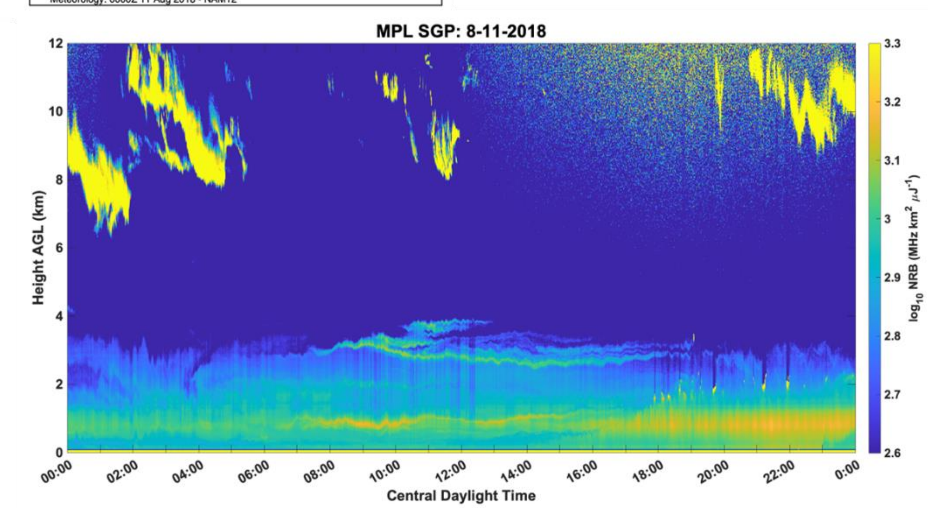

Appendix B 4 Same as B.1 for August 11, 2018.

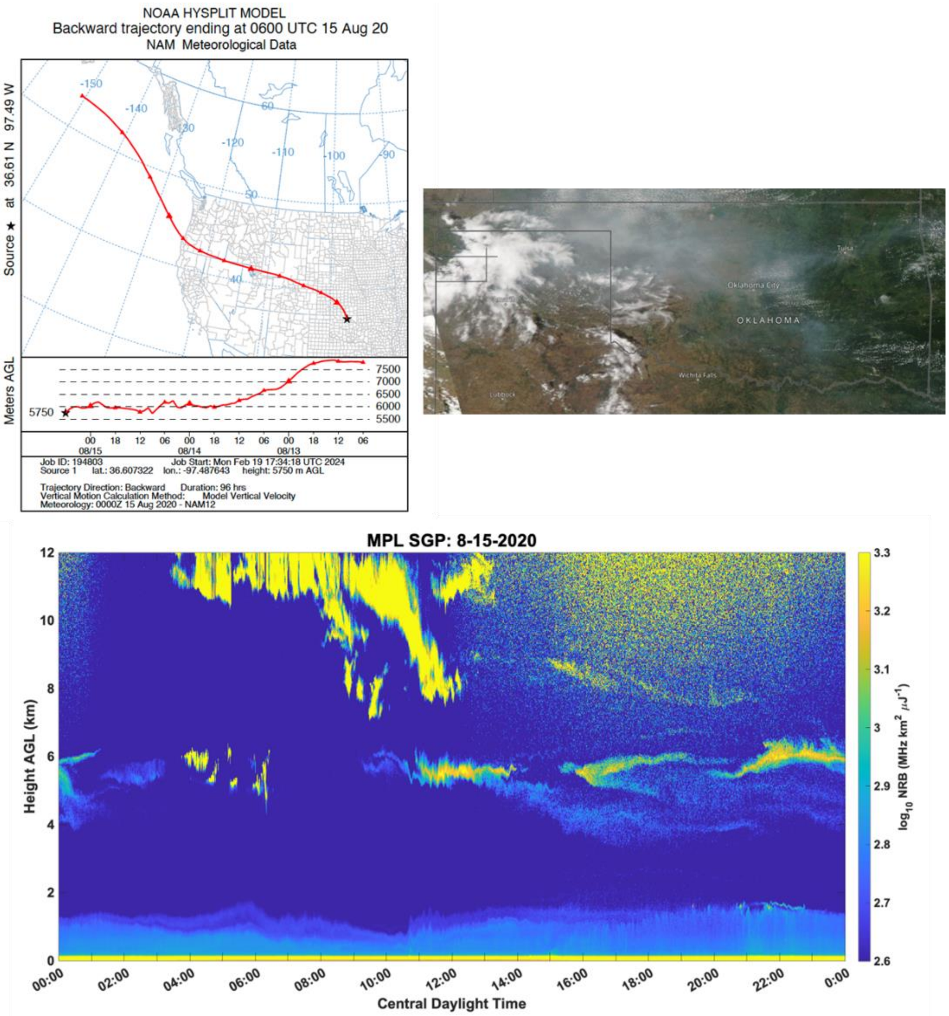

Appendix B 5 Same as B.1 for August 15, 2020.

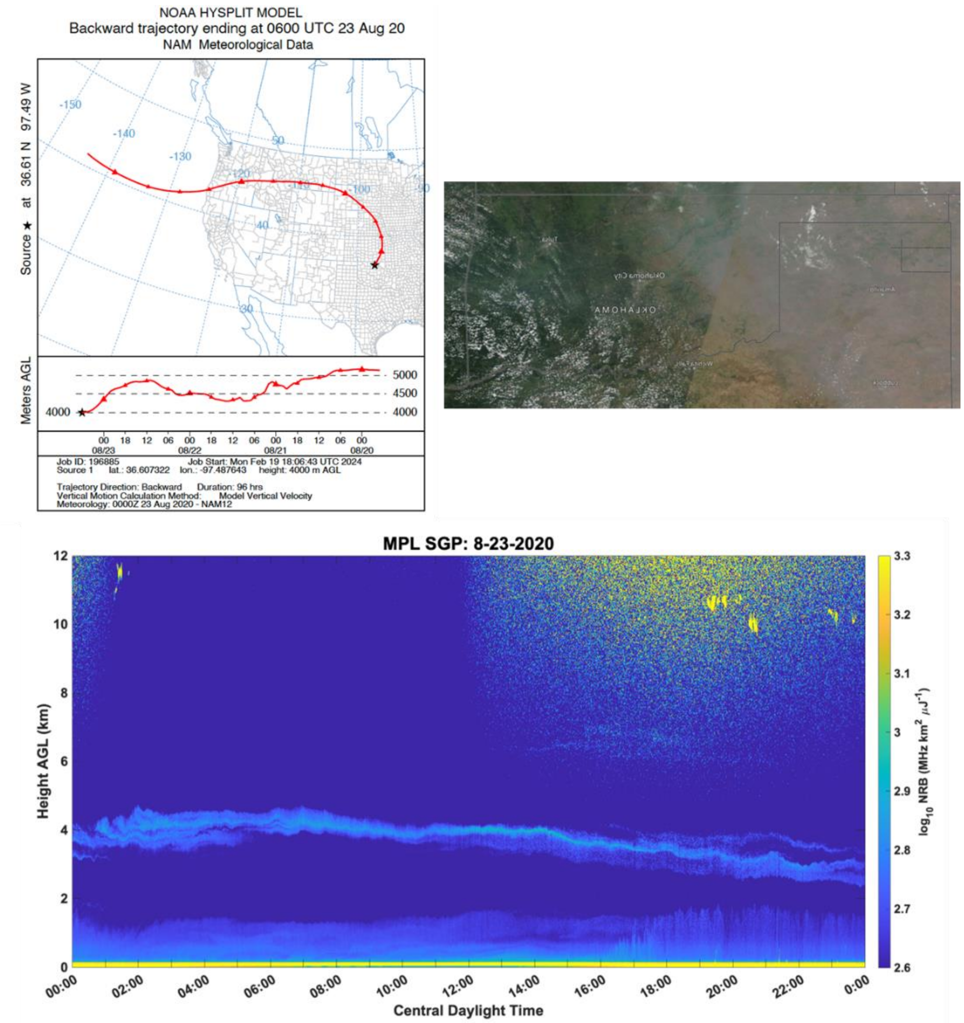

Appendix B 6 Same as B.1 for August 23, 2020.

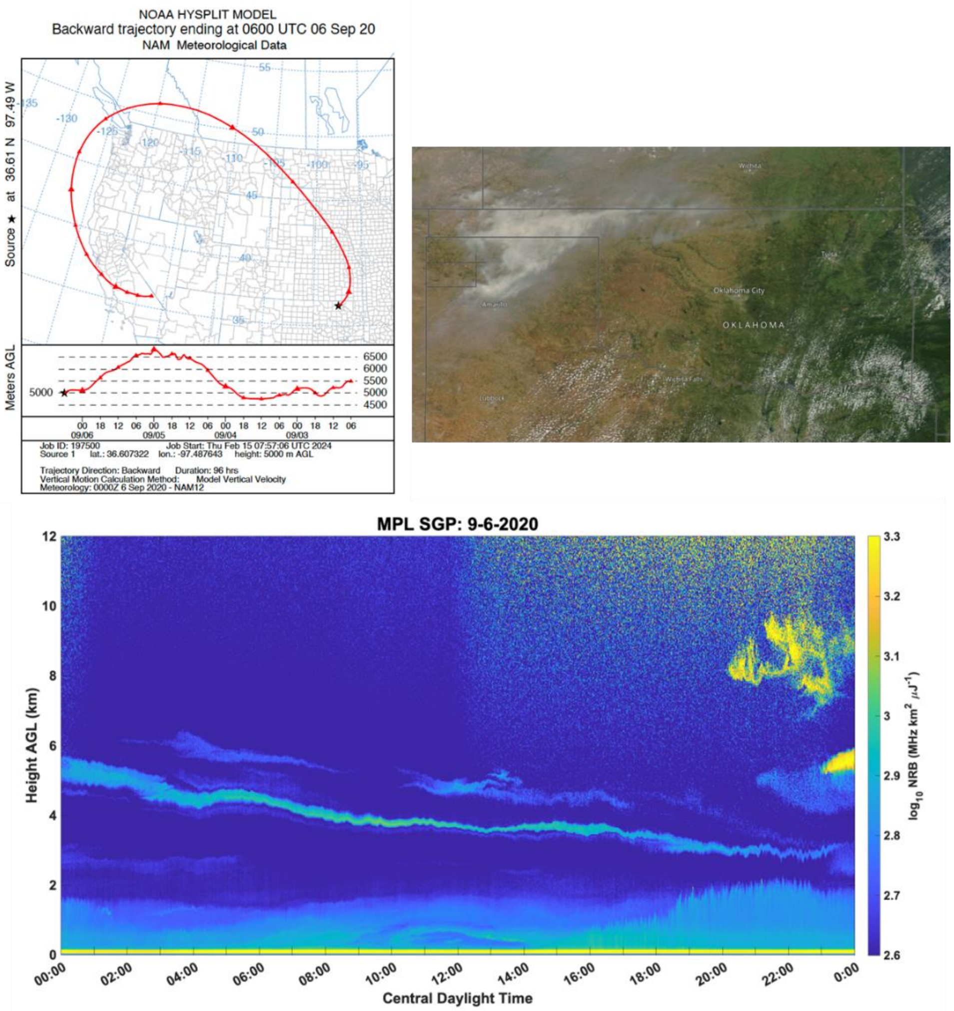

Appendix B 7 Same as B.1 for September 6, 2020.

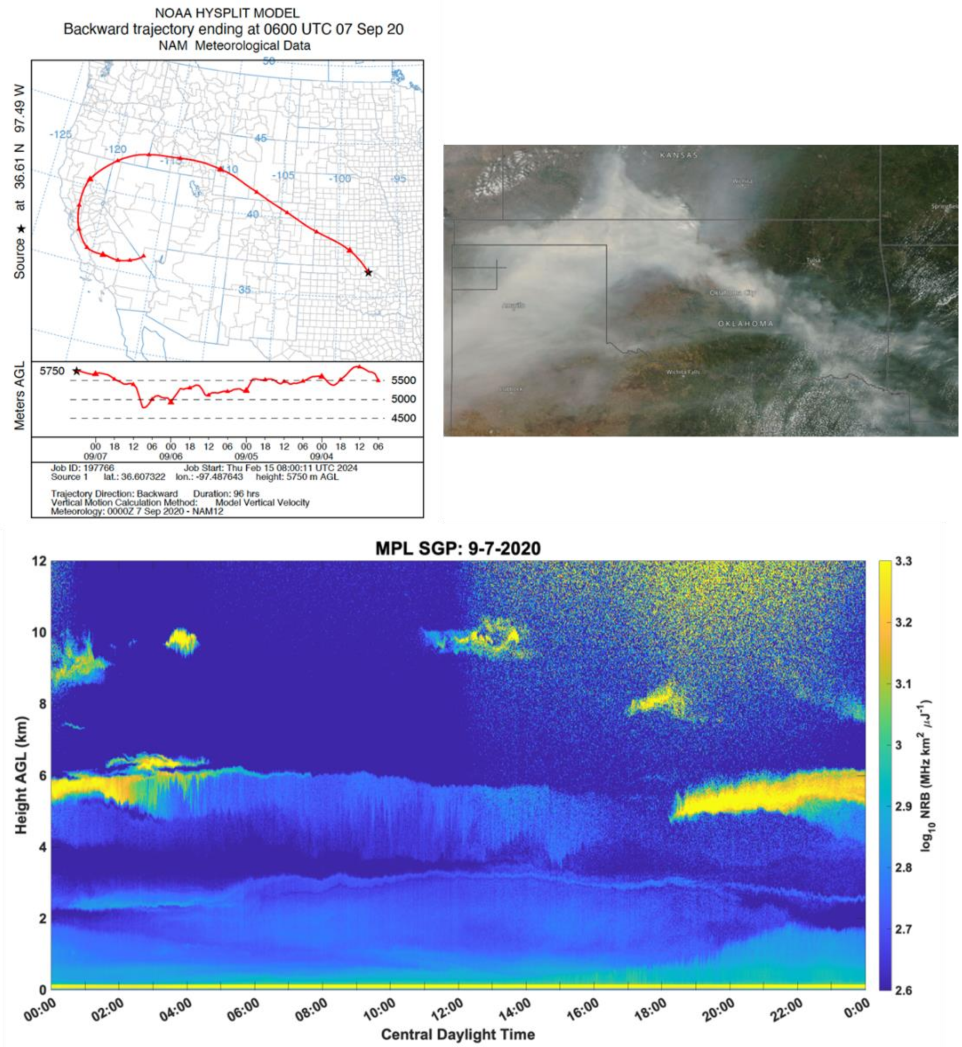

Appendix B 8 Same as B.1 for September 7, 2020.

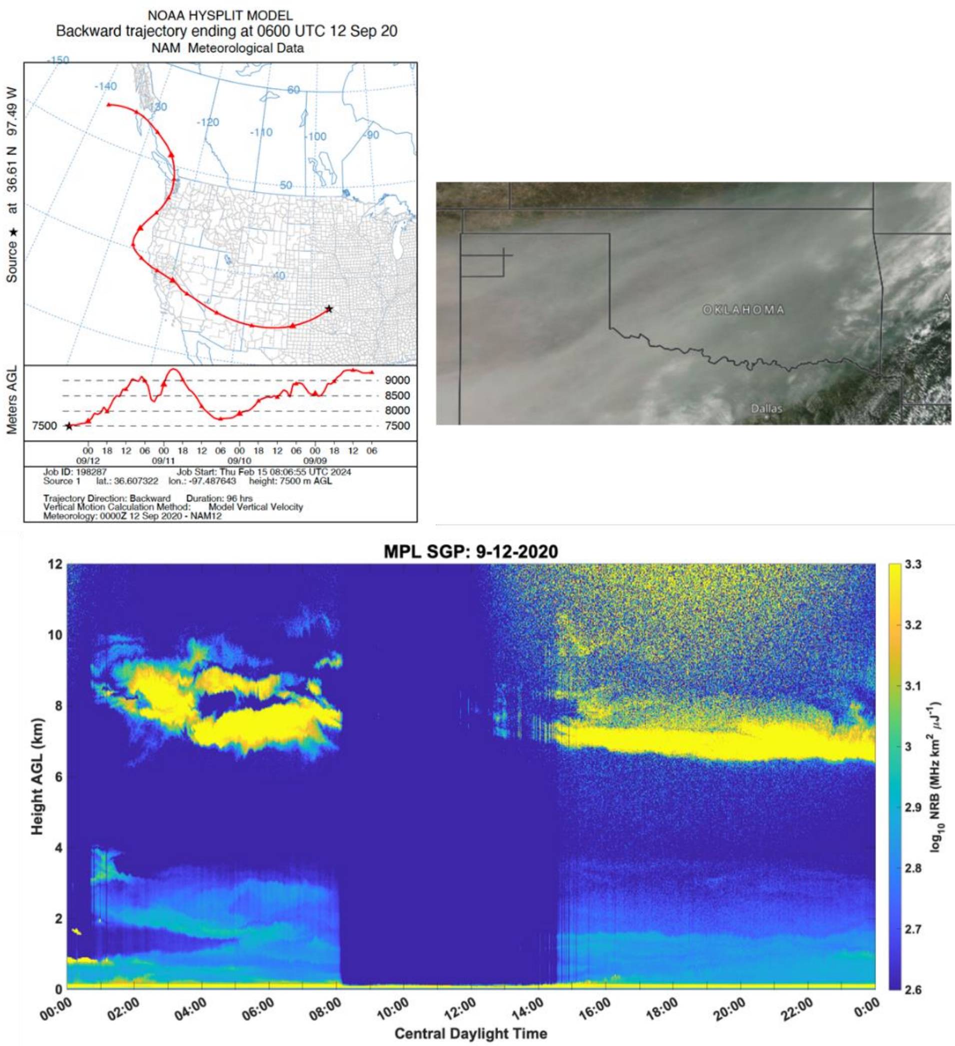

Appendix B 9 Same as B.1 for September 12, 2020.

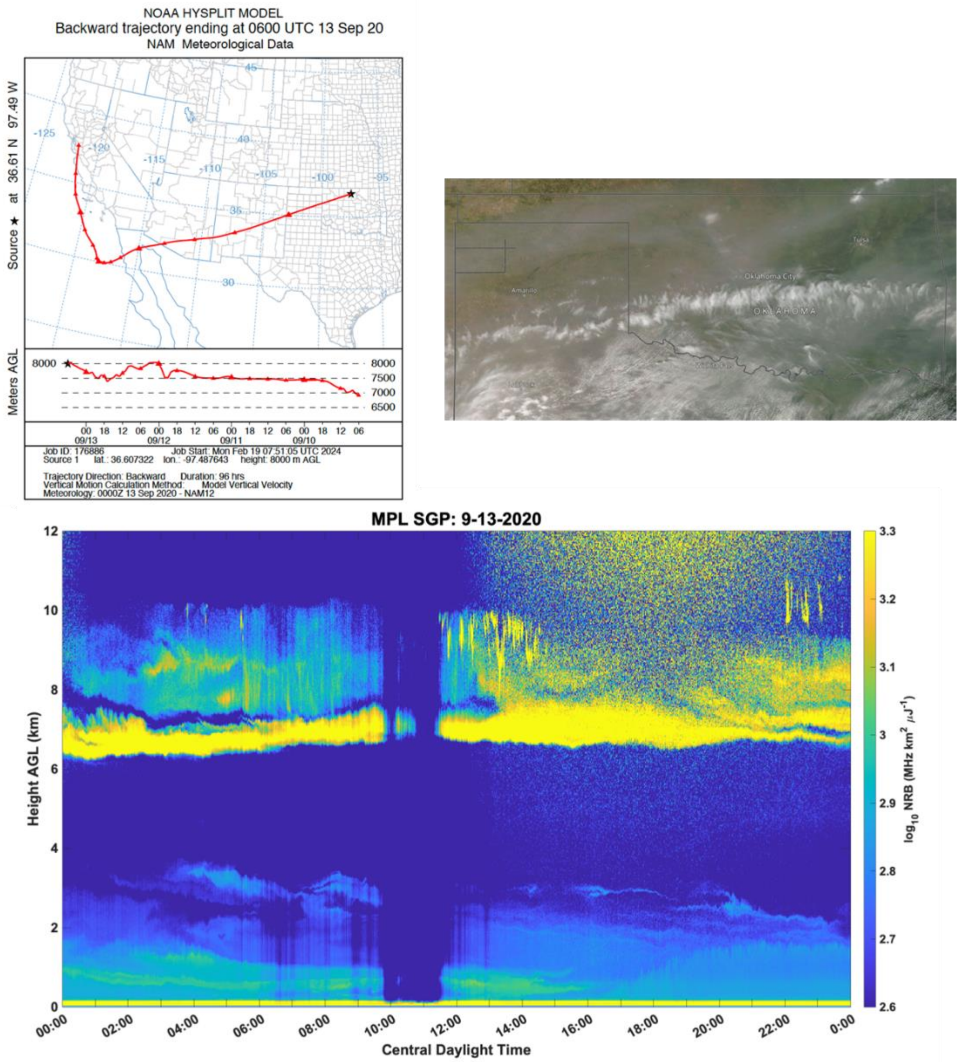

Appendix B 10 Same as B.1 for September 13, 2020.

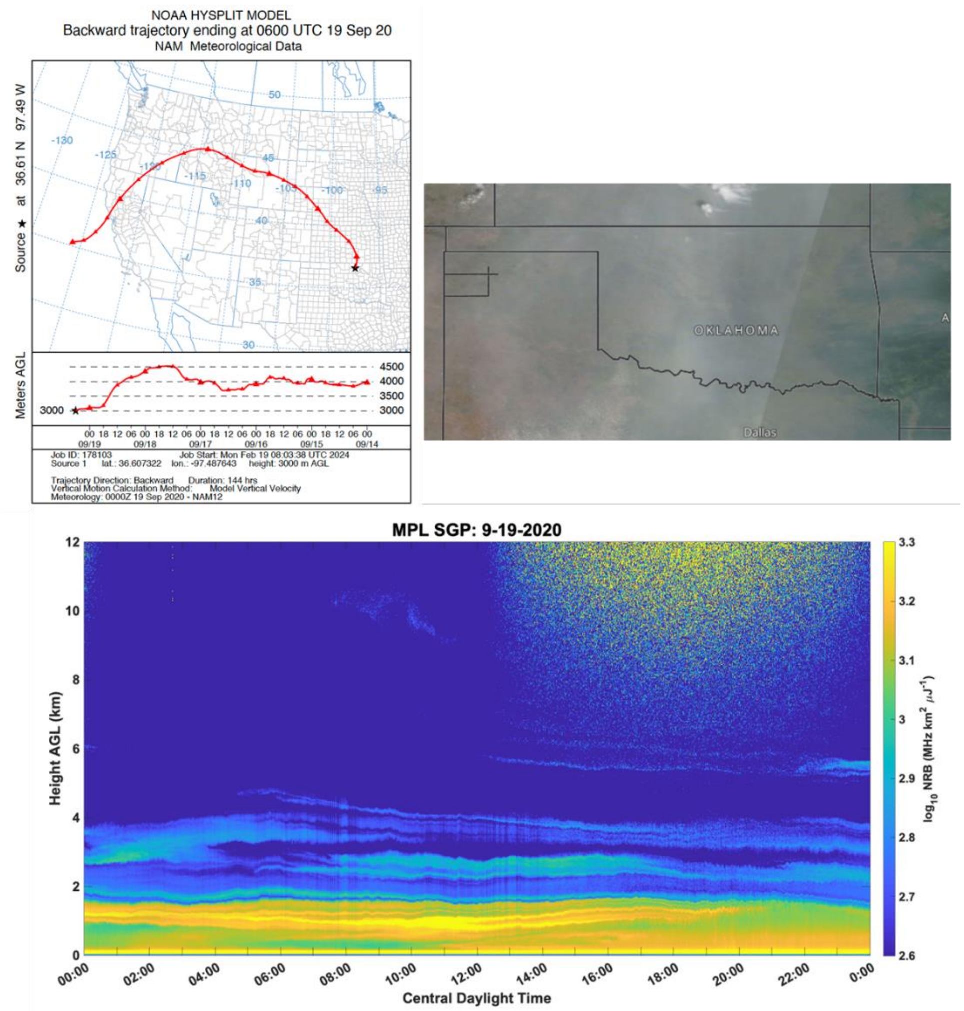

Appendix B 11 Same as B.1 for September 19, 2020.

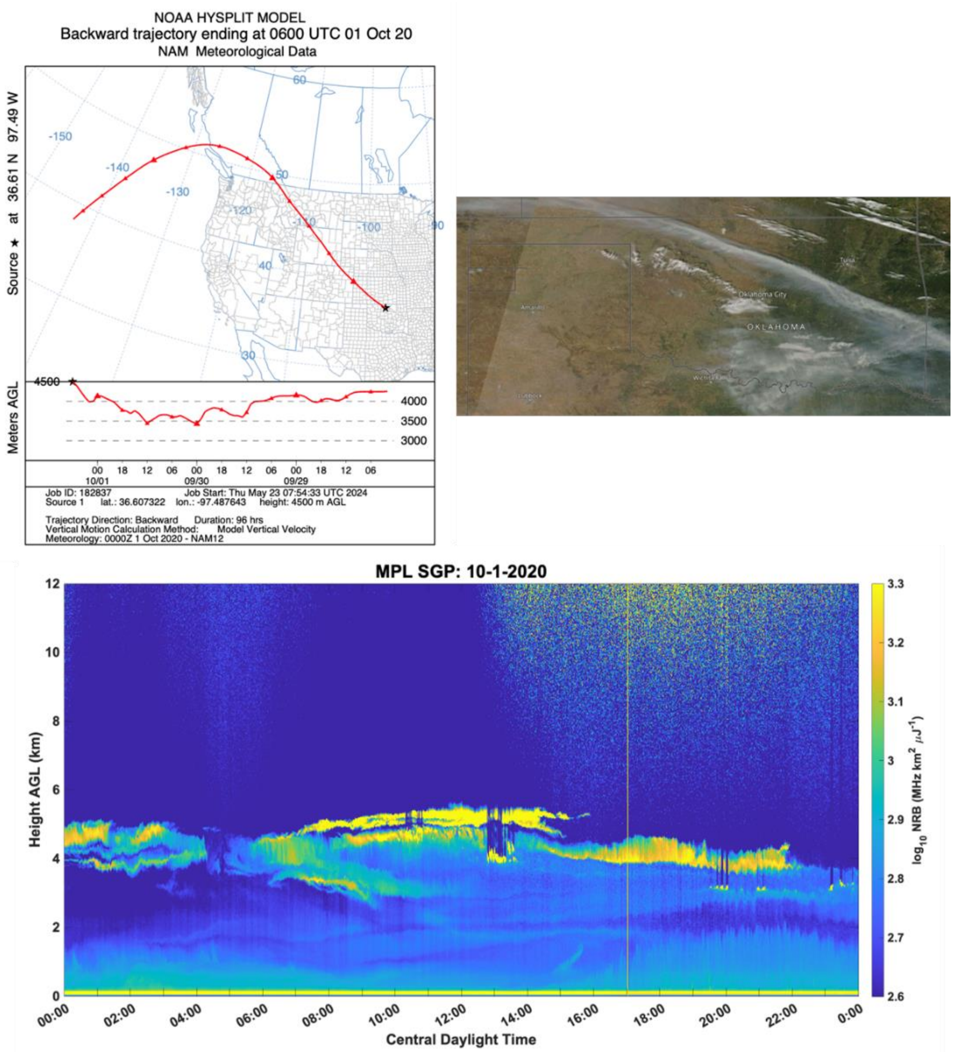

Appendix B 12 Same as B.1 for October 1, 2020.

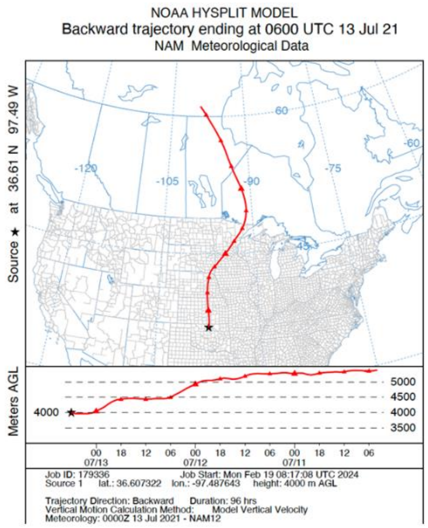

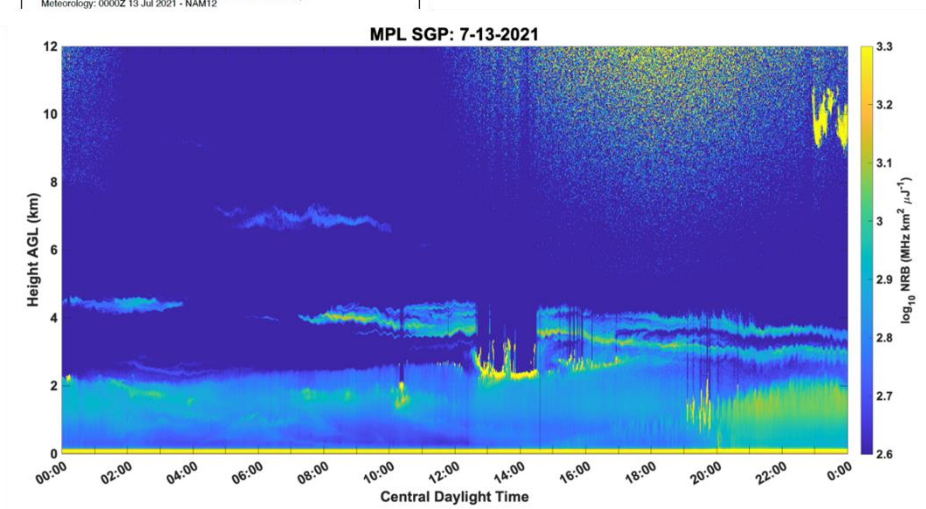

Appendix B 13 Same as B.1 for July 13, 2021.

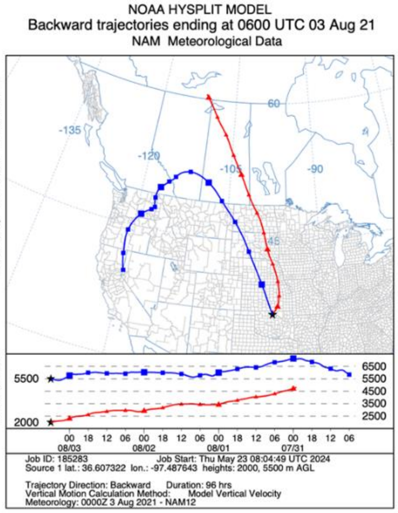

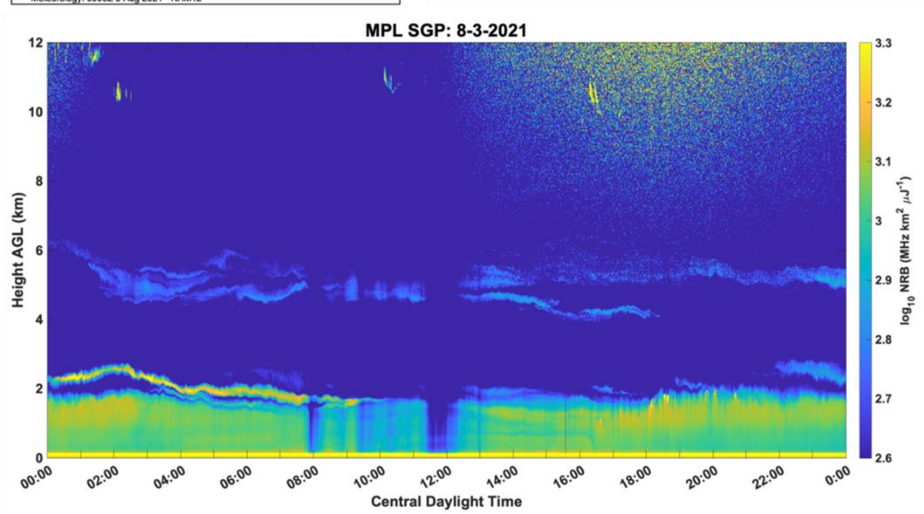

Appendix B 14 Same as B.1 for August 3, 2021.

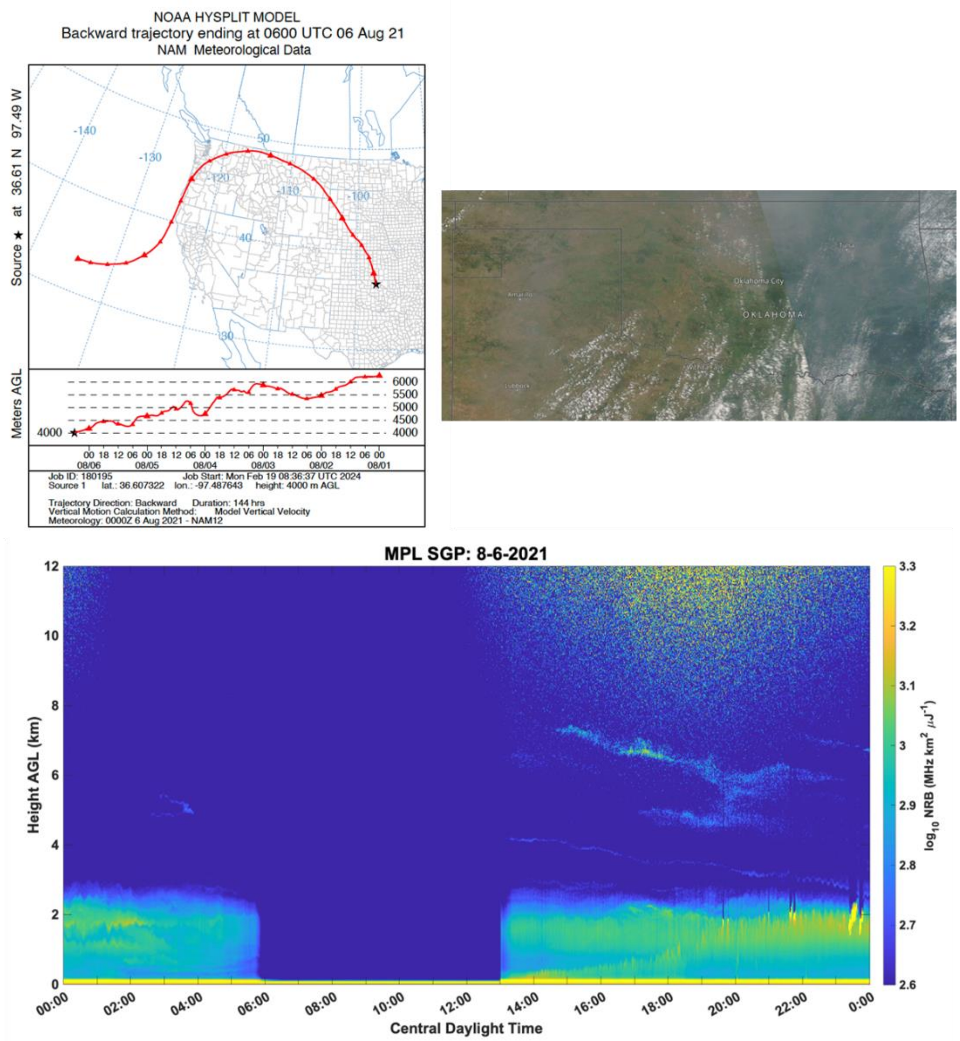

Appendix B 15 Same as B.1 for August 6, 2021.

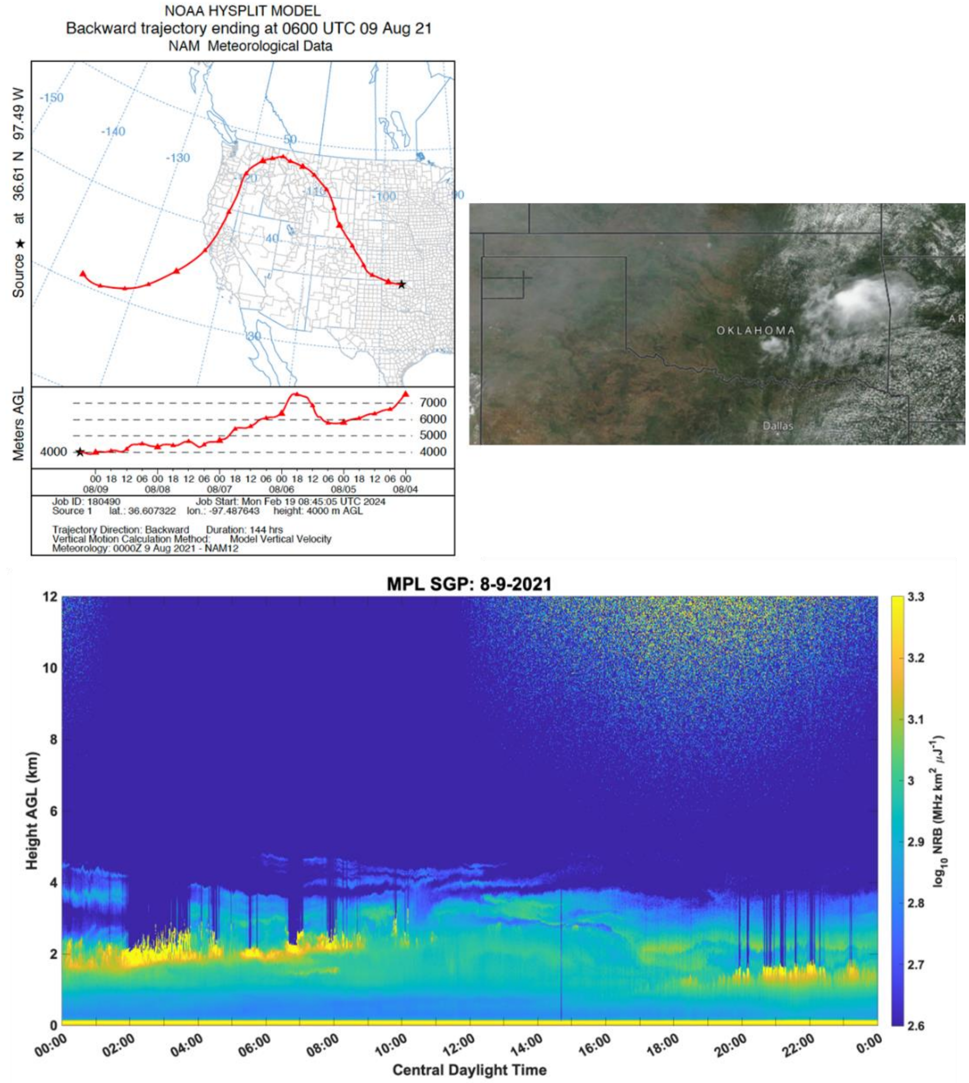

Appendix B 16 Same as B.1 for August 9, 2021.

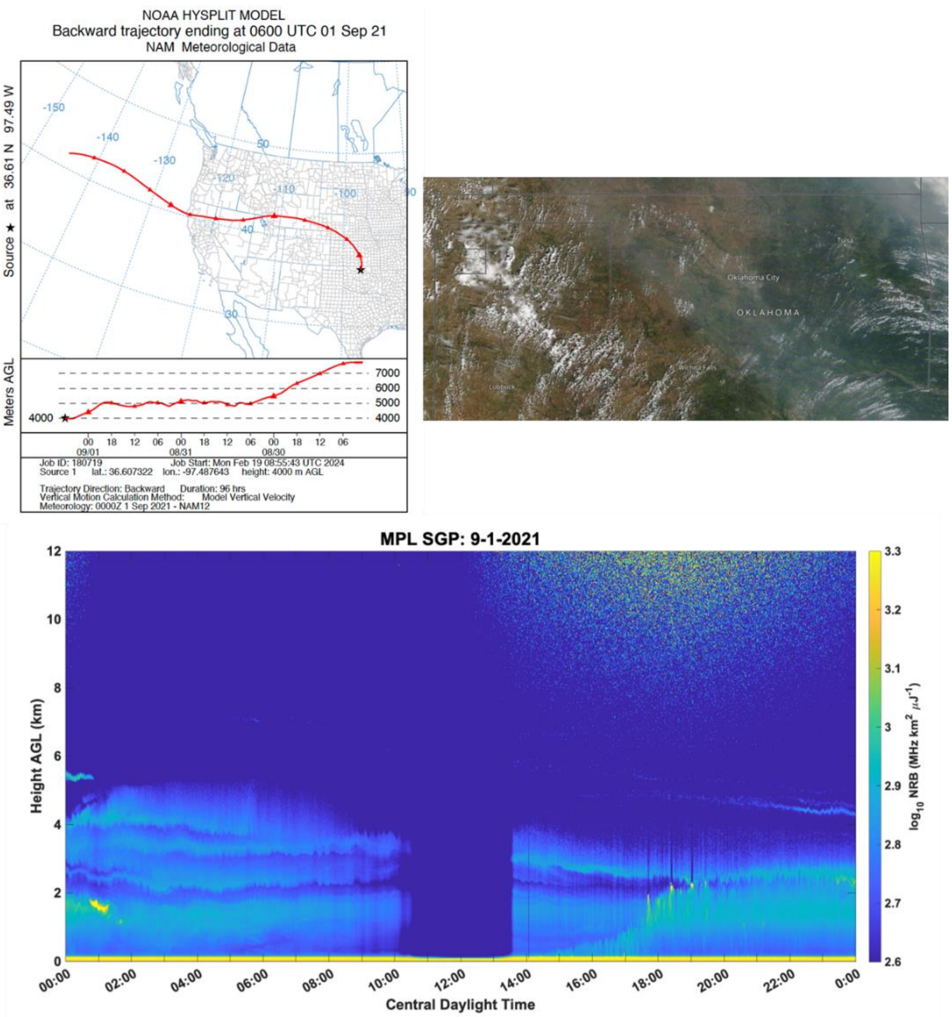

Appendix B 17 Same as B.1 for September 1, 2021.

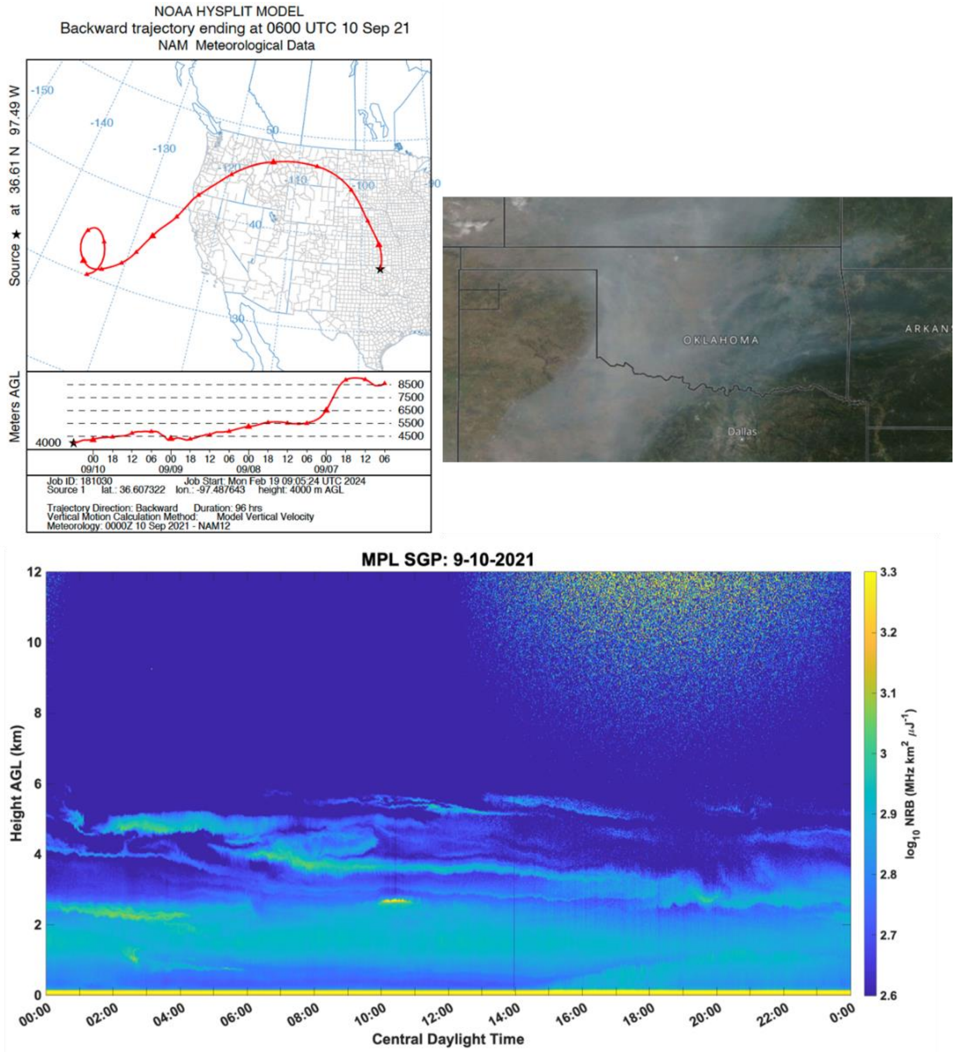

Appendix B 18 Same as B.1 for September 10, 2021.

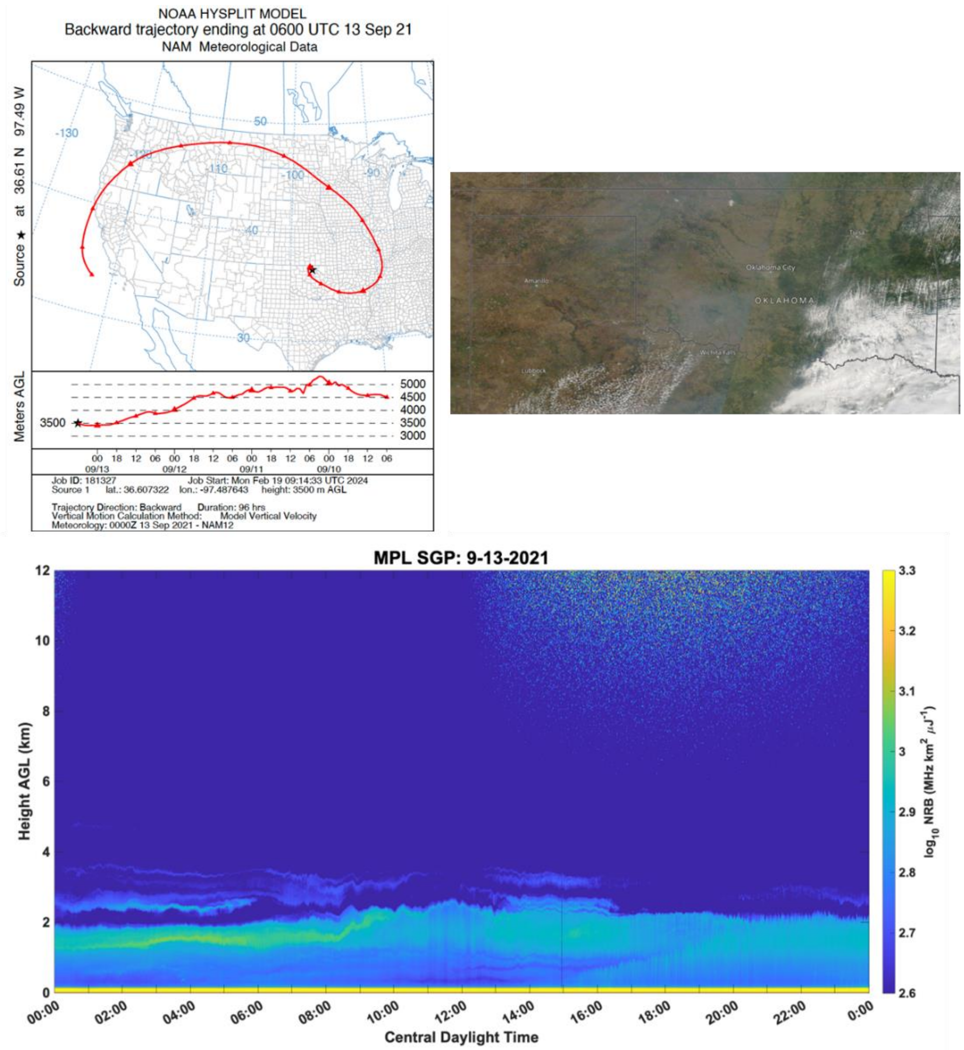

Appendix B 19 Same as B.1 for September 13, 2021.

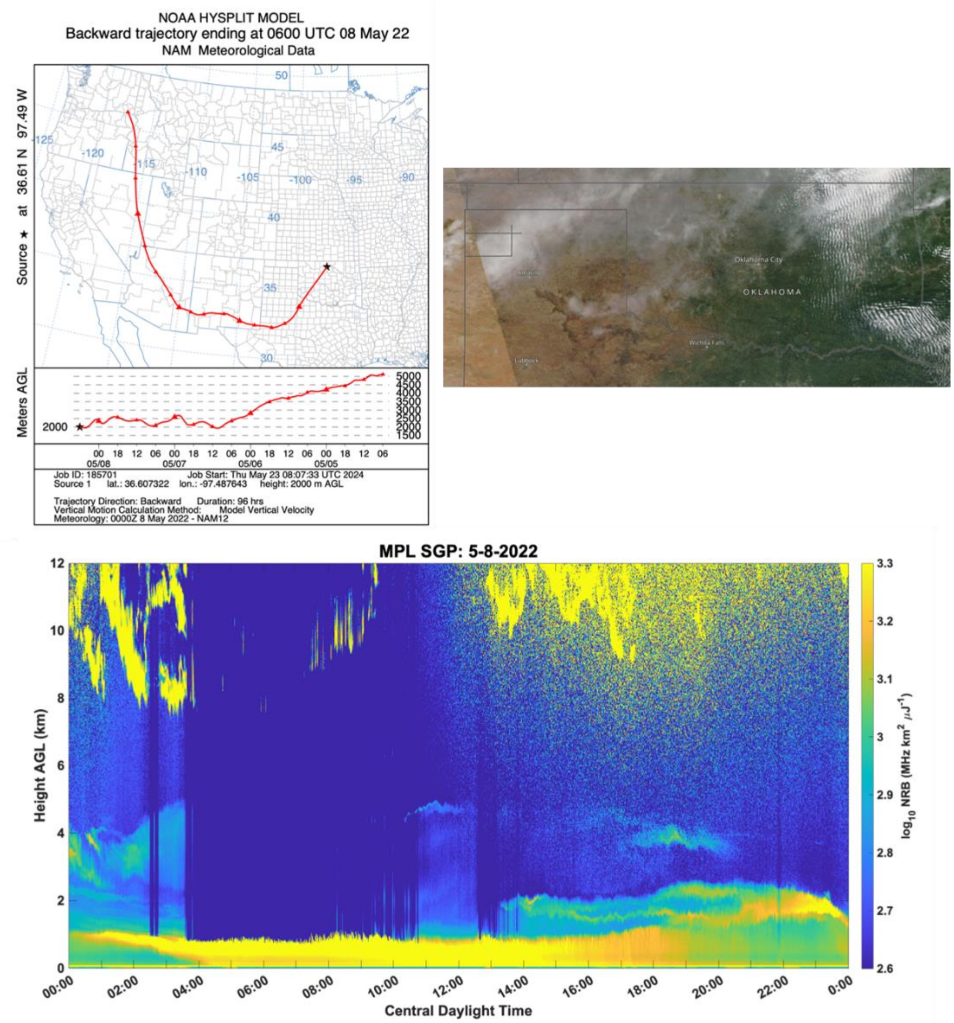

Appendix B 20 Same as B.1 for May 8, 2022.

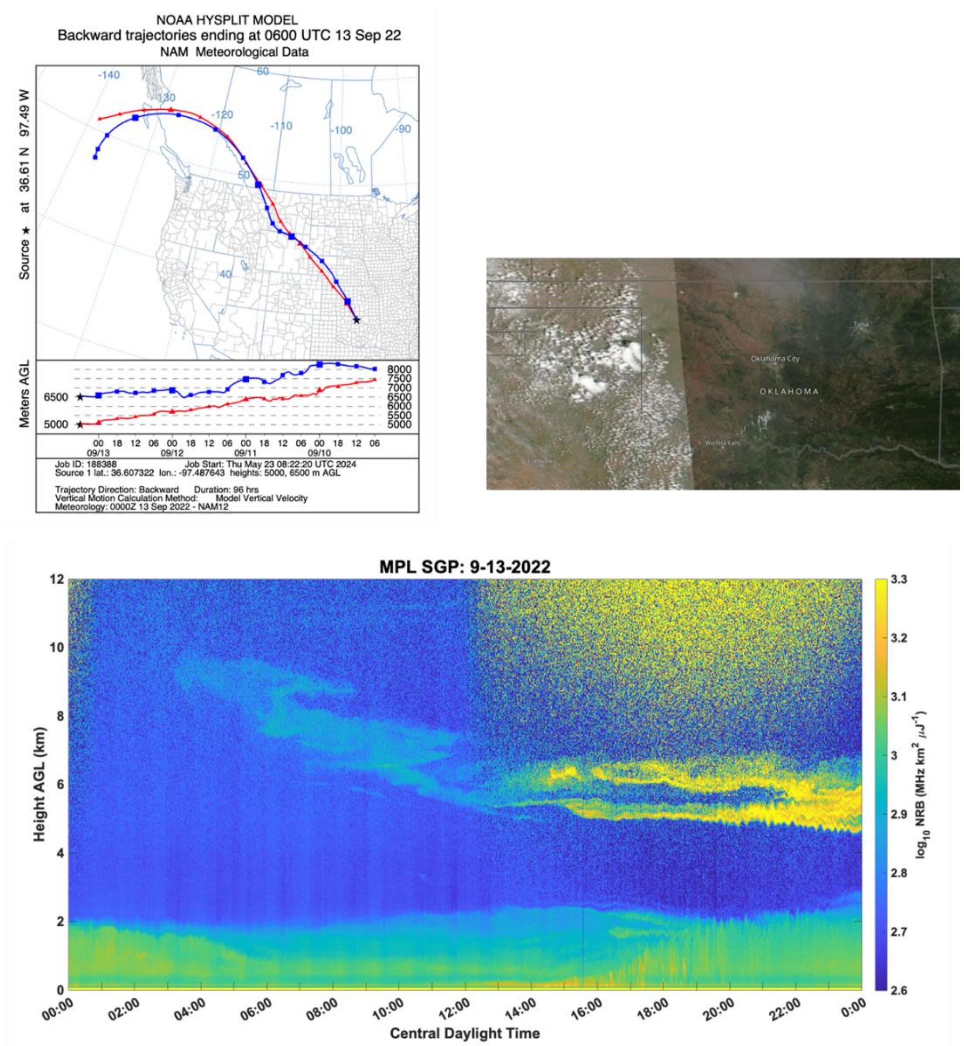

Appendix B 21 Same as B.1 for September 13, 2022.

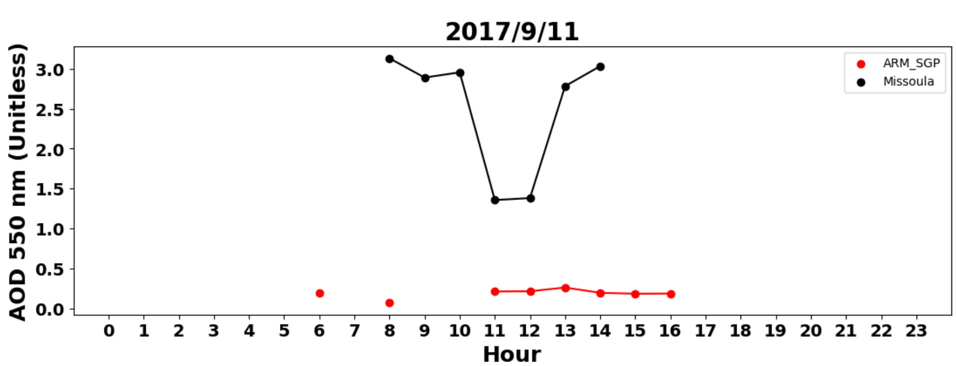

Appendix C 1 Hourly AOD$_{500\ nm}$ compared at Billings, OK (red) and the plumes source (black) on 9/11/2017.

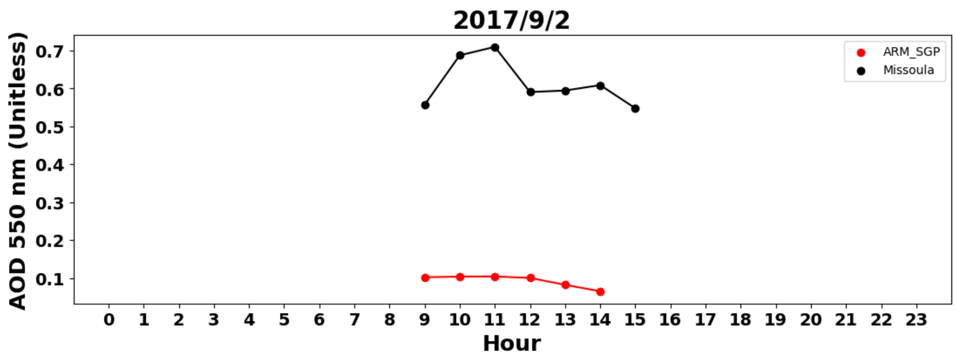

Appendix C 2 Same as C.1 for 9/2/2017.

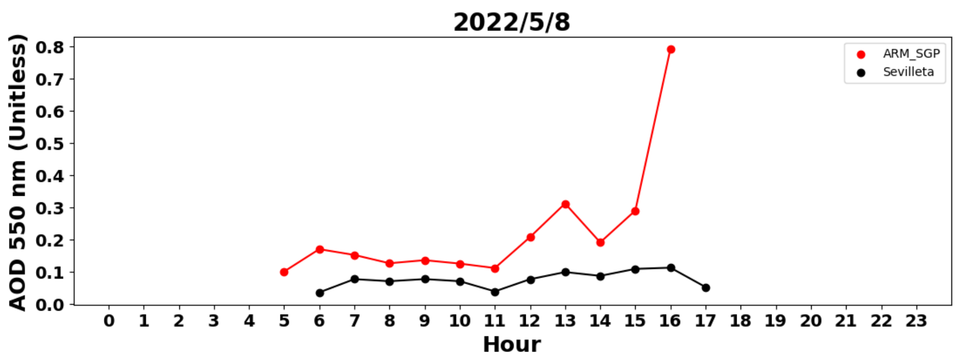

Appendix C 3 Same as C.1 for 5/8/2022.

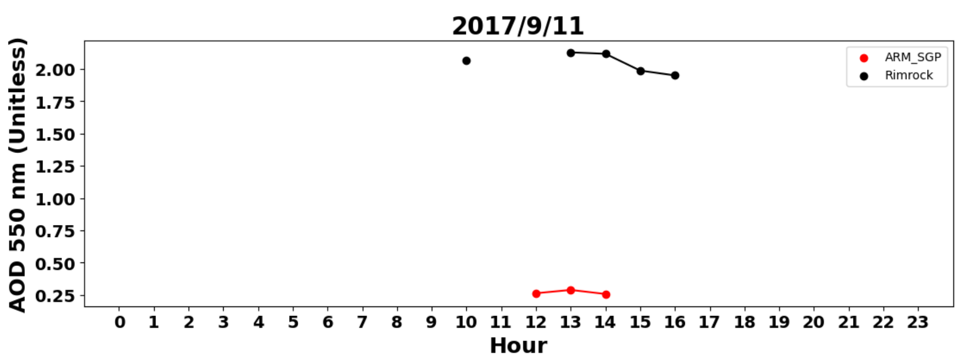

Appendix C 4 Same as C.1 for 9/11/2017.

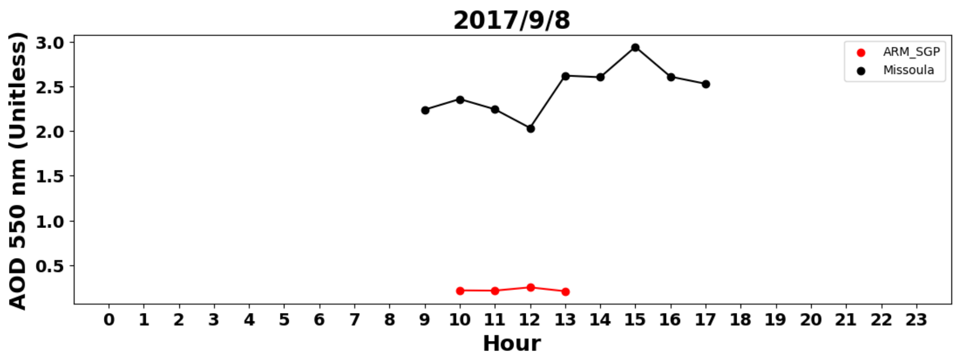

Appendix C 5 Same as C.1 for 9/8/2017.

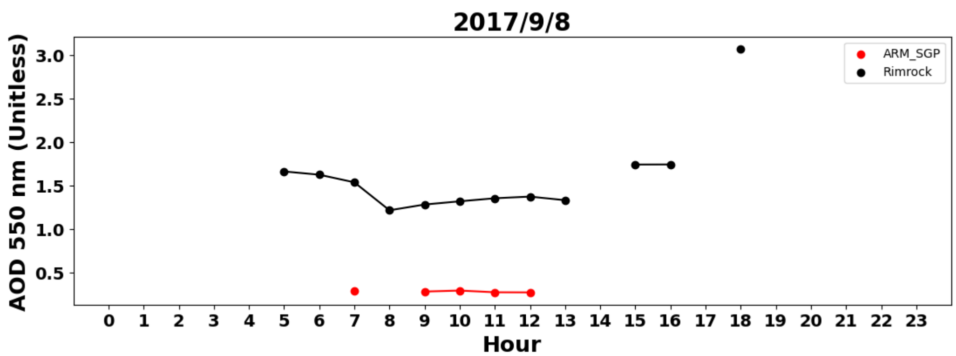

Appendix C 6 Same as C.1 for 9/8/2017.

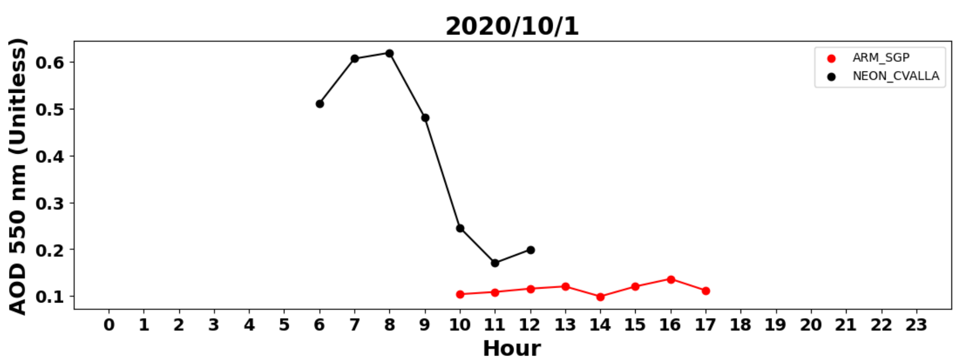

Appendix C 7 Same as C.1 for 10/1/2020.

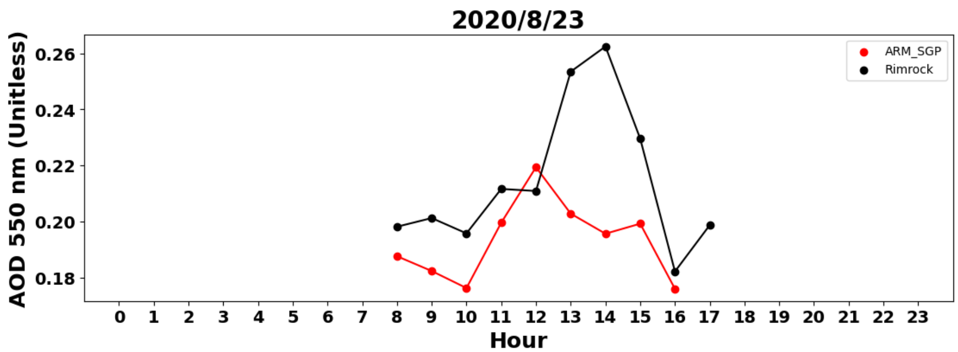

Appendix C 8 Same as C.1 for 8/23/2020.

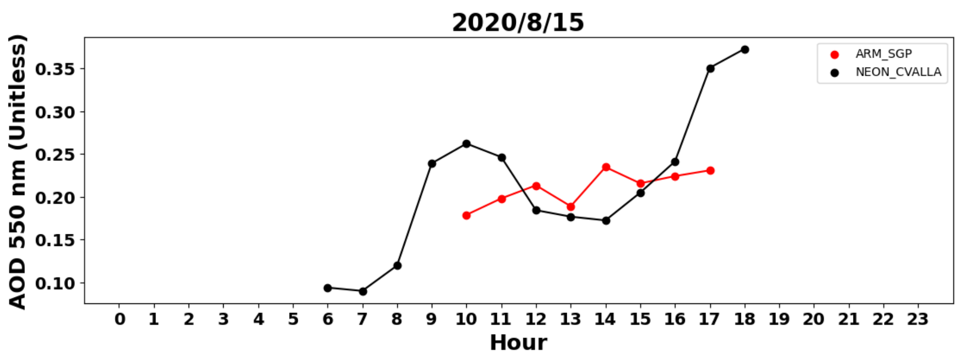

Appendix C 9 Same as C.1 for 8/15/2020.

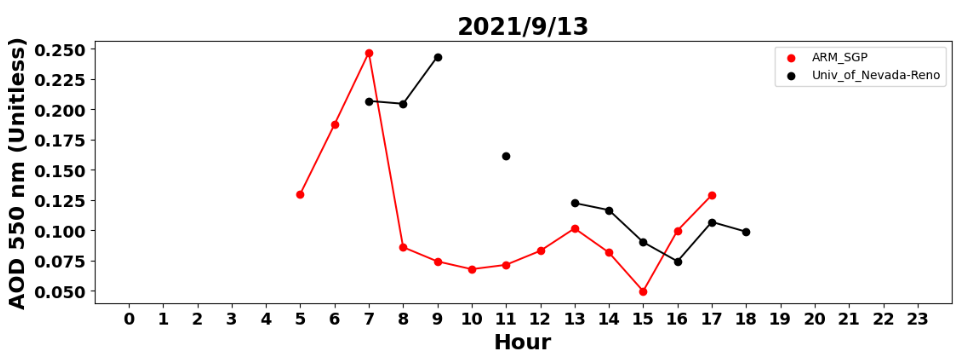

Appendix C 10 Same as C.1 for 9/13/2021.

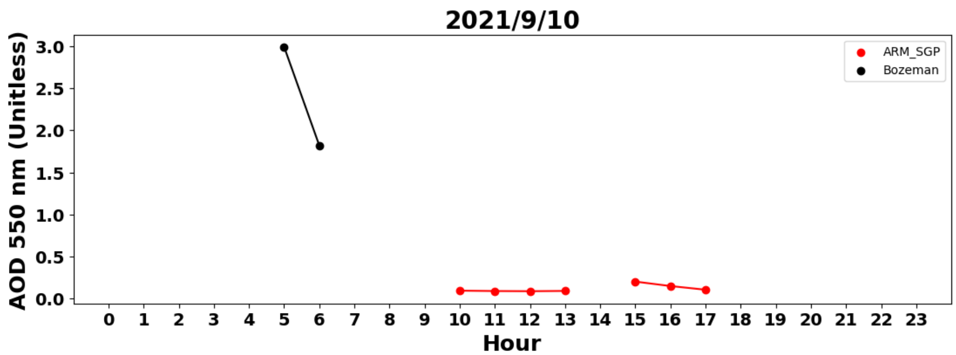

Appendix C 11 Same as C.1 for 9/10/2021.

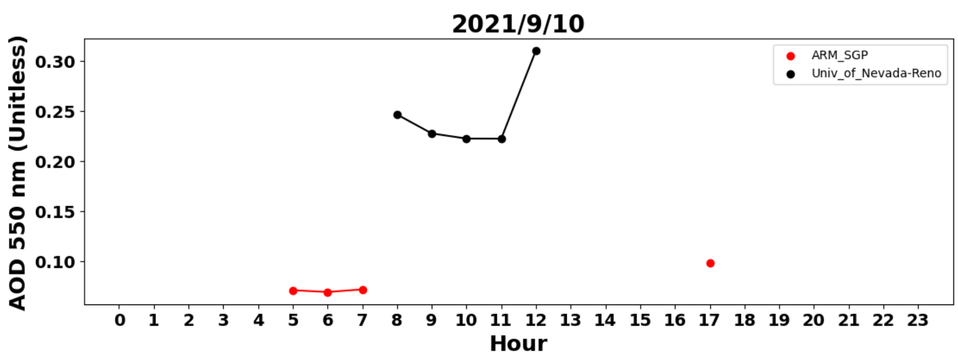

Appendix C 12 Same as C.1 for 9/10/2021.

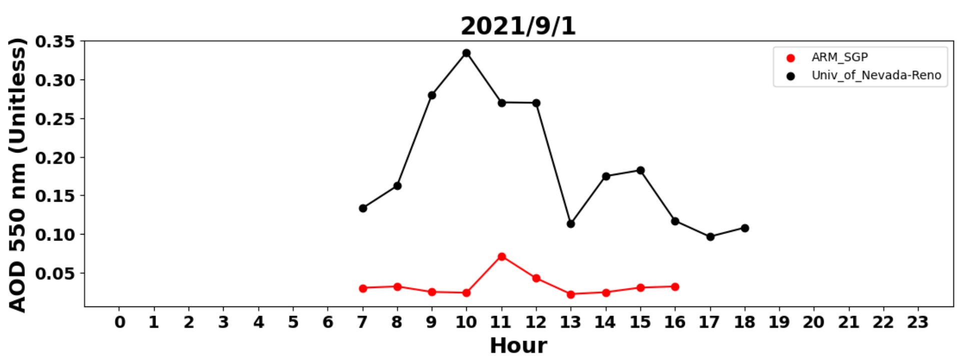

Appendix C 13 Same as C.1 for 9/1/2021.

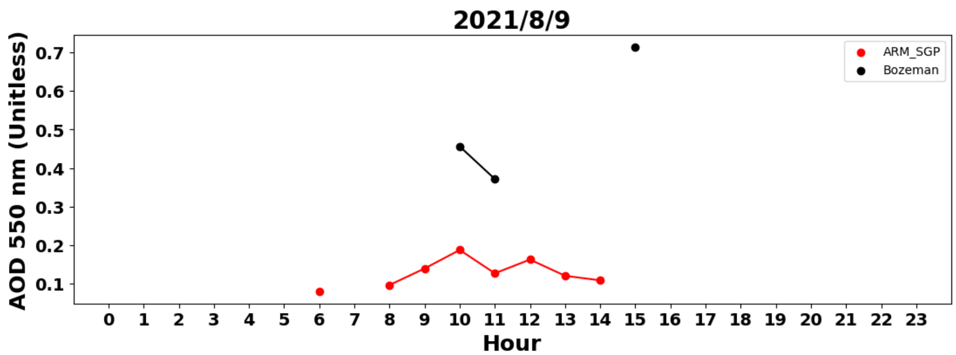

Appendix C 14 Same as C.1 for 8/9/2021.

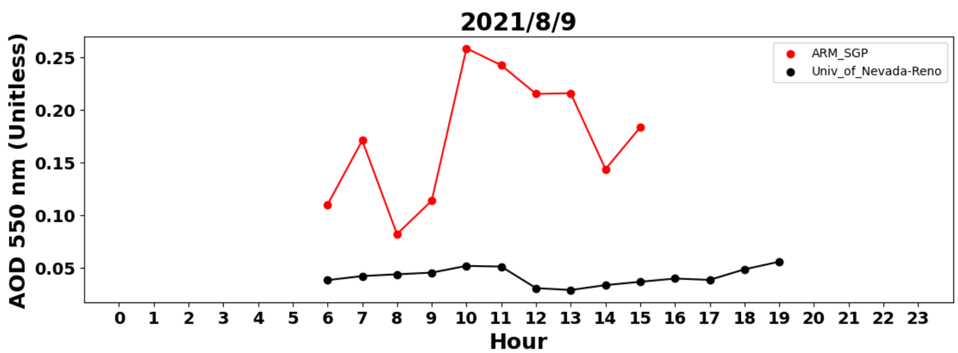

Appendix C 15 Same as C.1 for 8/9/2021.

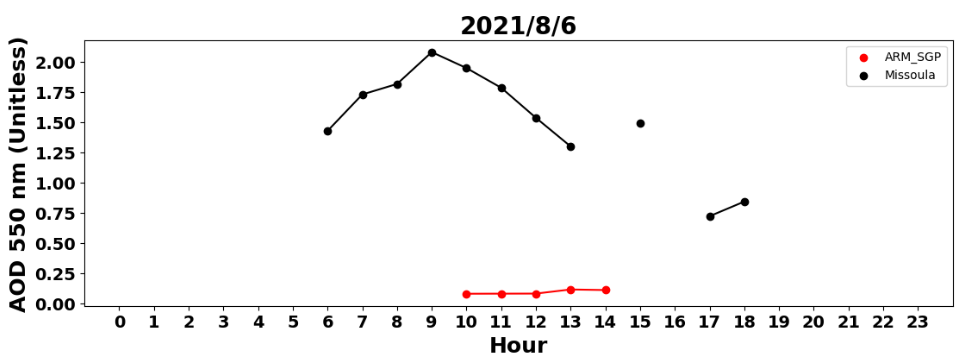

Appendix C 16 Same as C.1 for 8/6/2021.

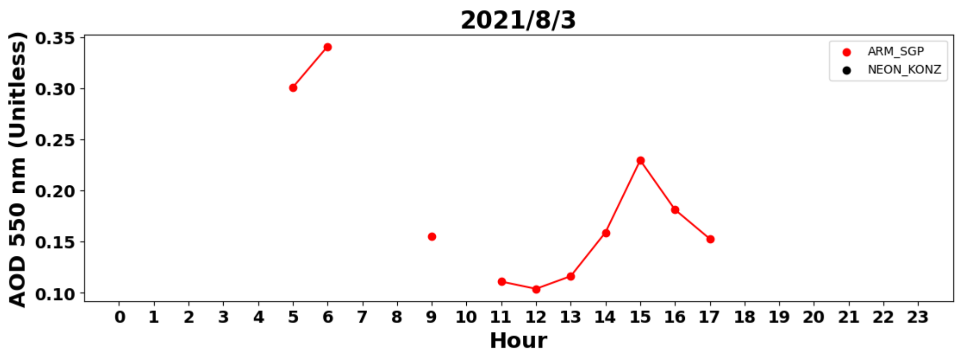

Appendix C 17 Same as C.1 for 8/3/2021.

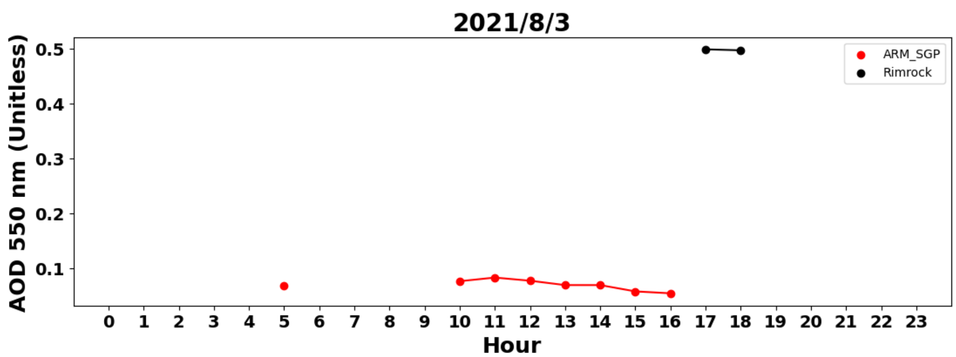

Appendix C 18 Same as C.1 for 8/3/2021.

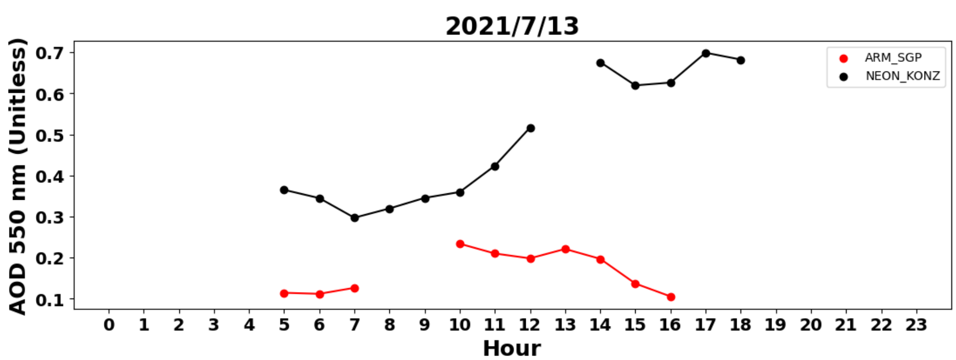

Appendix C 19 Same as C.1 for 7/13/2021.

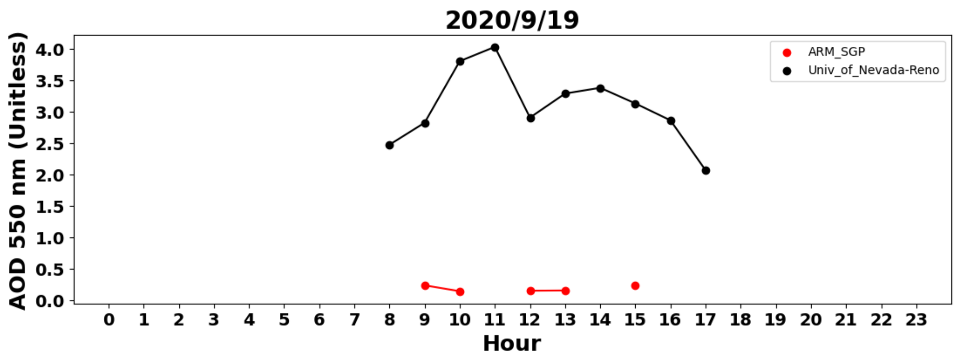

Appendix C 20 Same as C.1 for 9/19/2020.

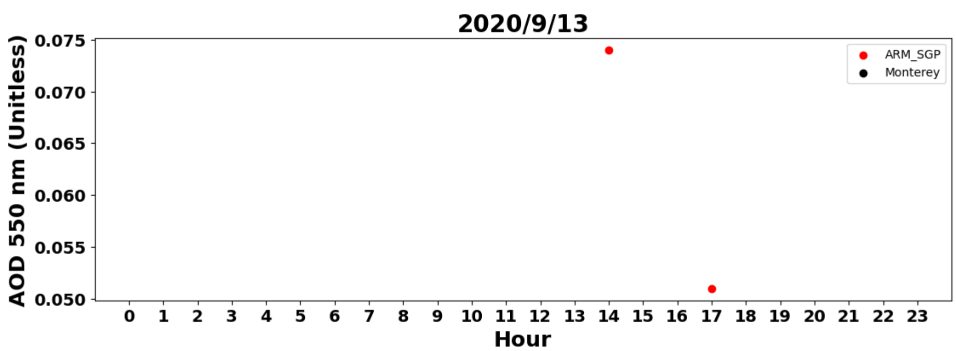

Appendix C 21 Same as C.1 for 9/13/2020.

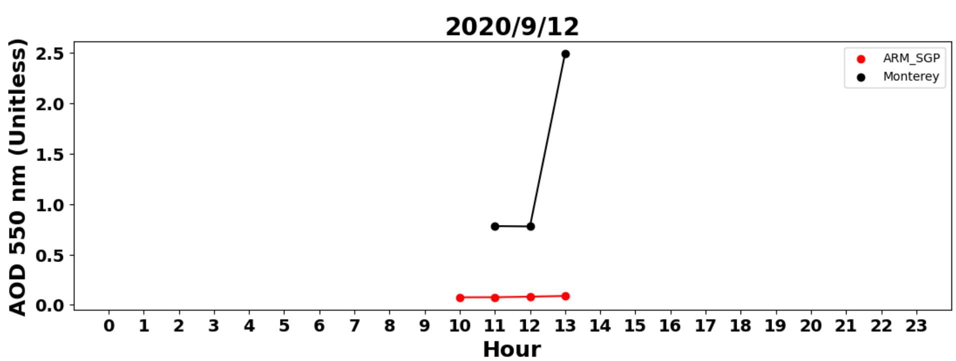

Appendix C 22 Same as C.1 for 9/12/2020.

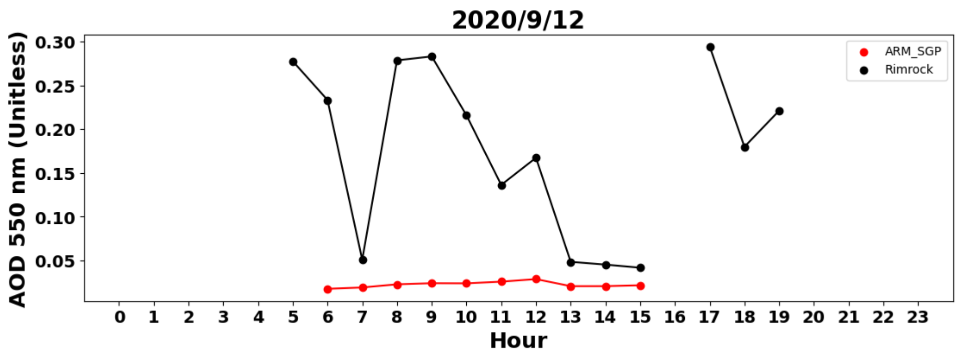

Appendix C 23 Same as C.1 for 9/12/2020.

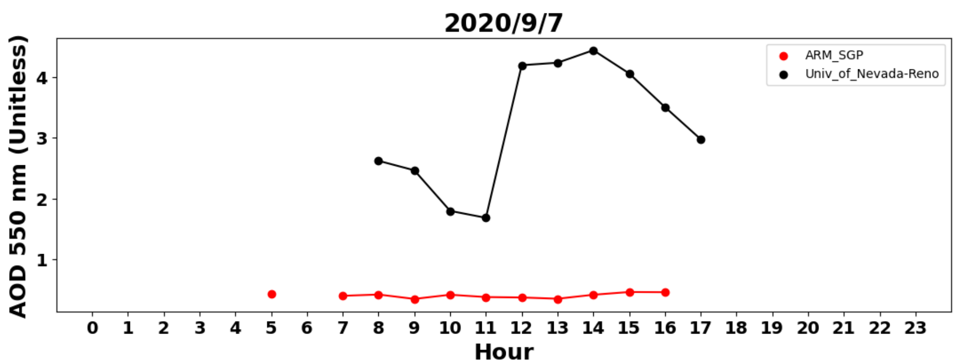

Appendix C 24 Same as C.1 for 9/7/2020.

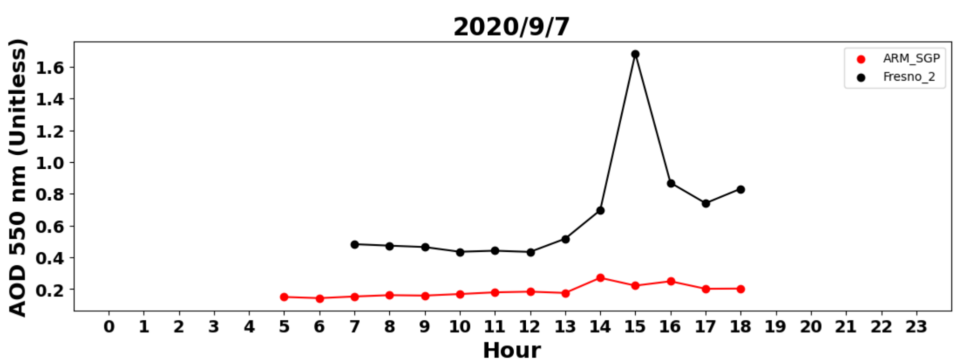

Appendix C 25 Same as C.1 for 9/7/2020.

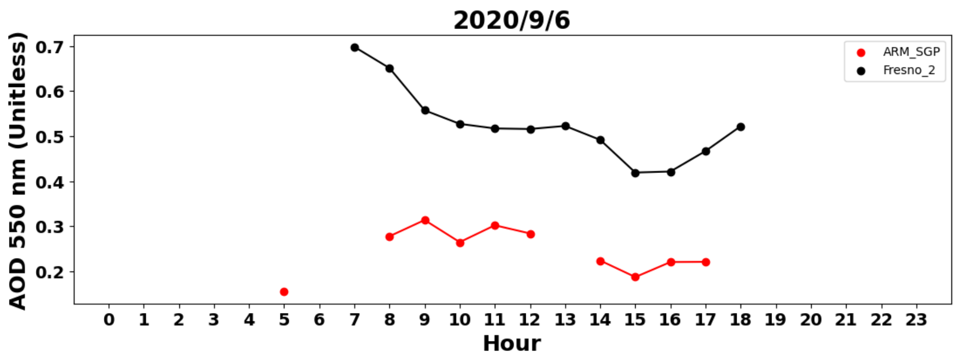

Appendix C 26 Same as C.1 for 9/6/2020.

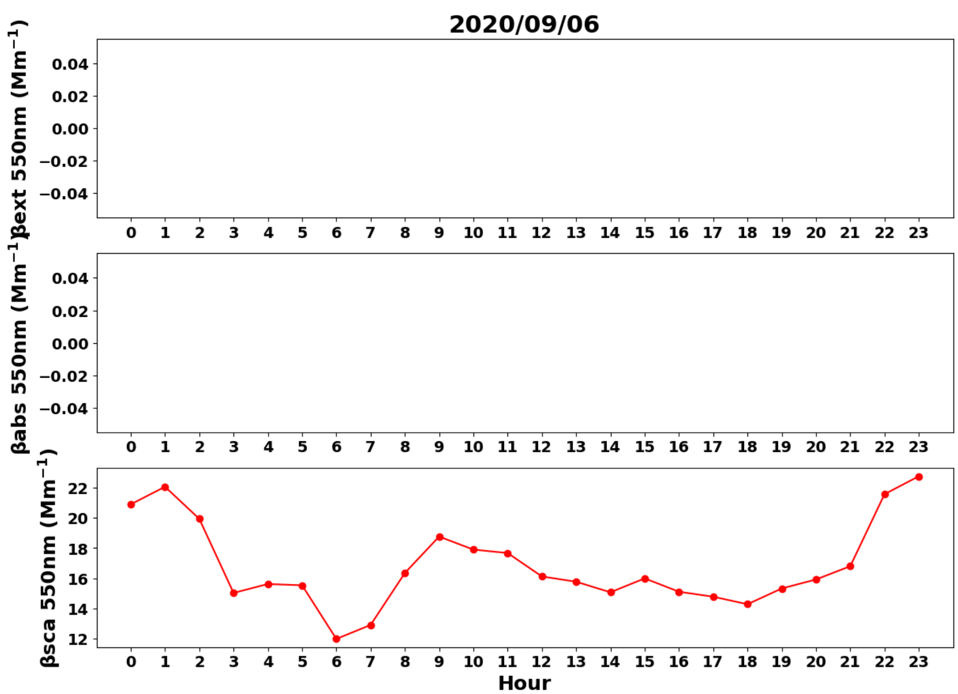

Appendix D 1 Hourly β_{ext} at 550 nm (Mm^{-1}) (top), β_a at 550 nm (Mm^{-1}) (middle), β_s at 550 nm (Mm^{-1}) (bottom) 9/06/2020.

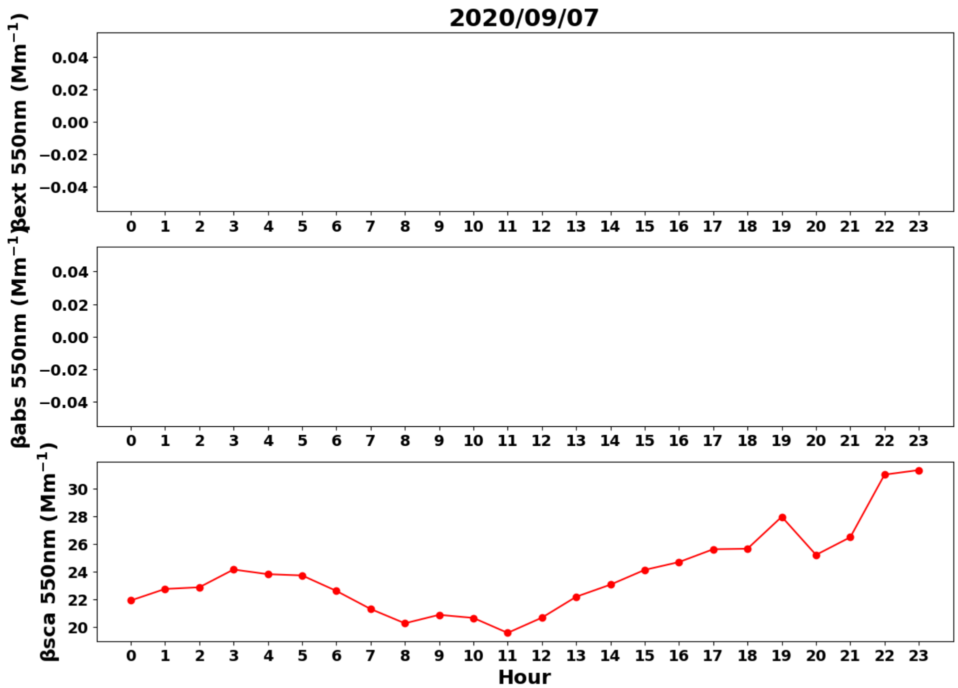

Appendix D 2 Same as D.1 for 9/07/2020.

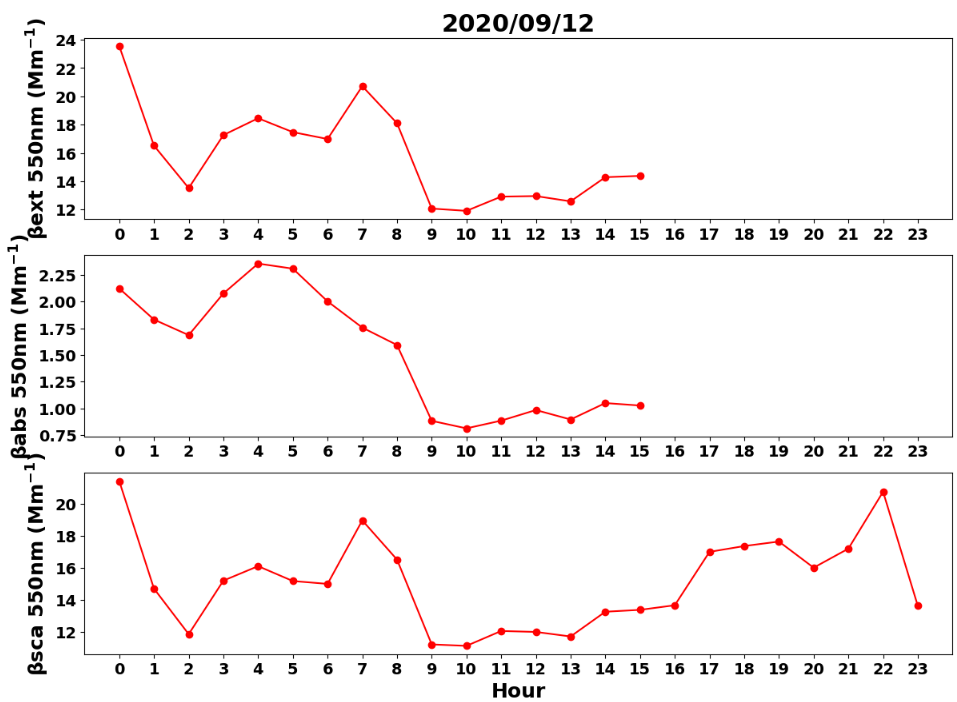

Appendix D 3 Same as D.1 for 9/12/2020.

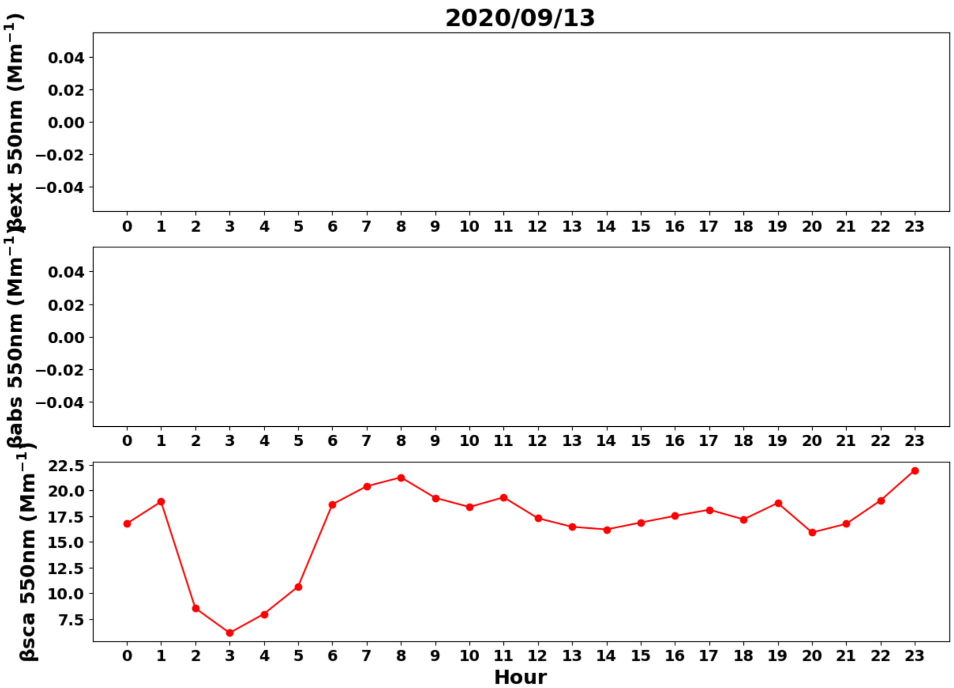

Appendix D 4 Same as D.1 for 9/13/2020.

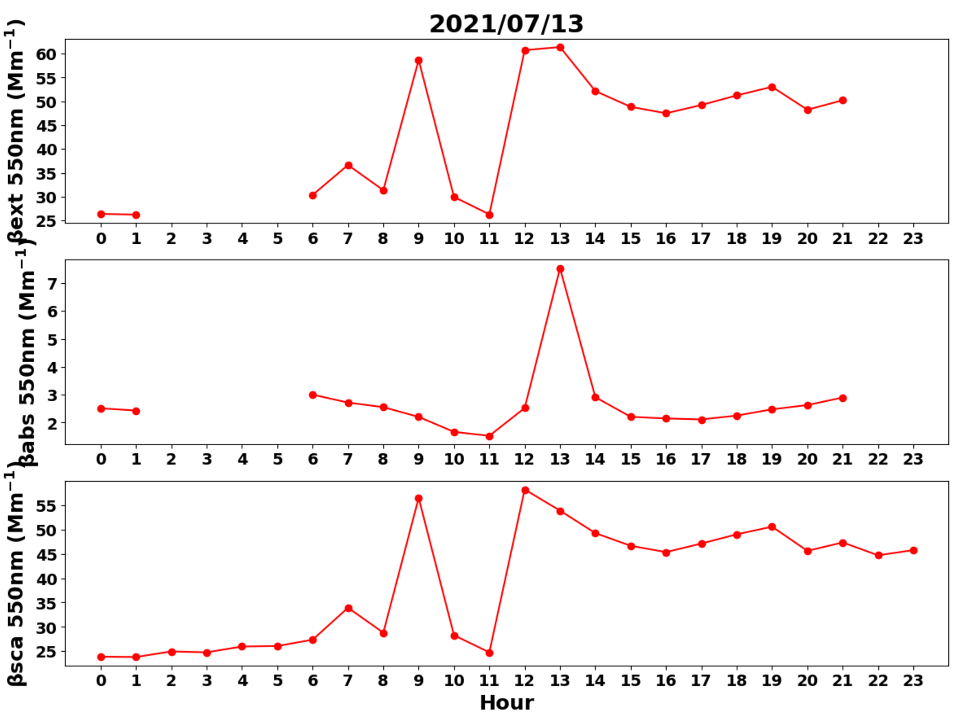

Appendix D 5 Same as D.1 for 7/13/2021.

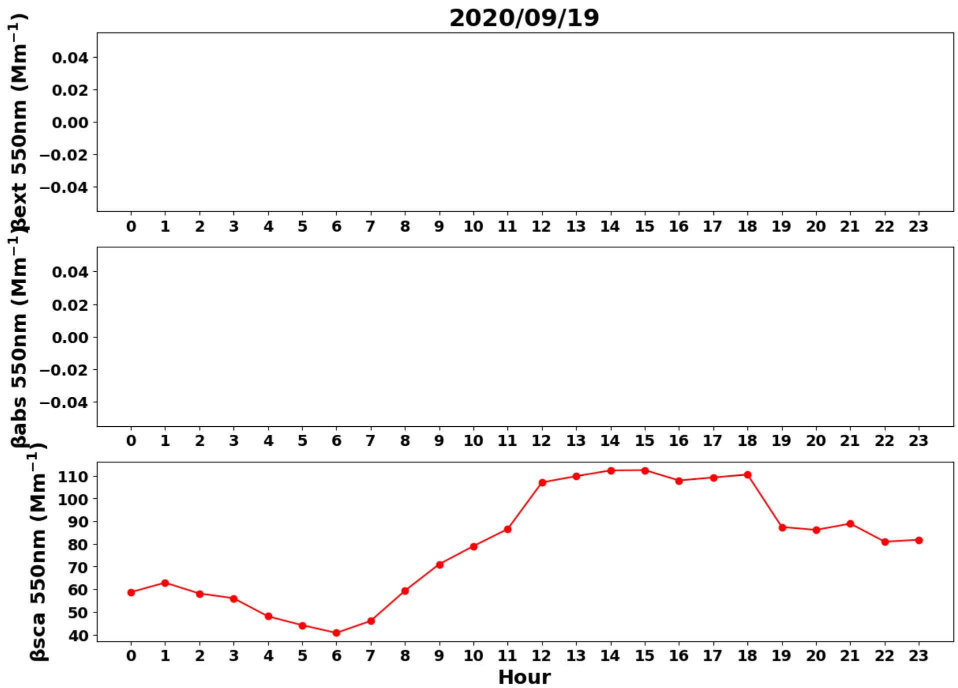

Appendix D 6 Same as D.1 for 9/19/2020.

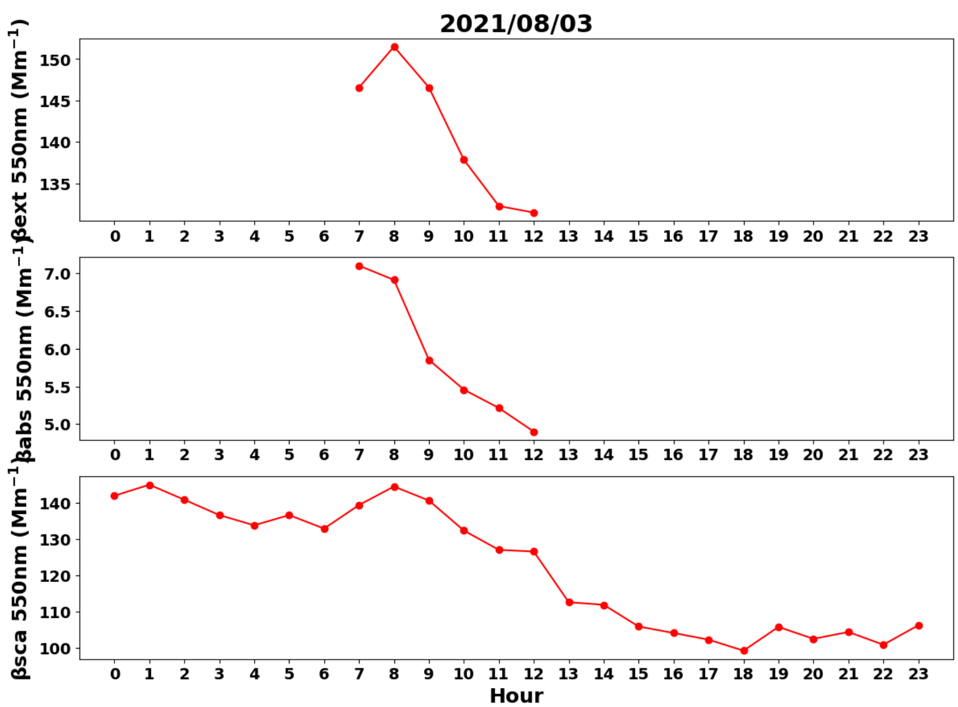

Appendix D 7 Same as D.1 for 8/3/2021.

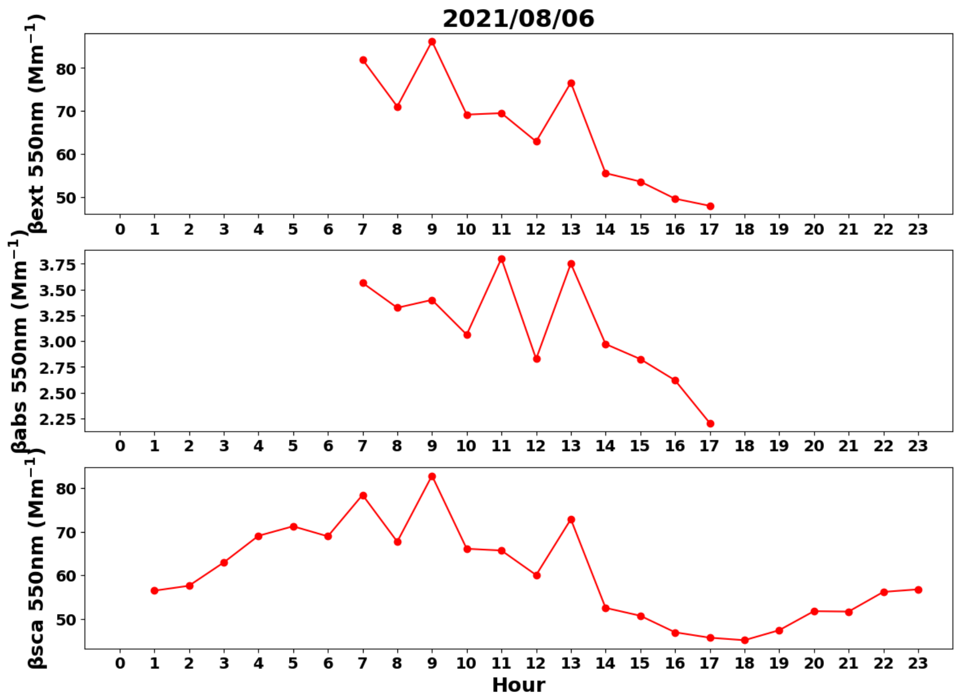

Appendix D 8 Same as D.1 for 8/6/2021.

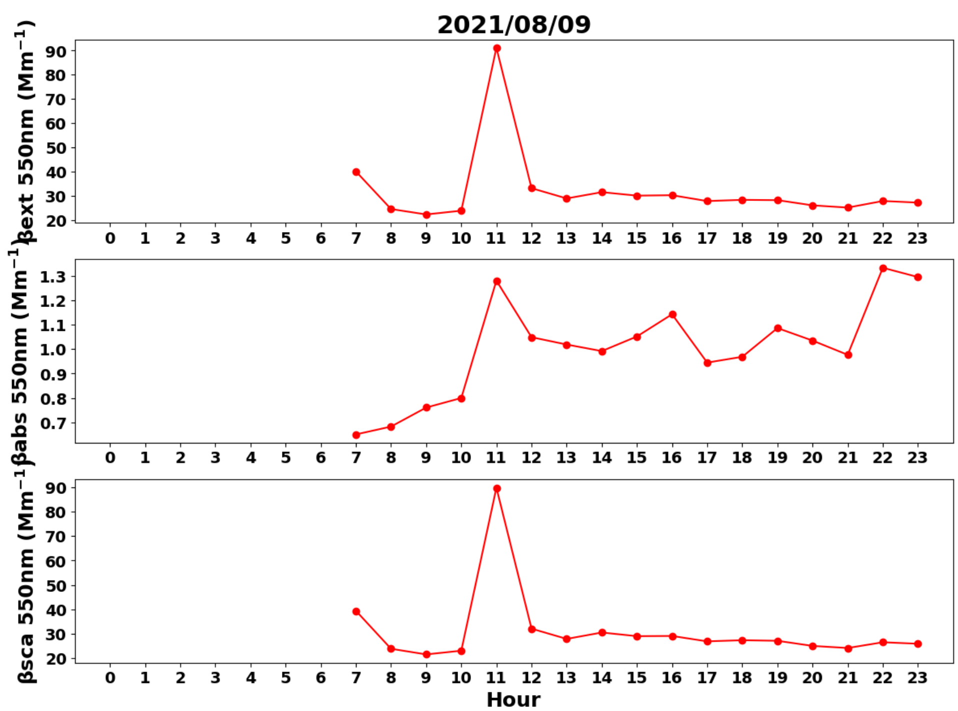

Appendix D 9 Same as D.1 for 8/9/2021.

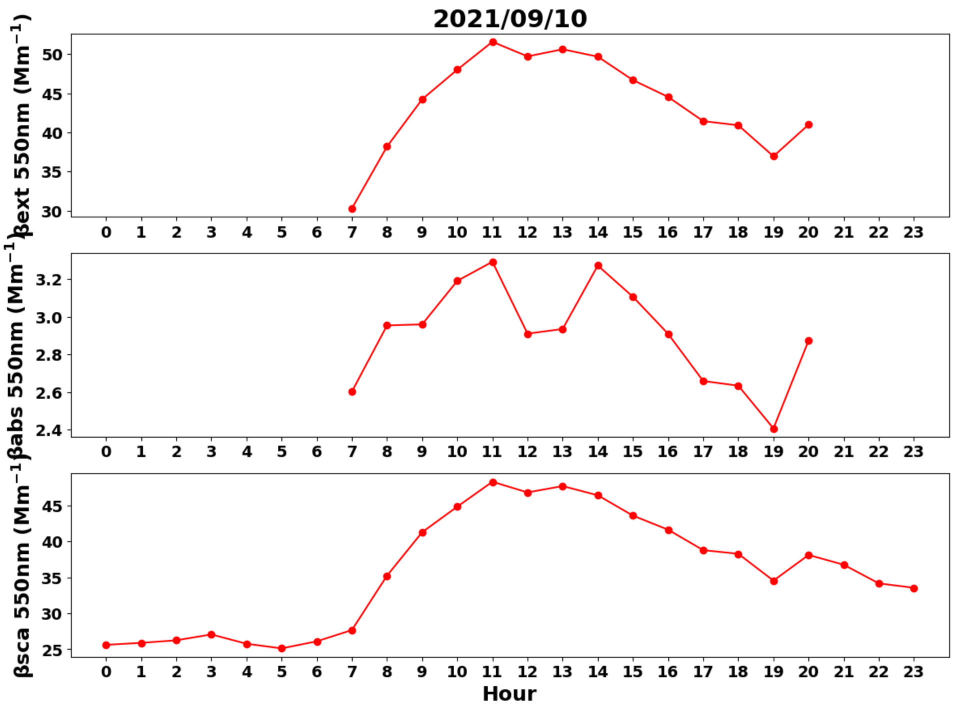

Appendix D 10 Same as D.1 for 9/10/2021.

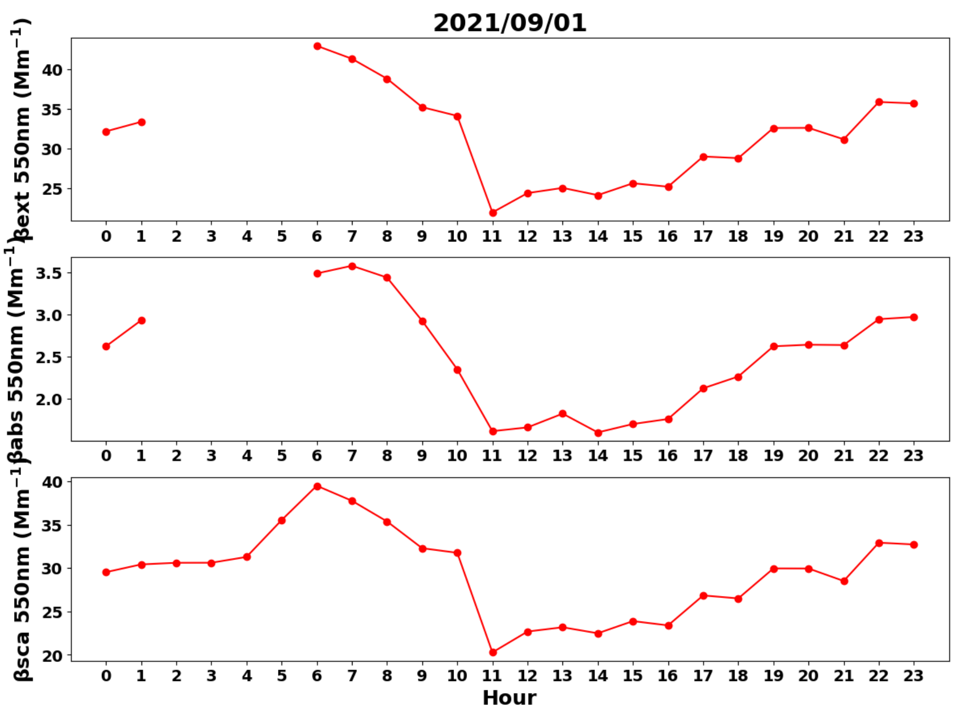

Appendix D 11 Same as D.1 for 9/1/2021.

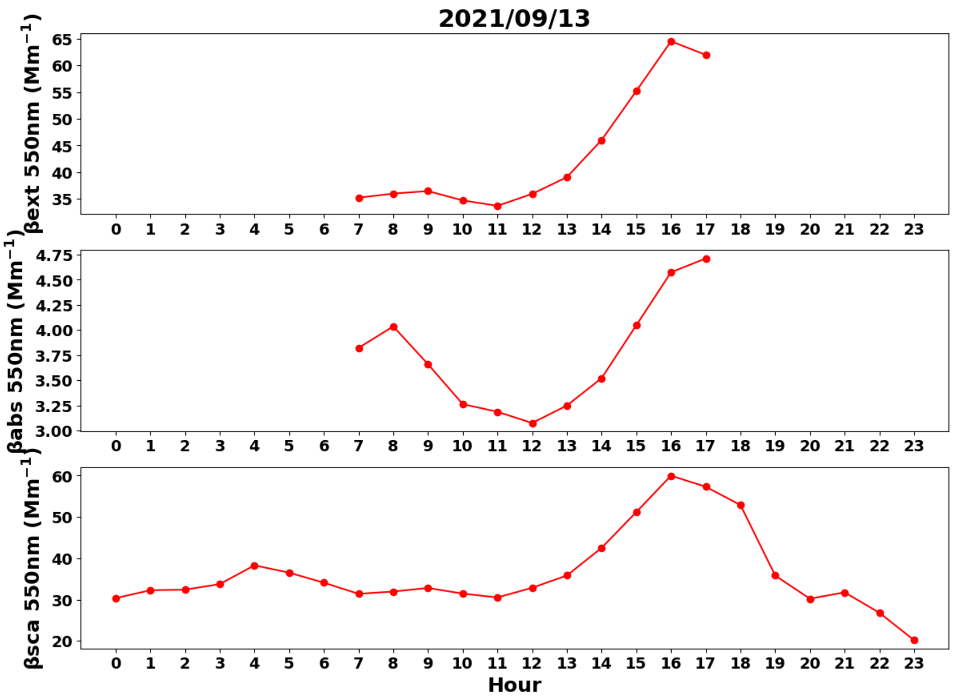

Appendix D 12 Same as D.1 for 9/13/2021.

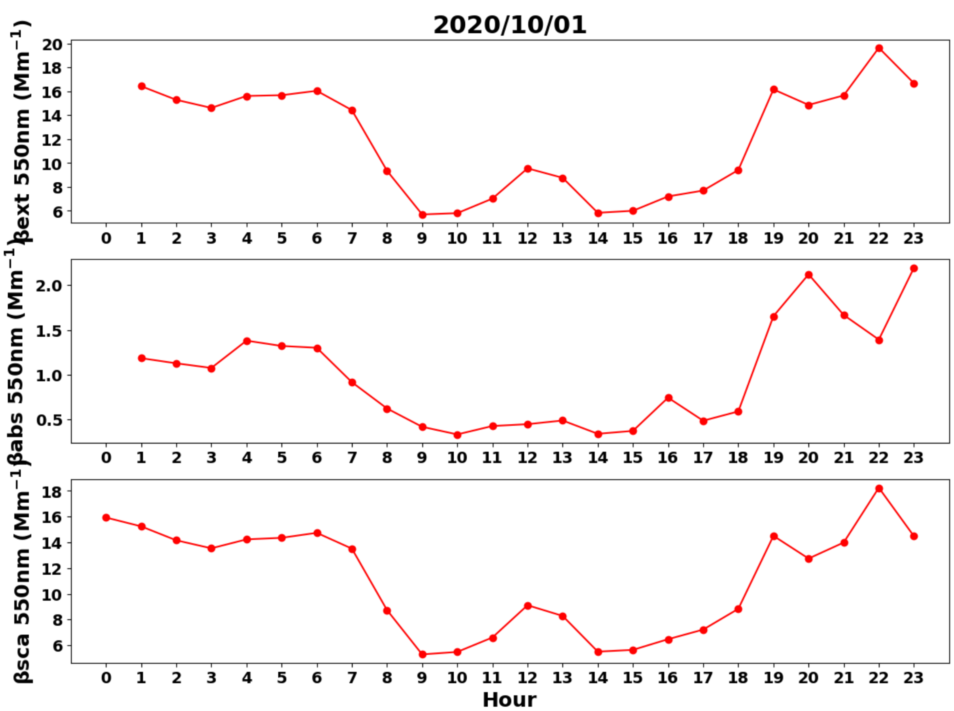

Appendix D 13 Same as D.1 for 10/1/2020.

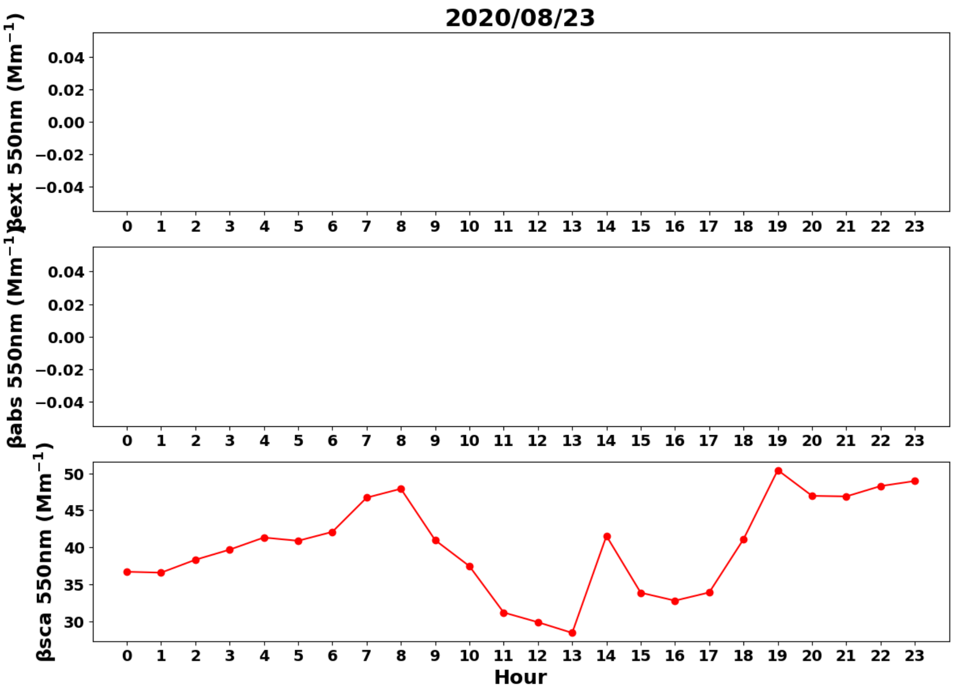

Appendix D 14 Same as D.1 for 8/23/2020.

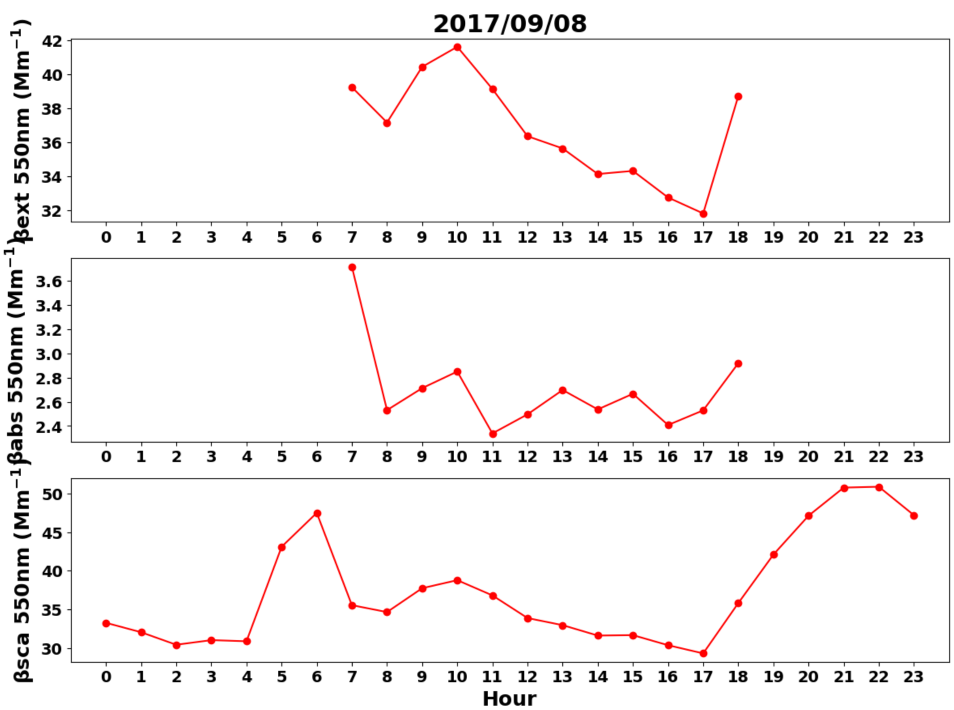

Appendix D 15 Same as D.1 for 9/8/2017.

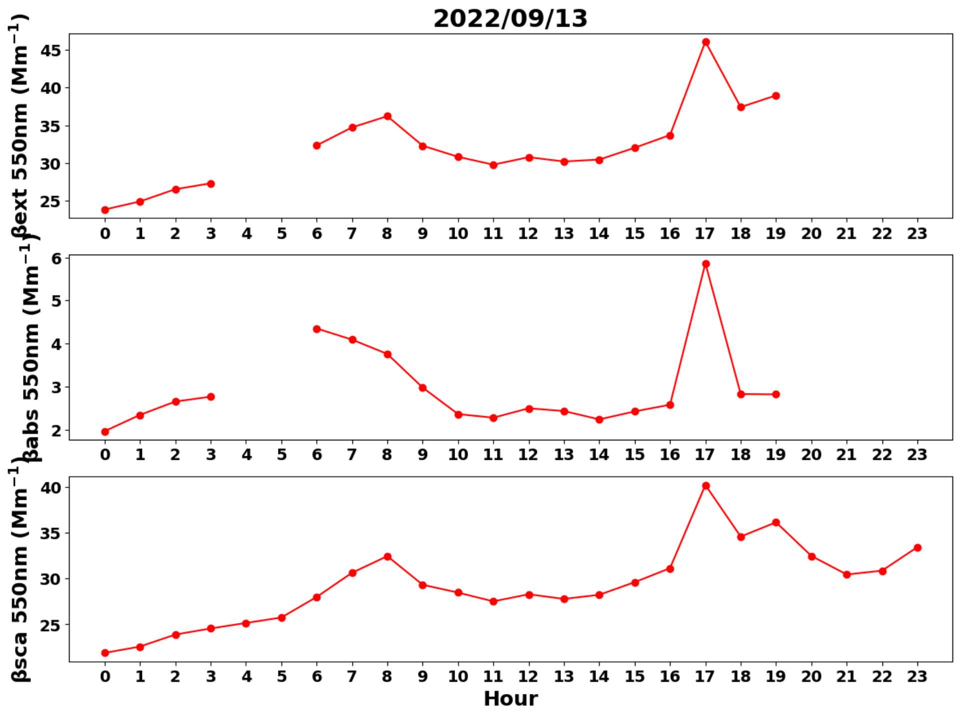

Appendix D 16 Same as D.1 for 9/13/2022.

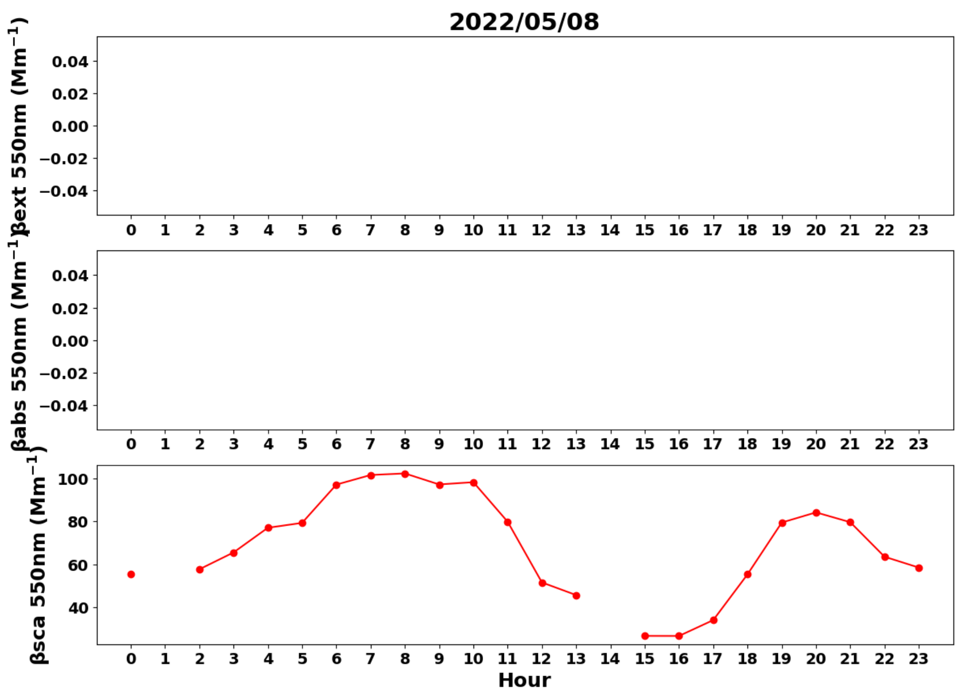

Appendix D 17 Same as D.1 for 5/8/2022.

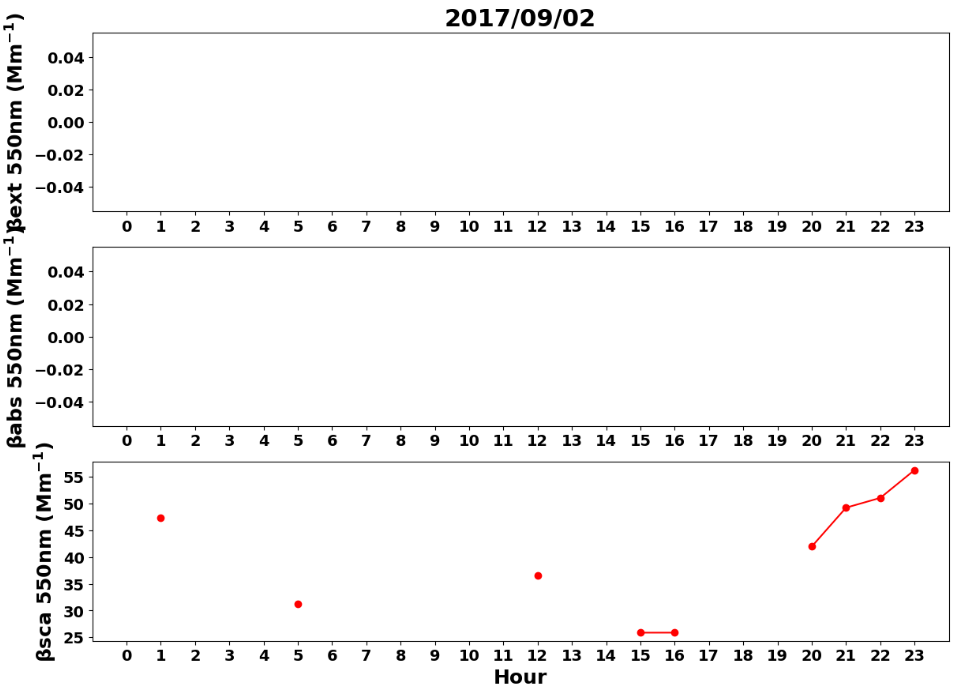

Appendix D 18 Same as D.1 for 9/2/2017.

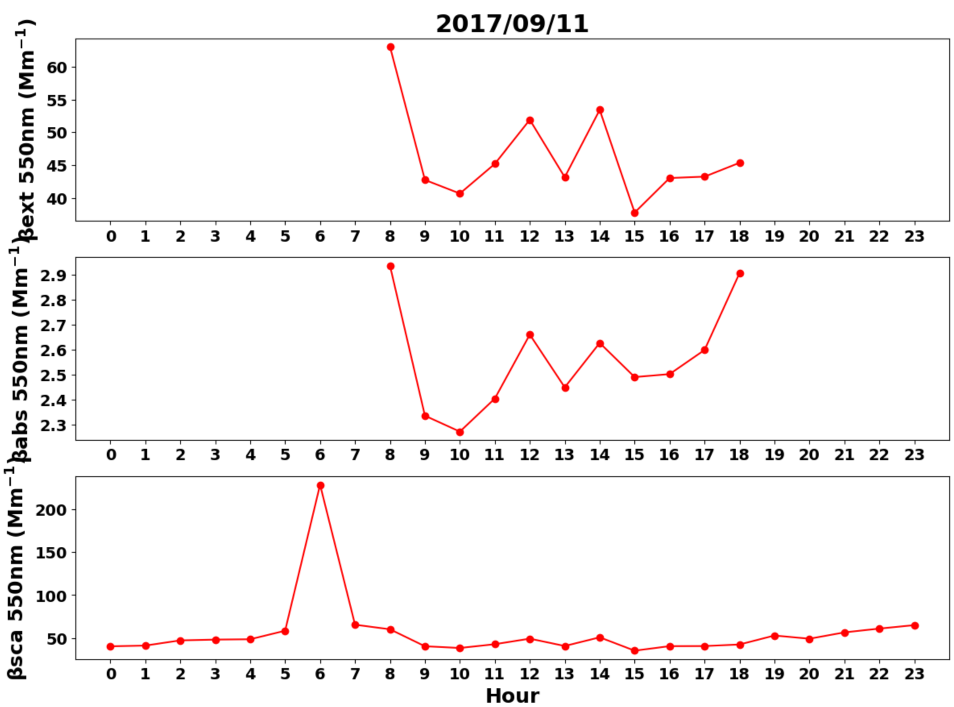

Appendix D 19 Same as D.1 for 9/11/2017.

References

Anderson, T.L. and Ogren, J.A. (1998). Determining Aerosol Radiative Properties Using the TSI 3563 Integrating Nephelometer. *Aerosol Science and Technology* 29 (1):57–69. doi:10.1080/02786829808965551.

Ångström, A. (1929). On the Atmospheric Transmission of Sun Radiation and on Dust in the Air. *Geografiska Annaler* 11:156–166.

Barnes, W.L. and Salomonson, V.V. (1992). MODIS: a global imaging spectroradiometer for the Earth Observing System.*, in Optical Technologies for Aerospace Sensing: A Critical Review,* Presented at the Optical Technologies for Aerospace Sensing: A Critical Review, SPIE, pp. 280–302.

Barnes, W.L., Xiong, X., and Salomonson, V.V. (2003). Status of terra MODIS and aqua modis. *Advances in Space Research, Calibration, Characterization of Satellite Sensors, Physical Parameters Derived from Satellite Data* 32 (11):2099–2106. doi:10.1016/S0273-1177(03)90529-1.

Bergstrom, R.W., Pilewskie, P., Russell, P.B., Redemann, J., Bond, T.C., Quinn, P.K., and Sierau, B. (2007). Spectral absorption properties of atmospheric aerosols. *Atmospheric Chemistry and Physics* 7 (23):5937–5943. doi:10.5194/acp-7-5937-2007.

Bian, Q., Ford, B., Pierce, J.R., and Kreidenweis, S.M. (2020). A Decadal Climatology of Chemical, Physical, and Optical Properties of Ambient Smoke in the Western and Southeastern United States. *Journal of Geophysical Research: Atmospheres* 125 (1):e2019JD031372. doi:10.1029/2019JD031372.

Bond, T.C., Anderson, T.L., and Campbell, D. (1999). Calibration and Intercomparison of Filter-Based Measurements of Visible Light Absorption by Aerosols. *Aerosol Science and Technology* 30 (6):582–600. doi:10.1080/027868299304435.

Campbell, J.R., Hlavka, D.L., Welton, E.J., Flynn, C.J., Turner, D.D., Spinhirne, J.D., Scott, V.S., and Hwang, I.H. (2002). Full-Time, Eye-Safe Cloud and Aerosol Lidar Observation at Atmospheric Radiation Measurement Program Sites: Instruments and Data Processing. *J. Atmos. Oceanic Technol.* 19 (4):431–442. doi:10.1175/1520-0426(2002)019<0431:FTESCA>2.0.CO;2.

Carboni, E., Thomas, G.E., Sayer, A.M., Siddans, R., Poulsen, C.A., Grainger, R.G., Ahn, C., Antoine, D., Bevan, S., Braak, R., Brindley, H., DeSouza-Machado, S., Deuzé, J.L., Diner, D., Ducos, F., Grey, W., Hsu, C., Kalashnikova, O.V., Kahn, R., North, P.R.J., Salustro, C., Smith, A., Tanré, D., Torres, O., and Veihelmann, B. (2012). Intercomparison of desert dust optical depth from satellite measurements. *Atmospheric Measurement Techniques* 5 (8):1973–2002. doi:10.5194/amt-5-1973-2012.

Cascio, W.E. (2017). Wildland fire smoke and human health. *Sci. Total Environ.* 624:586–595. doi:10.1016/j.scitotenv.2017.12.086.

Chowdhury, S., Hänninen, R., Sofiev, M., and Aunan, K. (2024). Fires as a source of annual ambient PM2.5 exposure and chronic health impacts in Europe. *Science of The Total Environment* 922:171314. doi:10.1016/j.scitotenv.2024.171314.

Chylek, P. and Wong, J. (1995). Effect of absorbing aerosols on global radiation budget. *Geophysical Research Letters* 22 (8):929–931. doi:10.1029/95GL00800.

Colarco, P.R., Schoeberl, M.R., Doddridge, B.G., Marufu, L.T., Torres, O., and Welton, E.J. (2004). Transport of smoke from Canadian forest fires to the surface near Washington, D.C.: Injection height, entrainment, and optical properties. *Journal of Geophysical Research: Atmospheres* 109 (D6). doi:10.1029/2003JD004248.

Crockett, J. and Westerling, A. (2018). Greater Temperature and Precipitation Extremes Intensify Western U.S. Droughts, Wildfire Severity, and Sierra Nevada Tree Mortality. *Journal of Climate* 31:341–354. doi:10.1175/JCLI-D-17-0254.1.

Crouse, D.L., Peters, P.A., van Donkelaar, A., Goldberg, M.S., Villeneuve, P.J., Brion, O., Khan, S., Atari, D.O., Jerrett, M., Pope, C.A., Brauer, M., Brook, J.R., Martin, R.V., Stieb, D., and Burnett, R.T. (2012). Risk of nonaccidental and cardiovascular mortality in relation to long-term exposure to low concentrations of fine particulate matter: a Canadian national-level cohort study. *Environ Health Perspect* 120 (5):708–714. doi:10.1289/ehp.1104049.

Dennison, P., Brewer, S., Arnold, J., and Moritz, M. (2014). Large wildfire trends in the western United States, 1984-2011. *Geophysical Research Letters* 41. doi:10.1002/2014GL059576.

Draxler, R. and Hess, G. (1998). An overview of the HYSPLIT_4 modelling system for trajectories. *Aust. Meteorol. Mag.* 47.

Draxler, R. and Hess, G. (1997). Description of the HYSPLIT_4 modelling system. *NOAA Tech. Mem. ERL ARL-224*.

Draxler, R.R. and Taylor, A.D. (1982). Horizontal Dispersion Parameters for Long-Range Transport Modeling. *Journal of Applied Meteorology and Climatology* 21 (3):367–372. doi:10.1175/1520-0450(1982)021<0367:HDPFLR>2.0.CO;2.

Dubovik, O. and King, M.D. (2000). A flexible inversion algorithm for retrieval of aerosol optical properties from Sun and sky radiance measurements. *Journal of Geophysical Research: Atmospheres* 105 (D16):20673–20696. doi:10.1029/2000JD900282.

Dubovik, O., Smirnov, A., Holben, B.N., King, M.D., Kaufman, Y.J., Eck, T.F., and Slutsker, I. (2000). Accuracy assessments of aerosol optical properties retrieved from Aerosol Robotic Network (AERONET) Sun and sky radiance measurements. *J. Geophys. Res.* 105 (D8):9791–9806. doi:10.1029/2000JD900040.

Eck, T.F., Holben, B.N., Reid, J.S., Dubovik, O., Smirnov, A., O'Neill, N.T., Slutsker, I., and Kinne, S. (1999). Wavelength dependence of the optical depth of biomass burning, urban, and desert dust aerosols. *J. Geophys. Res.* 104 (D24):31333–31349. doi:10.1029/1999JD900923.

Feng, Y.-C., Theisen, A., Lindenmaier, I.A., Collis, S., Giangrande, S., Comstock, J.M., Matthews, A.A., Rocque, M.N., Schuman, E.K., Wendler, T.G., Castro, V., Deng, M., Zhang, D., Xie, S., Flaherty, J.E., and Mather, J.H. (2023). ARM FY2024 Radar Plan (No. DOE/SC-ARM-TR-291). Oak Ridge National Laboratory (ORNL), Oak Ridge, TN (United States). Atmospheric Radiation Measurement (ARM) Data Center.

Fernandes, P. and Botelho, H. (2003). A review of prescribed burning effectiveness in fire hazard reduction. *International Journal of Wildland Fire* 12:127–128. doi:10.1071/WF02042.

Ford, B., Val Martin, M., Zelasky, S., Fischer, E., Anenberg, S., Heald, C., and Pierce, J. (2018). Future Fire Impacts on Smoke Concentrations, Visibility, and Health in the Contiguous United States. *GeoHealth* 2. doi:10.1029/2018GH000144.

Gan, R.W., Ford, B., Lassman, W., Pfister, G., Vaidyanathan, A., Fischer, E., Volckens, J., Pierce, J.R., and Magzamen, S. (2017). Comparison of wildfire smoke estimation methods and associations with cardiopulmonary-related hospital admissions. *Geohealth* 1 (3):122–136. doi:10.1002/2017GH000073.

Giles, D.M., Sinyuk, A., Sorokin, M.G., Schafer, J.S., Smirnov, A., Slutsker, I., Eck, T.F., Holben, B.N., Lewis, J.R., Campbell, J.R., Welton, E.J., Korkin, S.V., and Lyapustin, A.I. (2019). Advancements in the Aerosol Robotic Network (AERONET) Version 3 database – automated near-real-time quality control algorithm with improved cloud screening for Sun photometer aerosol optical depth (AOD) measurements. *Atmospheric Measurement Techniques* 12 (1):169–209. doi:10.5194/amt-12-169-2019.

Grant, E. and Runkle, J.D. (2022). Long-term health effects of wildfire exposure: A scoping review. *The Journal of Climate Change and Health* 6:100110. doi:10.1016/j.joclim.2021.100110.

Helin, A., Virkkula, A., Backman, J., Pirjola, L., Sippula, O., Aakko-Saksa, P., Väätäinen, S., Mylläri, F., Järvinen, A., Bloss, M., Aurela, M., Jakobi, G., Karjalainen, P., Zimmermann, R., Jokiniemi, J., Saarikoski, S., Tissari, J., Rönkkö, T., Niemi, J.V., and Timonen, H. (2021). Variation of Absorption Ångström Exponent in Aerosols From Different Emission Sources. *Journal of Geophysical Research: Atmospheres* 126 (10):e2020JD034094. doi:10.1029/2020JD034094.

Hersbach, H., Bell, B., Berrisford, P., Hirahara, S., Horányi, A., Muñoz-Sabater, J., Nicolas, J., Peubey, C., Radu, R., Schepers, D., Simmons, A., Soci, C., Abdalla, S., Abellan, X., Balsamo, G., Bechtold, P., Biavati, G., Bidlot, J., Bonavita, M., De Chiara, G., Dahlgren, P., Dee, D., Diamantakis, M., Dragani, R., Flemming, J., Forbes, R., Fuentes, M., Geer, A., Haimberger, L., Healy, S., Hogan, R.J., Hólm, E., Janisková, M., Keeley, S., Laloyaux, P., Lopez, P., Lupu, C., Radnoti, G., de Rosnay, P., Rozum, I., Vamborg, F., Villaume, S., and Thépaut, J.-N. (2020). The ERA5 global reanalysis. *Quarterly Journal of the Royal Meteorological Society* 146 (730):1999–2049. doi:10.1002/qj.3803.

Holben, B.N., Eck, T.F., Slutsker, I., Tanré, D., Buis, J.P., Setzer, A., Vermote, E., Reagan, J.A., Kaufman, Y.J., Nakajima, T., Lavenu, F., Jankowiak, I., and Smirnov, A. (1998). AERONET—A Federated Instrument Network and Data Archive for Aerosol Characterization. *Remote Sensing of Environment* 66 (1):1–16. doi:10.1016/S0034-4257(98)00031-5.

Hsu, N.C., Jeong, M.-J., Bettenhausen, C., Sayer, A.M., Hansell, R., Seftor, C.S., Huang, J., and Tsay, S.-C. (2013). Enhanced Deep Blue aerosol retrieval algorithm: The second generation. *Journal of Geophysical Research: Atmospheres* 118 (16):9296–9315. doi:10.1002/jgrd.50712.

Hsu, N.C., Tsay, S.-C., King, M.D., and Herman, J.R. (2004a). Aerosol properties over bright-reflecting source regions. *IEEE Transactions on Geoscience and Remote Sensing* 42 (3):557–569. doi:10.1109/TGRS.2004.824067.

Hsu, N.C., Tsay, S.-C., King, M.D., and Herman, J.R. (2004b). Aerosol properties over bright-reflecting source regions. *IEEE Transactions on Geoscience and Remote Sensing* 42 (3):557–569. doi:10.1109/TGRS.2004.824067.

Huang, X., Ding, K., Liu, J., Wang, Z., Tang, R., Xue, L., Wang, H., Zhang, Q., Tan, Z.-M., Fu, C., Davis, S.J., Andreae, M.O., and Ding, A. (2023). Smoke-weather interaction affects extreme wildfires in diverse coastal regions. *Science* 379 (6631):457–461. doi:10.1126/science.add9843.

Hung, W.-T., Lu, C.-H. (Sarah), Shrestha, B., Lin, H.-C., Lin, C.-A., Grogan, D., Hong, J., Ahmadov, R., James, E., and Joseph, E. (2020). The impacts of transported wildfire smoke aerosols on surface air quality in New York State: A case study in summer 2018. *Atmospheric Environment* 227:117415. doi:10.1016/j.atmosenv.2020.117415.

Iaukea-Lum, M., Bhattarai, C., Sengupta, D., Samburova, V., Khlystov, A.Y., Watts, A.C., Arnott, W.P., and Moosmüller, H. (2022). Optical Characterization of Fresh and Photochemically Aged Aerosols Emitted from Laboratory Siberian Peat Burning. *Atmosphere* 13 (3):386. doi:10.3390/atmos13030386.

Kogan, F. and Guo, W. (2015). 2006–2015 mega-drought in the western USA and its monitoring from space data. *Geomatics, Natural Hazards and Risk* 6 (8):651–668. doi:10.1080/19475705.2015.1079265.

Lack, D.A. and Cappa, C.D. (2010). Impact of brown and clear carbon on light absorption enhancement, single scatter albedo and absorption wavelength dependence of black carbon. *Atmospheric Chemistry and Physics* 10 (9):4207–4220. doi:10.5194/acp-10-4207-2010.

Lee, H., Calvin, K., Dasgupta, D., Krinner, G., Mukherji, A., Thorne, P., Trisos, C., Romero, José, Aldunce, P., Barrett, K., Blanco, G., Cheung, W.W.L., Connors, S.L., Denton, F., Diongue-Niang, A., Dodman, D., Garschagen, M., Geden, O., Hayward, B., Jones, C., Jotzo, F., Krug, T., Lasco, R., Lee, J.-Y., Masson-Delmotte, V., Meinshausen, M., Mintenbeck, K., Mokssit, A., Otto, F.E.L., Pathak, M., Pirani, A., Poloczanska, E., Pörtner, H.-O., Revi, A., Roberts, D.C., Romero, Jose, Roy, J., Ruane, A.C., Skea, J., Shukla, P.R., Slade, R., Slangen, A., Sokona, Y., Sörensson, A.A., Tignor, M., van Vuuren, D., Wei, Y.-M., Winkler, H., Zhai, P., and Zommers, Z. (2023). Climate Change 2023: Synthesis Report. Contribution of Working Groups I, II and III to the Sixth

Assessment Report of the Intergovernmental Panel on Climate Change (Report). The Australian National University.

Lee, J., Gorkowski, K., Meyer, A., Benedict, K., Aiken, A., and Dubey, M. (2022). Wildfire Smoke Demonstrates Significant and Predictable Black Carbon Light Absorption Enhancements. *Geophysical Research Letters* 49. doi:10.1029/2022GL099334.

Lewis, K., Arnott, W.P., Moosmüller, H., and Wold, C.E. (2008). Strong spectral variation of biomass smoke light absorption and single scattering albedo observed with a novel dual-wavelength photoacoustic instrument. *J. Geophys. Res.* 113 (D16):D16203. doi:10.1029/2007JD009699.

Li, J., Carlson, B.E., Yung, Y.L., Lv, D., Hansen, J., Penner, J.E., Liao, H., Ramaswamy, V., Kahn, R.A., Zhang, P., Dubovik, O., Ding, A., Lacis, A.A., Zhang, L., and Dong, Y. (2022). Scattering and absorbing aerosols in the climate system. *Nat Rev Earth Environ* 3 (6):363–379. doi:10.1038/s43017-022-00296-7.

Liu, C., Chung, C.E., Yin, Y., and Schnaiter, M. (2018). The absorption Ångström exponent of black carbon: from numerical aspects. *Atmospheric Chemistry and Physics* 18 (9):6259–6273. doi:10.5194/acp-18-6259-2018.

Magzamen, S., Gan, R.W., Liu, J., O'Dell, K., Ford, B., Berg, K., Bol, K., Wilson, A., Fischer, E.V., and Pierce, J.R. (2021). Differential Cardiopulmonary Health Impacts of Local and Long-Range Transport of Wildfire Smoke. *GeoHealth* 5 (3):e2020GH000330. doi:10.1029/2020GH000330.

Muradyan, P. and Coulter, R. (2020). Micropulse Lidar (MPL) Handbook (No. DOE/SC-ARM/TR-019). PNNL; Richland, WA.

O'Dell, K., Ford, B., Fischer, E.V., and Pierce, J.R. (2019). Contribution of Wildland-Fire Smoke to US PM2.5 and Its Influence on Recent Trends. *Environ. Sci. Technol.* 53 (4):1797–1804. doi:10.1021/acs.est.8b05430.

Petty, G.W. (2006). A First Course in Atmospheric Radiation Second Edition. Sundog Publishing LLC.

Reid, Koppmann, R., Eck, T.F., and Eleuterio, D.P. (2005). A review of biomass burning emissions part II: intensive physical properties of biomass burning particles. *Atmospheric Chemistry and Physics* 5 (3):799–825. doi:10.5194/acp-5-799-2005.

Russell, P.B., Redemann, J., Schmid, B., Bergstrom, R.W., Livingston, J.M., Mcintosh, D.M., Ramirez, S.A., Hartley, S., Hobbs, P.V., Quinn, P.K., Carrico, C.M., Rood, M.J., Öström, E., Noone, K.J., Von Hoyningen-Huene, W., and Remer, L. (2002). Comparison of aerosol single scattering albedos derived by diverse techniques in two North Atlantic experiments. *Journal of the Atmospheric Sciences* 59 (3):609–619. doi:10.1175/1520-0469(2002)059%3C0609%3ACOASSA%3E2.0.C.

Sayer, A.M., Hsu, N.C., Bettenhausen, C., and Jeong, M.-J. (2013). Validation and uncertainty estimates for MODIS Collection 6 "Deep Blue" aerosol data. *J. Geophys. Res. Atmos.* 118 (14):7864–7872. doi:10.1002/jgrd.50600.

Sayer, A.M., Hsu, N.C., Bettenhausen, C., Jeong, M.-J., and Meister, G. (2015). Effect of MODIS Terra radiometric calibration improvements on Collection 6 Deep Blue aerosol products: Validation and Terra/Aqua consistency. *Journal of Geophysical Research: Atmospheres* 120 (23):12,157-12,174. doi:10.1002/2015JD023878.

Sayer, A.M., Munchak, L.A., Hsu, N.C., Levy, R.C., Bettenhausen, C., and Jeong, M.-J. (2014). MODIS Collection 6 aerosol products: Comparison between Aqua's e-Deep Blue, Dark

Target, and "merged" data sets, and usage recommendations. *J. Geophys. Res. Atmos.* 119 (24):2014JD022453. doi:10.1002/2014JD022453.

Schuster, G.L., Dubovik, O., and Holben, B.N. (2006). Ångström exponent and bimodal aerosol size distributions. *Journal of Geophysical Research: Atmospheres* 111 (D7). doi:10.1029/2005JD006328.

Sedlacek, A.J., Lewis, E.R., Onasch, T.B., Zuidema, P., Redemann, J., Jaffe, D., and Kleinman, L.I. (2022). Using the Black Carbon Particle Mixing State to Characterize the Lifecycle of Biomass Burning Aerosols. *Environ. Sci. Technol.* 56 (20):14315–14325. doi:10.1021/acs.est.2c03851.

Sicard, M., Granados-Muñoz, M.J., Alados-Arboledas, L., Barragán, R., Bedoya-Velásquez, A.E., Benavent-Oltra, J.A., Bortoli, D., Comerón, A., Córdoba-Jabonero, C., Costa, M.J., del Águila, A., Fernández, A.J., Guerrero-Rascado, J.L., Jorba, O., Molero, F., Muñoz-Porcar, C., Ortiz-Amezcua, P., Papagiannopoulos, N., Potes, M., Pujadas, M., Rocadenbosch, F., Rodríguez-Gómez, A., Román, R., Salgado, R., Salgueiro, V., Sola, Y., and Yela, M. (2019). Ground/space, passive/active remote sensing observations coupled with particle dispersion modelling to understand the inter-continental transport of wildfire smoke plumes. *Remote Sensing of Environment* 232:111294. doi:10.1016/j.rse.2019.111294.

Sillanpää, M., Saarikoski, S., Hillamo, R., Pennanen, A., Makkonen, U., Spolnik, Z., Van Grieken, R., Koskentalo, T., and Salonen, R.O. (2005). Chemical composition, mass size distribution and source analysis of long-range transported wildfire smokes in Helsinki. *Sci Total Environ* 350 (1–3):119–135. doi:10.1016/j.scitotenv.2005.01.024.

Sokolik, I.N., Soja, A.J., DeMott, P.J., and Winker, D. (2019). Progress and Challenges in Quantifying Wildfire Smoke Emissions, Their Properties, Transport, and Atmospheric Impacts. *Journal of Geophysical Research: Atmospheres* 124 (23):13005–13025. doi:10.1029/2018JD029878.

Spracklen, D.V., Mickley, L.J., Logan, J.A., Hudman, R.C., Yevich, R., Flannigan, M.D., and Westerling, A.L. (2009). Impacts of climate change from 2000 to 2050 on wildfire activity and carbonaceous aerosol concentrations in the western United States. *Journal of Geophysical Research: Atmospheres* 114 (D20). doi:10.1029/2008JD010966.

Springston, S.R. (2018). Particle Soot Absorption Photometer (PSAP) Instrument Handbook (No. DOE/SC-ARM-TR-176). DOE ARM Climate Research Facility, Washington, DC (United States).

Stein, A.F., Draxler, R.R., Rolph, G.D., Stunder, B.J.B., Cohen, M.D., and Ngan, F. (2015). NOAA's HYSPLIT Atmospheric Transport and Dispersion Modeling System. *Bulletin of the American Meteorological Society* 96 (12):2059–2077. doi:10.1175/BAMS-D-14-00110.1.

Szopa, S., Naik, V., Adhikary, B., Artaxo, P., Berntsen, T., Collins, W.D., Fuzzi, S., Gallardo, L., Kiendler-Scharr, Z., Kilmont, Z., Liao, H., Unger, N., and Zanis, P. (2023). Short-lived Climate Forcers.*, in Climate Change 2021: The Physical Science Basis. Contribution of Working Group I to the Sixth Assessment Report of the Intergovernmental Panel on Climate Change,* Cambridge University Press, Cambridge, pp. 817–922.

Turpin, B.J., Huntzicker, J.J., Larson, S.M., and Cass, G.R. (1991). Los Angeles summer midday particulate carbon: primary and secondary aerosol. *Environ. Sci. Technol.* 25 (10):1788–1793. doi:10.1021/es00022a017.

Uin, J. (2024). Nephelometer Instrument Handbook (No. DOE/SC-ARM-TR-165). DOE ARM Climate Research Facility, Washington, DC (United States).

Welton, E.J., Campbell, J.R., and Starr, D.O. (2002). Micro-Pulse Lidar Signals: Uncertainty Analysis.

Westerling, A.L., Hidalgo, H.G., Cayan, D.R., and Swetnam, T.W. (2006). Warming and Earlier Spring Increase Western U.S. Forest Wildfire Activity. *Science* 313 (5789):940–943. doi:10.1126/science.1128834.

Wilkins, J.L., Foy, B. de, Thompson, A.M., Peterson, D.A., Hyer, E.J., Graves, C., Fishman, J., and Morris, G.A. (2020). Evaluation of Stratospheric Intrusions and Biomass Burning Plumes on the Vertical Distribution of Tropospheric Ozone Over the Midwestern United States. *Journal of Geophysical Research: Atmospheres* 125 (18):e2020JD032454. doi:10.1029/2020JD032454.

Woodhouse, C.A., Meko, D.M., MacDonald, G.M., Stahle, D.W., and Cook, E.R. (2010). A 1,200-year perspective of 21st century drought in southwestern North America. *Proceedings of the National Academy of Sciences* 107 (50):21283–21288. doi:10.1073/pnas.0911197107.

Wu, Y., Arapi, A., Huang, J., Gross, B., and Moshary, F. (2018). Intra-continental wildfire smoke transport and impact on local air quality observed by ground-based and satellite remote sensing in New York City. *Atmospheric Environment* 187:266–281. doi:10.1016/j.atmosenv.2018.06.006.

Yue, X., Mickley, L., Logan, J., and Kaplan, J. (2013). Ensemble projections of wildfire activity and carbonaceous aerosol concentrations over the western United States in the mid-21st century. *Atmospheric environment (Oxford, England : 1994)* 77:767–780. doi:10.1016/j.atmosenv.2013.06.003.